

Wave Propagation in Fractured Media: Theory and Applications of the Rotated Staggered Finite-Difference Grid

Wellenausbreitung in geklüfteten Medien: Theorie und Anwendungen der Methode des Rotated Staggered Finite-Difference Grid

Zur Erlangung des akademischen Grades eines

DOKTORS DER NATURWISSENSCHAFTEN

der Fakultät für Physik der
Universität Karlsruhe (TH)
genehmigte

DISSERTATION

von

Dipl.-Phys. Erik H. Saenger
aus Konstanz

Tag der mündlichen Prüfung:

3. Nov 2000

Referent:

Prof. Dr. Peter Hubral

Korreferent:

Prof. Dr. Serge A. Shapiro

Zusammenfassung

Der englischen Fassung der vorliegenden Dissertation ist eine ausführliche Zusammenfassung in Deutsch vorangestellt. Sie dient dazu, den ausschließlich deutschsprachigen Lesern einen Überblick über diese Arbeit zu geben sowie den Regelungen der Fakultät für Physik der Universität Karlsruhe zu entsprechen.

Für diese Zusammenfassung habe ich den gleichen Aufbau gewählt, der auch in der englischen Fassung verwendet wurde. Damit entspricht jeder Abschnitt der Zusammenfassung den Aussagen und Inhalten des entsprechenden Kapitels im Hauptteil der Arbeit.

Da es auch unter deutschsprachigen Geophysikern üblich ist, die englische Fachterminologie nicht ins Deutsche zu übersetzen, habe auch ich darauf verzichtet. Ich habe entsprechende Worte *kursiv* geschrieben.

A1: Einleitung

Die Seismik ist unter den Gesichtspunkten der Investitionen und der Anzahl der beteiligten Wissenschaftler die wichtigste geophysikalische Methodik. Diese hervorgehobene Stellung ergibt sich aus der hohen Genauigkeit, der hohen Auflösung und der hohen Eindringtiefe bei der Suche eines möglichst akkurate Abbildes des Erduntergrundes. Die Vielfalt der erforschten und verwendeten Techniken hat seine Ursache in der Exploration für Erdöl. Die Anzahl ergiebiger Bohrlöcher wäre gering ohne die intensive Nutzung der Seismik.

Das grundlegende Prinzip der seismischen Exploration ist die Tatsache, daß Inhomogenitäten des Mediums das einfallende Wellenfeld streuen [White, 1983]. Künstliche Druckquellen werden dazu verwendet, seismische Wellen in den Erduntergrund einzubringen. Der Streueffekt kann wiederum dazu benutzt werden, um aus dem gestreuten Wellenfeld, das an der Oberfläche registriert wird, auf das streuende Medium zu schließen [Yilmaz, 1987; Claerbout, 1985]. Diese Information kann dann dazu verwendet werden, die geologi-

sche Struktur zu ermitteln. Das gleiche Prinzip gilt für elastische Wellen in der zerstörungsfreien Prüfung, wo wesentlich kleinere Proben verwendet werden und deshalb höhere Frequenzen nötig sind [Reinhardt et al., 1996].

Aus diesem Grund ist das Studium der Ausbreitung von seismischen Wellen in komplexen, lateral variierenden dreidimensionalen Strukturen notwendig und wichtig. Dieser Ausbreitungsvorgang kann mit Hilfe einer Wellengleichung beschrieben werden. Es ist jedoch für komplexe Strukturen nicht möglich, exakte analytische Lösungen dieser partiellen Differentialgleichung zu ermitteln. Daher ist es notwendig, numerische Näherungsverfahren anzuwenden. Die neuartige Methode des *Rotated Staggered Finite-Difference Grid* [Saenger et al., 2000a] ist ein solches Verfahren und bildet die Basis und den ersten Schwerpunkt der vorliegenden Dissertation. Diese Technik ist besonders vorteilhaft, um sehr kontrastreiche Strukturen numerisch zu untersuchen. Neben zahlreichen Anwendungsbeispielen bildet daher die Bestimmung von effektiven Geschwindigkeiten in kontrastreichen geklüfteten Medien [Saenger and Shapiro, 2000b,a] den zweiten Schwerpunkt.

A2: Elastizitätstheorie

Mit Hilfe der Elastizitätstheorie wird der Ausbreitungsvorgang von elastischen Wellen in beliebig komplexen Medien beschrieben. In diesem Abschnitt werden in sehr komprimierter Form die zum Verständnis für diese Arbeit notwendigen Grundlagen behandelt. Für ein vertiefendes Studium elastischer Wellen empfehle ich folgende weiterführende Literatur: [Auld, 1973], [Crampin, 1981] , und [White, 1983].

Am Anfang werden die elementaren Größen *displacement-* (Verschiebungs-) Vektor, *strain-* (Verformungs-) und *stress-* (Rückstell-) Tensor eingeführt (Kapitel 2.1 und 2.2). Die für isotrope Medien gültige *stress-strain* Beziehung, das sogenannte Hook'sche Gesetz (isotrope Form), wird in Kapitel 2.3 behandelt. Um ein homogenes, elastisches und isotropes Medium vollständig zu beschreiben, benötigt man neben der Dichte noch zwei weitere voneinander unabhängige Variablen. Die verschiedenen in der Literatur dazu verwendeten elastischen Variablen (u.a. *Young's modulus*, *Shear modulus*, *Poisson's ratio*, *Bulk modulus*, *P wave modulus*) werden vorgestellt und die Umrechnung ineinander in einer Tabelle dargestellt. Zur Beschreibung beliebiger anisotroper Medien zu hat sich die Notation von [Auld, 1973] bewährt. Anhand der anisotropen Form des Hook'schen Gesetzes wird diese Notation in Kapitel 2.4 erläutert. Es ergibt sich eine 6×6 -Matrix Darstellung des *stiffness-* (Steifheits-) Tensors. Die drei wichtigsten Symmetrien, die in der Seismik eine Rolle spielen (isotrop, transversal isotrop, orthorhombisch), werden ebenfalls in der

vorliegenden Arbeit verwendet. Es werden zwei, fünf oder neun voneinander unabhängige elastische Parameter zur vollständigen Beschreibung des jeweiligen Mediums benötigt. Der Zusammenhang von seismischen Ausbreitungsgeschwindigkeiten und Elementen des *stiffness*-Tensors für die drei oben beschriebenen Symmetrien wird in Kapitel 2.5 behandelt. Es ist zu beachten, daß die Richtungsabhängigkeit der Ausbreitungsgeschwindigkeit in Abhängigkeit des Phasenwinkels angegeben ist. Dieser stimmt für anisotrope Medien nicht notwendigerweise mit dem Winkel der Ausbreitungsrichtung überein (Kapitel 2.6). Den Abschluß des Kapitels über die Elastizitätstheorie bildet die elastodynamische Wellengleichung, die sich aus dem zweiten Newton'schen Gesetz und dem Hook'schen Gesetz herleiten läßt.

A3: Die Theorie der Methode des Rotated Staggered Grid

In der Seismik kommen hauptsächlich zwei numerische Verfahren zur Lösung der elastodynamischen Wellengleichung zur Anwendung. Die erste Methode, das sogenannte *Ray-tracing* Verfahren (z. B. [Moser and Pajchel, 1997]), basiert auf einer Hochfrequenzapproximation und korrespondiert damit zur geometrischen Optik. Die Methode der Finiten Differenzen (FD) ist die zweite Methode und beinhaltet keine physikalischen Einschränkungen der Lösung [Kelly et al., 1976]. Für relativ einfache Strukturmodelle ist der Rechenaufwand von *Ray-tracing* Verfahren signifikant kleiner. Das ändert sich jedoch wenn sehr komplexe Medien untersucht werden. Während der Rechenaufwand bei *Ray-tracing* Verfahren mit der Komplexität des Modells ansteigt, bleibt der Rechenaufwand bei FD-Verfahren konstant.

Im Allgemeinen wird bei der Verwendung von FD-Techniken die Wellengleichung auf einem Gitter diskretisiert. Die räumlichen Ableitungen werden dabei durch FD-Operatoren ersetzt. Ebenfalls damit verbunden ist auch eine Diskretisierung der Zeit. Somit kann man zum Beispiel mit Hilfe einer Taylorreihe das Wellenfeld des jeweils nächsten Zeitschritts berechnen (Kapitel 3.2).

Um die numerische Genauigkeit von FD-Verfahren zu steigern, ist es inzwischen üblich, sogenannte *staggered grid* Techniken [Virieux, 1986] zu verwenden. Dabei werden die Ableitungen zwischen zwei Gitterpunkten in Richtung der Achsen berechnet. Dadurch ergibt sich eine spezielle Verteilung der Modellierungsparameter auch auf Zwischengitterplätzen. Bei der numerischen Lösung der Wellenausbreitung in Medien mit starken Kontrasten der elastischen Parameter führt dies jedoch zu Stabilitätsproblemen bei der Modellierung (z. B. [Crase, 1990]). Die Lösung dieses Problems wurde mit einer Modifikation

des FD-Gitters erreicht [Saenger et al., 2000a], welche zu einer veränderten Anordnung der Modellierungsparameter und der räumlichen Ableitungsrichtungen führt. Die prinzipiell neue Methode - das *rotated staggered finite-difference grid* - wird in der Folge und in Kapitel 3.3 detailliert beschrieben. Damit ist es möglich, die Ausbreitung elastischer Wellen in kontrastreichen Materialien zu simulieren, ohne explizite Randbedingungen angeben zu müssen. Zahlreiche Anwendungsmöglichkeiten sind Inhalt der weiteren Abschnitte. Um die Frage der numerischen Genauigkeit zu klären, werden die Stabilitätsbedingungen und die numerische Dispersion nach der von Neumann-Methode hergeleitet.

Die Diskretisierung von Medium und Wellenfeld

Um die Grundidee der Methode des *rotated staggered grid* einfach und klar darzustellen zu können, wird im folgenden Abschnitt nur das zweidimensionale Problem behandelt. Diese Überlegungen kann man jedoch auch auf dreidimensionale Medien anwenden, was im weiteren auch demonstriert wird.

Die Standardverteilung von Modellierungsparametern unter Verwendung der *staggered grid* Methode wurde als erstes von Virieux [1986] beschrieben und ist in Abbildung 3.1a dargestellt. Eine sehr ähnliche Methode [Kneib and Kerner, 1993; Karrenbach, 1995] ergibt die in Abbildung 3.1b gezeigte Verteilung. Es ist zu beachten, daß sich bei beiden *standard staggered grid*- Techniken die Elemente des *strain*- Tensors nicht an einer einzigen Position befinden. Bei kleinen Mediumskontrasten kann dieses Problem durch Mittelung oder durch einfaches Benutzen des nächstgelegenen Wertes behoben werden. Sollen jedoch hohe Kontraste modelliert werden, ist aus diesem Grund der Algorithmus nicht mehr stabil. Diese Art der Instabilität darf nicht mit der von Neumann-Stabilitätsbedingung verwechselt werden.

Die oben erwähnten Stabilitätsprobleme legen die Suche nach einer neuen Verteilung der Mediumsparameter nahe. Eine solche ist zum Beispiel in Abbildung 3.1c dargestellt. Sie kann erreicht werden, indem das gesamte Gitter um 45 Grad gedreht wird. Eine praktikablere Möglichkeit ist jedoch die in Abbildung 3.1d dargestellte Lösung, die die Basis der *rotated staggered grid*- Methode bildet. Die Neuverteilung der Modellierungsparameter, jetzt sind alle Elemente des *strain*- Tensors an einer einzigen Stelle definiert, wird durch einen speziellen Ableitungsoperator erreicht. Mit Hilfe dieses Ableitungsoperators werden die Ableitungen entlang der Raumdiagonalen berechnet und diese werden dann benutzt, um die Ableitungen in den Achsenrichtungen zu bestimmen. Somit ist in Standard-Modellierungsalgorithmen lediglich die Berechnung der Ableitungen, das Herzstück jedes

FD-Verfahrens, auszutauschen. Das Kapitel 3.4 gibt genaue Angaben wie der Ableitungsoperator in das FD-Schema zu implementieren ist.

Stabilität und Dispersion

Für eine ebene Welle, die sich in einem unendlichen, isotropen und homogenen Medium ausbreitet, gilt im Prinzip folgendes:

1. Die Amplitude bleibt unverändert.
2. Die Ausbreitungsgeschwindigkeit ist frequenzunabhängig.

Wird ein FD-Verfahren angewendet, ist es möglich, daß die Amplitude mit jedem Zeitschritt größer wird. Dies kann man vermeiden, indem man das (von Neumann-) Stabilitätskriterium erfüllt. Nach einer aufwendigen Berechnungsprozedur, beschrieben in Kapitel 3.5.1, ergibt sich das gesuchte Kriterium (siehe Formel 3.32). Es ist weniger restriktiv wie die vergleichbaren Bedingungen für ein *standard staggered grid* (siehe Formel 3.33 und 3.34).

Die Frequenzabhängigkeit der Ausbreitungsgeschwindigkeit lässt sich bei FD-Verfahren nicht vollständig vermeiden. Diesen Fehler (numerische Dispersion) kann man jedoch abschätzen und durch geeignete Wahl der Modellparameter auf eine akzeptable Größe reduzieren. Mit einer Dispersionsrelation steht ein Hilfsmittel für die Wahl dieser Parameter zur Verfügung. Die Herleitung der Dispersionsrelation wird in Kapitel 3.5.2 durchgeführt. Die praktische Interpretation erfolgt in Kapitel 3.5.3. Zu diesem Zweck wird der Dispersionsfehler des neuen FD-Verfahrens im Vergleich zum *staggered grid* graphisch dargestellt (siehe Abbildungen 3.3, 3.4, 3.5 und 3.6). Dazu werden, wie in der Fachliteratur üblich, zwei Parameter eingeführt. Der eine, γ , dient bei einem vorgegebenen Modell der Bestimmung des maximalen zeitlichen Inkrementes. Der andere, H , dient der Kontrolle der maximalen Frequenz des Quellsignals. Der Vergleich der beiden Verfahren ergibt, daß bei ähnlichen Bedingungen die gleiche numerische Genauigkeit erreicht wird.

A4: Anwendungen der Methode des Rotated Staggered Grid

In diesem Abschnitt werden sechs Anwendungsmöglichkeiten des *rotated staggered grid* (RSG) demonstriert. In den ausführlich beschriebenen Beispielen wird jeweils auf weiterführende Literatur hingewiesen.

Im relativ einfachen ersten Beispiel wird die Wellenausbreitung in einem homogenen elastischen Körper mit einem zentral gelegenen Riß modelliert. Dadurch können mehrere prinzipielle Eigenschaften der *rotated staggered grid*-Technik demonstriert werden. In Abbildung 4.1 ist das hierfür generierte Modell gezeigt. Am Modellierungsresultat (in der gleichen Abbildung) ist zu erkennen, daß der zentral gelegene Riß keine Schwierigkeiten bei der Berechnung der Wellenausbreitung verursacht. Auch die drei achsenparallelen “freien” Oberflächen sind ohne explizite Randbedingungen Bestandteil des elastischen Modells. Zusätzlich am unteren Rand implementierte *absorbing boundary conditions* zeigen, daß Standard FD Anwendungen auch für diese Methode angewendet werden können.

Die Simulation elastischer Wellen mittels FD-Verfahren ist bei Erdmodellen mit beliebiger (Oberflächen-) Topographie problematisch. Aufwendige Randbedingungen sind notwendig, ein solches Medium behandeln zu können (z. B. [Robertsson, 1996]). In Beispiel 2 wird anhand eines typischen Erdmodells gezeigt, daß die RSG-Methode keine Schwierigkeiten mit unebenen freien Oberflächen hat. Im Gegenteil, sogar eine sich ausbreitende Oberflächenwelle konnte erfolgreich modelliert werden (siehe Abbildung 4.3 und 4.4).

Schallwellen werden zunehmend auch in der zerstörungsfreien Prüfung angewendet. Die Impulswellenanalyse [Eberle and Gold, 1998] hat zum Ziel, Schäden nach den in der Geophysik bekannten Methoden zu detektieren. Im Rahmen dieser Untersuchungen wurde auch das in dieser Dissertation behandelte FD-Gitter verwendet. Dabei wurde, wie in Abbildung 4.6 aus Beispiel 3 zu erkennen ist, eine hervorragende Übereinstimmung von numerischen und experimentellen Resultaten erzielt [Saenger et al., 2000a].

In Beispiel 4 wurde die Ausbreitung von Plattenwellen in einer dünnen Aluminiumplatte numerisch untersucht. Die 305mm × 350mm × 1,5mm große Platte wurde dazu auf einem FD-Gitter diskretisiert. Das Quellsignal ist eine senkrecht auf der Plattenseite stehende Kraftquelle (siehe Abbildung 4.9). Dadurch werden stark disperse antisymmetrische Lambwellen [Viktorov, 1967] generiert (siehe Abbildung 4.8). Die in Abbildung 4.11 bis 4.15 gezeigten *snapshots* (Momentaufnahmen) zeigen die theoretisch vorhergesagte physikalische Dispersion und die Reflektionen der Wellen an den Plattenseiten und am Riß

sehr schön. Es ist zu beachten, daß die Farbskalen der *snapshots* jeweils auf das Maximum skaliert sind und damit verschieden sind. Das in diesem Beispiel gezeigte Modellierungsergebnis konnte in dieser Genauigkeit nur mit einer Simulation auf einem Großrechner erzielt werden: 180 parallel rechnende Prozessoren einer CRAY T3E benötigten ca. 10 Stunden Rechenzeit (5000 Zeitschritte).

Anisotropie ist ein häufig auftretendes Phänomen in der Seismik. In Beispiel 5 wird an einem sehr einfachen Modell (homogener Würfel) mit Hilfe des *rotated staggered grid* die Wellenausbreitung in einem transversal isotropen Medium simuliert. Das wichtigste Ziel dieses fünften Beispiels ist der Nachweis, daß anisotrope Modelle ebenfalls mit Hilfe des RSG untersucht werden können.

Beton ist ein sehr weit verbreiteter Werkstoff dessen Stabilität in vielen Bauwerken untersucht werden muß. Für die zerstörungsfreie Prüfung mittels Ultraschalltechniken ist es aber, unter anderem auch aufgrund seiner starken Heterogenitäten (Zement, Kies, Luftein schlüsse, Stahl, usw.), ein sehr komplexer Werkstoff. Bisher stand dem Experimentator nur ein numerisches Verfahren (*elastodynamic finite integration technique* (EFIT), siehe Fellinger et al. [1995]) zur Ermittlung der Wellenausbreitung in diesem Material zur Verfügung. In diesem letzten Beispiel wird anhand einer konkreten Anwendung (Rißdektion) erläutert, wie das gedrehte FD-Gitter auch in diesem Fall erfolgreich eingesetzt werden kann. Die stark heterogenen Strukturen erfordern keine besondere Behandlung im Berechnungsalgorithmus. Die hier erzielten numerischen Ergebnisse der Betonsimulation (Abbildung 4.17) verwendet eine *Imaging-* Studie [Vieth et al., 1999], um ein möglichst genaues Bild von der Position und Form eines Risses zu erhalten. Das Ergebnis ist in Abbildung 4.18 zu sehen.

A5: Effektive Geschwindigkeiten in kontrastreichen Medien

Grundsätzlich ist die genaue Lokalisierung eines gesuchten Reflektors (dies kann ein Reservoir in der Geophysik oder ein großer Riß in der zerstörungsfreien Prüfung sein) erschwert, wenn dieser sich in einem Gebiet befindet, in dem die elastischen Parameter des Mediums kleinskalig räumlich fluktuiieren. In diesem Fall trifft ein bereits gestörtes Wellenfeld auf den Reflektor und wird auf dem Rückweg zum Empfänger nochmals gestreut. In Abhängigkeit von den effektiven Eigenschaften des streuenden Mediums und der Wellenlänge resultiert diese Störung des Wellenfeldes in einer Dämpfung des kohärenten

(gemittelten) Feldanteils sowie einer Änderung seiner Geschwindigkeit. Da diese Effekte einen Einfluß auf weitere Rechenschritte (z. B. *Imaging*) haben, sollten sie bekannt sein. In der Exploration ist es sehr wichtig, Ausdehnung und Position eines Reflektors möglichst exakt zu bestimmen. Deshalb muß der Einfluß eines räumlich fluktuierenden Mediums auf das transmittierte Wellenfeld abgeschätzt und gegebenenfalls korrigiert werden.

Im Kapitel 5 werden zu diesem Zweck verschiedene zweidimensionale Medien untersucht, die mit zufallsverteilten Rissen versehen sind. Das scheint auf den ersten Blick eine große Vereinfachung zu sein. Die grundsätzlichen Erkenntnisse, die aus diesen Untersuchungen gewonnen werden können, sind jedoch auch auf dreidimensionale mit komplexeren Strukturen versehene Medien anwendbar.

Seit geraumer Zeit sind theoretische Vorhersagen effektiver Geschwindigkeiten in Medien, die Risse enthalten, ein wichtiges Thema in der Fachliteratur (z.B. [Eshelby, 1957; Knopoff, 1958]). Die Möglichkeiten, solche Theorien zu überprüfen, beschränkten sich jedoch im wesentlichen auf Ultraschallexperimente von Gesteinsproben. Mit der *rotated staggered grid*- Technik ist es nun möglich, diese Experimente unter absolut kontrollierten Bedingungen numerisch durchzuführen. Es werden drei verschiedenartige Materialien, die Risse enthalten, untersucht.

Als erstes werden zufällig in Richtung und Ort verteilte, geradlinige und sich nicht überschneidende, dünne trockene Risse in einem isotropen homogenen Material untersucht (siehe Abbildung 5.1). In der Literatur (z.B. [Davis and Knopoff, 1995]) existieren drei verschiedene Theorien, die die effektiven elastischen Parameter in Abhängigkeit der Rißdichte ρ (vgl. Formel 5.7) in diesem Fall vorhersagen. Namentlich sind das die *theory for non-interacting cracks*, die *self-consistent theory* und die sogenannte *modified self-consistent theory*. Die jeweiligen Formeln werden in Kapitel 5.2.3 ausführlich diskutiert. Die daraus resultierenden verschiedenen Geschwindigkeitsvorhersagen können in Abbildung 5.6 miteinander verglichen werden.

Als zweites werden sich überschneidende Risse untersucht (im Gegensatz zu sich nicht überschneidenden Rissen im ersten Beispiel). Ansonsten ändert sich im Vergleich zum Medium des ersten Falls nichts (siehe Abbildung 5.2). Damit ändert sich jedoch die physikalische Situation erheblich. Mit Hilfe der Perkolationstheorie (siehe z. B. [Sahimi, 1995]) läßt sich zeigen, daß es ab einer wohldefinierten sogenannten *critical crack density* ρ_c keinen Weg mehr für eine elastische Welle gibt, das Medium zu durchdringen (in den trockenen Rissen wird die Phasengeschwindigkeit auf Null gesetzt). Konventionelle Theorien können dieses Verhalten bisher nicht befriedigend beschreiben. Daher wurde im Rahmen dieser Dissertation eine neue Ansatz (*critical crack density (CCD) formulation*) entwickelt, um

dieses Verhalten zu beschreiben (siehe Kapitel 5.2.4). Abbildung 5.8 illustriert diese neuartige Geschwindigkeitsprognose elastischer Wellen in derartigen Medien.

Der Fall paralleler Risse, gezeigt in Abbildung 5.3, wurde bisher nur mit Hilfe einer *theory for non-interacting cracks* behandelt [Kachanov, 1992]. Diese wird in Kapitel 5.2.5 beschrieben; die Ergebnisse hierzu sind in Abbildung 5.9 zu sehen.

Die große Anzahl numerischer FD-Experimente zur Bestimmung der effektiven Geschwindigkeit wurden alle nach einem Prinzip durchgeführt (Kapitel 5.3.1). Mit Hilfe einer Kraftquelle wird eine ebene Welle am oberen Rand eines zweidimensionalen Modells generiert (siehe Abbildung 5.4). Es ist dabei möglich, drei verschiedene Wellentypen (SH(90), SV(90), P(90), siehe Abbildung 2.1) zu erzeugen und die dominante Frequenz zu variieren. Die ebene Welle durchdringt auf ihrem Weg zum unteren Rand eine Region mit vorher festgelegter und genau definierter *crack density* ρ . Die dadurch verursachte Verzögerung der Welle wird registriert und wird dazu verwendet, die effektive Geschwindigkeit zu berechnen.

Es zeigte sich, daß die *rotated staggered grid*-Technik für die oben beschriebenen Experimente besonders vorteilhaft ist. Mit herkömmlichen FD-Verfahren hätte jeder einzelne Riß in den verschiedenen Modellen mit entsprechenden Randbedingungen implementiert werden müssen. Es ist zu betonen, daß die Kriterien zur Vermeidung von Dispersionsfehlern (vgl. Kapitel 3.5.3) sehr genau gewählt wurden. Aufgrund dieser Tatsache wurde es notwendig, die Numerik auf einem leistungsfähigen Parallelrechner auszuführen.

Die numerischen Resultate der hier durchgeführten Studie werden in den Kapiteln 5.3.2 bis 5.3.4 für die drei oben beschriebenen Fälle vorgestellt und erläutert. Für zufällig verteilte und zufällig orientierte Risse zeigt sich eindeutig, daß die *modified self-consistent theory* am geeignetsten ist, effektive Geschwindigkeiten für diesen Fall vorherzusagen. In Abbildung 5.6 ist sehr schön die exzellente Übereinstimmung von dieser Theorie und den numerischen Resultaten für alle drei Wellentypen zu erkennen.

Die sehr gute Vorhersage der effektiven Geschwindigkeit im Fall sich überschneidender Risse durch die *critical crack density formulation* wird durch die numerischen Experimente bestätigt (Abbildung 5.8).

Die unzureichende Genauigkeit der *theory for non-interacting cracks* für große Werte der *crack density* ρ zeigt sich auch im Fall paralleler Risse (Abbildung 5.9). Hier ist es erforderlich, genauere Theorien zu finden.

A6: Schlußfolgerungen und Ausblick

Anhand zahlreicher Beispiele wurden die breiten Anwendungsmöglichkeiten der *rotated staggered grid*- Methode [Saenger et al., 2000a] demonstriert. Die Besonderheit der Methode hat ihre Ursache darin, daß alle Elemente einer physikalischen Größe jeweils nur an einer einzigen Position definiert sind. Diese Tatsache erlaubt im Gegensatz zu herkömmlichen Methoden, starke Mediumskontraste ohne die Angabe von Randbedingungen numerisch zu untersuchen. Die Existenz der Stabilitäts- und Dispersionskriterien für das modifizierte Finite-Differenzen-Verfahren erlaubt einen gezielten effizienten Einsatz dieser Methode.

Die in dieser Dissertation behandelte FD-Technik kann auch bei der numerischen Lösung anderer partieller Differentialgleichungen (z.B. parabolischer) eingesetzt werden. Es ist ebenfalls möglich das beschriebene Verfahren zur Berechnung von Schallwellen in viscoelastischen oder anelastischen Materialmodellen zu verwenden (vgl. Kapitel 6.1.2 bis 6.1.4).

Die erreichte Neuverteilung der Modellierungsparameter im Vergleich zu Standard FD-Techniken ist auch für die Simulation elastischer Wellen in anisotropen Medien von besonderem Vorteil. Durch eine notwendige Mittelung beim Verwenden eines konventionellen *standard staggered grid* entsteht ein zusätzlicher numerischer Fehler [Igel et al., 1995]. Dieser enfällt beim Verwenden des *rotated staggered grid*.

Die numerische Bestimmung effektiver Geschwindigkeiten in Kapitel 5 (und [Saenger and Shapiro, 2000a,b]) kann auf weitere verschiedenartige Medien erweitert werden. Insbesondere die Untersuchung dreidimensionaler Strukturen ist sowohl von theoretischem als auch von praktischem Interesse. Der als Beiproduct gewonnene Wert der Dämpfung der ebenen Welle, verursacht durch die in der Riß-Region stattfindende Streuung, kann ebenfalls mit den in der Literatur vorhandenen Theorien verglichen werden (z.B. [Metha, 1983]).

Abstract

The modeling of elastic waves with an explicit Finite Difference (FD) scheme on a staggered grid causes instability problems when the medium possesses high contrast discontinuities (strong heterogeneities). In this thesis I present a new rotated staggered grid (RSG) where all medium parameters are defined at appropriate positions within an elementary cell for the essential operations. Using this modified grid it is possible to simulate the propagation of elastic waves in a medium containing cracks, pores or free surfaces without applying boundary conditions. I compare the von Neumann stability criterion and the dispersion error for the new rotated staggered grid with the results of the standard staggered grid.

I show six synthetic examples to demonstrate the wide range of applications of the rotated staggered finite-difference technique in 2D and 3D. For instance the modeling of elastic wave propagation in concrete or the modeling of Lamb waves in thin plates is presented. Free surfaces in the presence of topography can be easily handled.

The rotated staggered grid allows an efficient and precise numerical study of effective velocities in fractured structures. I model the propagation of plane waves through a set of different randomly cracked media. In these numerical experiments I vary the wavelength of the plane waves, the porosity and the crack density. The synthetic results are compared with several static theories that predict the effective P- and S-wave velocities in fractured materials in the long wavelength limit. For randomly distributed and randomly oriented rectilinear non-intersecting thin dry cracks the numerical simulations of velocities of P-, SV- and SH-waves are in excellent agreement with the results of the modified (or differential) self-consistent theory. On the other hand for intersecting cracks the critical crack density (porosity) concept must be taken into account. To describe the wave velocities in media with intersecting cracks I propose to introduce the critical crack density concept into the modified self-consistent theory. Numerical simulations show that this new formulation predicts well effective elastic properties in such a case.

Finally, possible extensions of the modeling technique and further applications are discussed.

Contents

Zusammenfassung	iii
Abstract	xiii
1 Introduction	1
1.1 Motivation: Wave propagation in fractured media	1
1.2 Structure of the thesis	4
2 Elasticity and Hooke's Law	5
2.1 Displacement and strain	5
2.2 Stress	6
2.3 Elastic moduli - Isotropic Form of Hooke's Law	6
2.4 Anisotropic Form of Hooke's Law	8
2.5 Seismic velocities	11
2.6 Phase angle θ and ray angle ϕ	13
2.7 The elastodynamic wave equation	13
3 Theory of the rotated staggered finite-difference grid	15
3.1 Introduction	15
3.2 Basic numerical procedures and requirements for the FD modeling	16
3.3 Discretization of media and wavefields	17
3.3.1 Standard staggered grids	17

3.3.2	The rotated staggered grid	20
3.4	Discretization of derivatives of the new rotated staggered grid	21
3.4.1	2D case	21
3.4.2	3D case	23
3.5	Stability and dispersion	24
3.5.1	Neumann Stability	24
3.5.2	Dispersion relation	27
3.5.3	Dispersion analysis	29
3.6	Conclusions	35
4	Applications of the rotated staggered finite-difference grid	37
4.1	Example 1: 2D crack modeling	38
4.2	Example 2: Free-surface modeling in the presence of topography	39
4.3	Example 3: 3D aluminum plate - a comparison with laboratory data	42
4.4	Example 4: 3D modeling of Lamb waves in thin plates	44
4.5	Example 5: Modeling transversely isotropic media	50
4.6	Example 6: Modeling elastic waves in concrete	52
5	Effective velocities in fractured media	55
5.1	Introduction	55
5.2	Theory	57
5.2.1	Formulas for transversal isotropic media	57
5.2.2	Formulas for orthorhombic media	57
5.2.3	Non-intersecting Cracks	58
5.2.4	Intersecting Cracks	61
5.2.5	Parallel Cracks	65
5.3	Numerical Experiments	66
5.3.1	Experimental Setup	66

5.3.2	Numerical results for non-intersecting cracks	70
5.3.3	Numerical results for intersecting cracks	73
5.3.4	Numerical results for parallel cracks	75
5.4	Conclusions	76
6	Conclusions and perspectives	77
6.1	Extensions of the modeling scheme	77
6.1.1	General conclusions	77
6.1.2	A new principle to solve other partial differential equations	77
6.1.3	Modeling viscoelastic wave propagation	78
6.1.4	Modeling nonlinear wave propagation	78
6.1.5	Modeling wave propagation in general anisotropic media	79
6.2	Numerical Rock Physics	79
6.2.1	General conclusions	79
6.2.2	Effective velocities in 3D media	79
6.2.3	Scattering attenuation in 2D and 3D media	79
References		81
A Numerical Dispersion Relations		89
B Computational implementation of the rotated staggered grid		93
C Effective velocities in fractured media: database		99
List of Figures		107
Acknowledgments / Danksagung		111
Curriculum vitae		113

Chapter 1

Introduction

1.1 Motivation: Wave propagation in fractured media

The seismic method is by far the most important geophysical technique in terms of expenditures and number of geophysicists involved. Its predominance is due to high accuracy, high resolution and great penetration. The widespread use of seismic methods is principally in exploring for petroleum: the locations for exploratory wells are rarely made without seismic information.

The basic principle of seismic exploration is the fact that medium inhomogeneities cause scattering of seismic waves [White, 1983]. Explosives and other energy sources are used to generate them. The scattered wave field, detected with arrays of seismometers or geophones, can be used to determine the location of the scattering inhomogeneities within the medium [Yilmaz, 1987; Claerbout, 1985]. This information can be used for rock physics interpretation. The same principle is valid for elastic waves in ultrasonic testing where smaller samples and therefore higher frequencies are used [Reinhardt et al., 1996].

Therefore, the propagation of seismic waves in complex laterally varying 3D layered structures is a relevant process. This process can be described by the wave equation. But exact analytical solutions of the elastic wave equation do not exist for most configurations of exploration or non-destructive testing interest, and solutions to realistic models may be obtained only by means of approximation.

The most common approaches to the investigation of wave propagation in complex structures are methods based on direct numerical solutions of the elastodynamic wave equation such as finite difference and finite-element methods or approximate high frequency asymptotic methods. All of these methods are very useful to solve certain types of wave propagation problems, have their own advantages and disadvantages, and complement suitably each other.

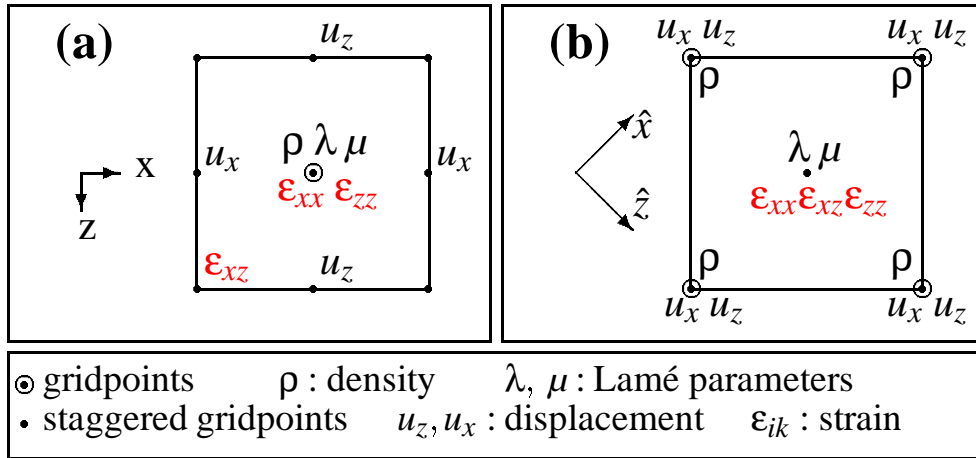


Figure 1.1: Elementary cells with locations where strains, displacement and elastic parameters are defined. **(a)** Locations are shown on a standard staggered grid if no averaging of medium parameters is performed. **(b)** Elementary cell of the rotated staggered grid. Spatial derivatives are performed along the \hat{x} - and \hat{z} -axes.

For the finite difference (FD) technique the partial differential equations of motion are approximated by suitable FD equations, which can be solved on a discrete spatial grid by strictly numerical procedures [Kelly et al., 1976]. Explicit schemes determine the motion for a space location at an advanced time exclusively from the motion already determined for previous times. Crucial parameters in finding such a FD solution to the continuous problem are the derivative operators. A well-established method is to use operators where the derivative value is located between original grid points. The main reason for using this so-called staggered grid method [Virieux, 1986] is to improve numerical accuracy with respect to centered FD grids. Since the FD approach is based on the wave equation without physical approximations, the method accounts not only for direct waves, primary reflected waves, and multiply reflected waves, but also for surface waves, head waves, converted reflected waves, and waves observed in ray-theoretical shadow zones. Additionally, it automatically accounts for the proper relative amplitudes.

So far, the modeling of elastic waves with an explicit FD scheme on a staggered grid causes instability problems when the medium possesses high contrast discontinuities (strong heterogeneities). In this thesis I present a new rotated staggered grid [Saenger et al., 2000a] where all medium parameters are defined at appropriate positions within an elementary grid cell for the essential operations (see Figure 1.1). Using this modified grid it is possible to simulate the propagation of elastic waves in a medium containing cracks, pores or free surfaces without applying boundary conditions. In order to clarify the question of accuracy I compare the von Neumann stability criterion and the dispersion error for the new rotated staggered grid (RSG) with the results of the standard staggered grid.

The new FD technique can be applied in various problems concerning wave propagation in complex fractured media:

- A fundamental aim of seismic data processing is to transform the acquired data into the best possible structural image of the subsurface. Synthetic seismograms of models with free surface topography calculated with the RSG method can aid in the understanding and the interpretation of wave patterns observed on field seismograms.
- Large-scale numerical solutions of the elastodynamic wave equation are required to get a better understanding of wave phenomena in the development of non-destructive testing methods. The rotated staggered grid is an excellent approach for this application, e.g. to model Lamb wave in thin plates [Saenger et al., 2000b]. The numerical solutions obtained with the RSG compare favorable with experimental data.
- Concrete as a strongly heterogeneous and highly-packed composite material represents an important but also difficult object for ultrasonic investigations. Due to the high density of scatterers the ultrasonic wave propagation in such a material is very complex and contains effects such as multiple scattering, mode conversion and diffusive energy transportation. The application of the RSG allows to model the wave propagation and scattering process explicitly in the time domain [Saenger et al., 1999c].

Problems in the seismic method arise, if an unknown target (this might be a reservoir in geophysics or a large crack in nondestructive testing) is embedded in an inhomogeneous medium causing scattering itself. In this case, an already distorted wave field arrives at the target and becomes distorted again on the way from the target to the receiver at the surface. Depending on the physical properties of the fluctuating medium and the wavelength, the wavefield distortion results in a velocity shift and in an attenuation of the coherent part of the transmitted wave field. Since these effects influence the results of further operations, they have to be taken into account.

Especially in seismic exploration, where it is necessary to determine the position and depth of a reflector as accurately as possible, a description of the effective properties of a fractured medium is of great importance. In general the science of rock physics addresses the relationship between the physical properties of rocks and geophysical observations. During the past three decades, scientists have discovered an increasing number of relations among properties that once appeared unrelated [Mavko et al., 1998].

Many of these relations are based on theories with certain approximations or experimental methods like laboratory testing of core samples. Fundamental new ways to achieve relations between rock properties are numerical rock physics methods. FD-experiments seem to be a good choice for this purpose. As described above, the rotated staggered FD scheme is a powerful tool for testing theories about fractured media. My numerical modeling of elastic properties of dry rock skeletons can be considered as an efficient and well controlled computer experiment. The different formalisms discussed in this thesis predict the

effective elastic moduli of multiply fractured media as a function of crack density ρ or porosity ϕ [Saenger and Shapiro, 2000b].

1.2 Structure of the thesis

The thesis is structured as follows: This chapter gives an overview of the thesis.

Chapter 2 introduces the theory of elasticity which is necessary to understand the following chapters.

In Chapter 3, I introduce the theory of the rotated staggered finite difference grid (RSG). I propose an accurate and efficient scheme to determine numerical solutions of the elasto-dynamic wave equation. The derivation of the numerical accuracy of this scheme is a very important part in this chapter.

In Chapter 4, I show some applications of the new modeling technique. Six different examples demonstrate the diversity of new modeling possibilities.

Chapter 5 compares theoretical predictions of effective velocities in fractured media with numerical results obtained with the help of the new modeling tool. In addition I present a new formalism, the so-called critical crack density formulae, to predict effective velocities in fractured structures.

In Chapter 6, I give some concluding remarks and discuss further perspectives of the RSG-method.

Numerical dispersion relations for high orders in space are given in Appendix A.

The High Performance Fortran (HPF) implementation of the RSG is presented in Appendix B.

In Appendix C the detailed results of the numerical study presented in Chapter 5 are shown.

Chapter 2

Elasticity and Hooke's Law

This chapter gives the reader an overview of waves in elastic media. The theory will be introduced very concisely and in a way that the following chapters can be understood without previous knowledge. Auld [1973], Crampin [1981], and White [1983] are recommended for a more detailed introduction into this topic.

2.1 Displacement and strain

The displacement u is the deviation of a point from the position it had in absence of external forces or elastic waves propagating through the medium. Since the deviation can be in all directions, u is a vectorial quantity and depends on the Cartesian components x , y and z of the initial position \mathbf{r} . Considering an infinitesimal small length l between two points within an elastic medium, we can describe the change of this length caused by deformation of the medium by the following equation :

$$l'^2 = l^2 + 2\epsilon_{ij}\delta x_i \delta x_j \quad (2.1)$$

The quantity ϵ_{ij} is the strain tensor and reads for small displacements :

$$\epsilon_{ij} = \frac{1}{2}(u_{i,j} + u_{j,i}) \quad (2.2)$$

The components of the strain tensor with $i = j$ denote compression along axis i , components with $i \neq j$ denote shear distortion of the i -axis in j -direction (and vice versa).

Considering a small area δV that has the volume $\delta V'$ after deformation, the change of volume depends directly on the strain tensor components. The new volume reads

$$\delta V' = \delta V(1 + \epsilon_{11} + \epsilon_{22} + \epsilon_{33}) \quad (2.3)$$

It should be noted that the strain tensor includes only 6 independent components, since $\epsilon_{ij} = \epsilon_{ji}$.

2.2 Stress

The stress tensor can be described in terms of forces acting on a body V . Since a scalar quantity (like the force in x -direction) can be written as divergence of a vector, we can write the full force as divergence of a tensorial quantity. Thus, we find

$$F_i = \sigma_{ij,j} \quad (2.4)$$

The quantity σ_{ij} is called the stress tensor. Similar to the strain tensor, we can distinguish between longitudinal components of the stress tensor ($i = j$) and shear components ($i \neq j$).

Again we have 6 independent components of the stress tensor.

2.3 Elastic moduli - Isotropic Form of Hooke's Law

In an isotropic, linear elastic material stress and strain related by Hooke's law as follows (see e.g [Timoshenko and Goodier, 1934]):

$$\sigma_{ij} = \lambda \delta_{ij} \epsilon_{\alpha\alpha} + 2\mu \epsilon_{kl} \quad (2.5)$$

or

$$\epsilon_{ij} = \frac{1}{E} ((1 + \nu) \sigma_{ij} - \nu \delta_{ij} \sigma_{\alpha\alpha}) \quad (2.6)$$

where

- ϵ_{ij} := elements of the strain tensor
- σ_{ij} := elements of the stress tensor
- $\epsilon_{\alpha\alpha}$:= volumetric strain (sum over repeated index)
- $\sigma_{\alpha\alpha}$:= mean stress times 3 (sum over repeated index)
- δ_{ij} := 0 if $i \neq j$, 1 if $i = j$

In an isotropic, linear elastic medium, only two constants are needed to specify the stress-strain relation completely (for example, $[\lambda, \mu]$ in equation 2.5 or $[E, \nu]$, which can be derived from $[\lambda, \mu]$, in equation 2.6). Other useful and convenient moduli can be defined but are always relatable to just two constants (see Table 2.1). For example, the

- Young's modulus, E , defined as the ratio of extensional stress to extensional strain in a uniaxial stress state:

$$\sigma_{zz} = E \epsilon_{zz}, \quad \sigma_{xx} = \sigma_{yy} = \sigma_{xy} = \sigma_{xz} = \sigma_{yz} = 0 \quad (2.7)$$

K	E	λ	ν	M	μ
$\lambda + 2\mu/3$	$\mu \frac{3\lambda + 2\mu}{\lambda + \mu}$	-	$\frac{\lambda}{2(\lambda + \mu)}$	$\lambda + 2\mu$	-
-	$9K \frac{K - \lambda}{3K - \lambda}$	-	$\frac{\lambda}{3K - \lambda}$	$3K - 2\lambda$	$3(K - \lambda)/2$
-	$\frac{9K\mu}{3K + \mu}$	$K - 2\mu/3$	$\frac{3K - 2\mu}{2(3K + \mu)}$	$K + 4\mu/3$	-
$\frac{E\mu}{3(3\mu - E)}$	-	$\mu \frac{E - 2\mu}{3\mu - E}$	$E/(2\mu) - 1$	$\mu \frac{4\mu - E}{3\mu - E}$	-
-	-	$3K \frac{3K - E}{9K - E}$	$\frac{3K - E}{6K}$	$3K \frac{3K + E}{9K - E}$	$\frac{3KE}{9K - E}$
$\lambda \frac{1 + \nu}{3\nu}$	$\lambda \frac{(1 + \nu)(1 - 2\nu)}{\nu}$	-	-	$\lambda \frac{(1 - \nu)}{\nu}$	$\lambda \frac{(1 - 2\nu)}{2\nu}$
$\mu \frac{2(1 + \nu)}{3(1 - 2\nu)}$	$2\mu(1 + \nu)$	$\mu \frac{2\nu}{1 - 2\nu}$	-	$\mu \frac{2 - 2\nu}{1 - 2\nu}$	-
-	$3K(1 - 2\nu)$	$3K \frac{\nu}{1 + \nu}$	-	$3K \frac{1 - \nu}{1 + \nu}$	$3K \frac{1 - 2\nu}{2 + 2\nu}$
$\frac{E}{3(1 - 2\nu)}$	-	$\frac{E\nu}{(1 + \nu)(1 - 2\nu)}$	-	$\frac{E(1 - \nu)}{(1 + \nu)(1 - 2\nu)}$	$\frac{E}{2 + 2\nu}$

Table 2.1: Relationships among elastic constants in an isotropic material (after Birch [1961])

- Shear modulus, $\mu = \rho V_S^2$, defined as the ratio of shear stress to shear strain:

$$\sigma_{ij} = 2\mu\epsilon_{ij}, \quad i \neq j \quad (2.8)$$

- Bulk modulus, K , defined as the ratio of hydrostatic stress, σ_0 , to volumetric strain:

$$\sigma_0 = \frac{1}{3}\sigma_{\alpha\alpha} = K\epsilon_{\alpha\alpha} \quad (2.9)$$

- P wave modulus, $M = \rho V_P^2$, defined as the ratio of axial stress to axial strain in a uniaxial strain state:

$$\sigma_{zz} = M\epsilon_{zz}, \quad \epsilon_{xx} = \epsilon_{yy} = \epsilon_{xy} = \epsilon_{xz} = \epsilon_{yz} = 0 \quad (2.10)$$

- Poisson's ratio, ν , which is defined as minus the ratio of lateral strain to axial strain in a uniaxial stress state:

$$\nu = \frac{\epsilon_{xx}}{\epsilon_{zz}}, \quad \sigma_{xx} = \sigma_{yy} = \sigma_{xy} = \sigma_{xz} = \sigma_{yz} = 0 \quad (2.11)$$

Note that the moduli (λ, μ, K, E, M) all have the same units as stress (force/area), whereas Poisson's ratio is dimensionless.

Energy considerations require that the following relations always hold. If they do not, one should suspect experimental errors or that the material is not isotropic.

$$\lambda + \frac{2\mu}{3} \geq 0; \quad \mu \geq 0 \quad (2.12)$$

or

$$-1 < \nu \leq 1/2; \quad E \geq 0 \quad (2.13)$$

2.4 Anisotropic Form of Hooke's Law

Hooke's law for a general anisotropic, linear elastic solid states that the stress σ_{ij} is linearly proportional to the strain ϵ_{ij} as expressed by

$$\sigma_{ij} = c_{ijkl}\epsilon_{kl} \quad (2.14)$$

in which summation is implied over repeated subscripts k and l . The elastic stiffness tensor, with elements c_{ijkl} , is a fourth-rank tensor obeying the laws of tensor transformation and has a total of eighty-one components. However, not all eighty-one components are independent. The symmetry of stresses and strains implies that

$$c_{ijkl} = c_{jikl} = c_{ijlk} = c_{jilk} \quad (2.15)$$

reducing the number of independent constants to thirty-six. Also the existence of a unique strain energy potential requires that

$$c_{ijkl} = c_{klji} \quad (2.16)$$

further reducing the number of elastic constants to twenty-one. This is the maximum number of elastic constants that any medium can have. Additional restrictions imposed by symmetry considerations reduce the number much further. Isotropic, linear elastic materials, which have the maximum symmetry, are completely characterized by two independent constants, whereas materials with triclinic symmetry (lowest symmetry) require all twenty-one constants.

Alternatively, the strains may be expressed as a linear combination of the stress by the expression

$$\epsilon_{ij} = s_{ijkl}\sigma_{kl} . \quad (2.17)$$

In this case s_{ijkl} are elements of the elastic compliance tensor, which has the same symmetry as the corresponding stiffness tensor. The compliance and stiffness are tensor inverses denoted by

$$c_{ijkl}s_{klmn} = I_{ijmn} = \frac{1}{2}(\delta_{im}\delta_{jn} + \delta_{in}\delta_{jm}) . \quad (2.18)$$

It is a standard practice in elasticity to use an abbreviated notation for the stresses, strains, and the stiffness and compliance tensors, for doing so simplifies some of the key equations [Auld, 1973]. In this abbreviated notation the stresses and strains are written as six-element column vectors rather than as nine element square matrices:

$$\mathbf{T} = \begin{bmatrix} \sigma_1 = \sigma_{11} \\ \sigma_2 = \sigma_{22} \\ \sigma_3 = \sigma_{33} \\ \sigma_4 = \sigma_{23} \\ \sigma_5 = \sigma_{13} \\ \sigma_6 = \sigma_{12} \end{bmatrix} \quad \mathbf{E} = \begin{bmatrix} \epsilon_1 = \epsilon_{11} \\ \epsilon_2 = \epsilon_{22} \\ \epsilon_3 = \epsilon_{33} \\ \epsilon_4 = 2\epsilon_{23} \\ \epsilon_5 = 2\epsilon_{13} \\ \epsilon_6 = 2\epsilon_{12} \end{bmatrix}$$

Note the factor of 2 in the definitions of strains.

The four subscripts of the stiffness and compliance tensors are reduced to two. Each pair of indices $ij(kl)$ is replaced by one index $I(J)$ using the following convention:

$ij(kl)$	$I(J)$
11	1
22	2
33	3
23, 32	4
13, 31	5
12, 21	6

The relation, therefore, is $c_{IJ} = c_{ijkl}$ and $s_{IJ} = s_{ijkl}N$ where:

$$N = \begin{cases} 1 & \text{for } I \text{ and } J = 1, 2, 3 \\ 2 & \text{for } I \text{ or } J = 4, 5, 6 \\ 4 & \text{for } I \text{ and } J = 4, 5, 6 \end{cases}$$

In the two-index notation, c_{IJ} and s_{IJ} can conveniently represented as 6×6 matrices. However, they no longer follow the laws of tensor transformation. Care has to be taken when transforming from one coordinate system to another. One way is to go back to the four-index notation and then use the ordinary laws of coordinate transformation. A more efficient method is to use the Bond transformation matrices, which can be found in [Mavko et al., 1998].

The nonzero components of the more symmetric anisotropy classes used in this thesis are given below.

Isotropic - two independent constants:

$$\begin{bmatrix} c_{11} & c_{12} & c_{12} & 0 & 0 & 0 \\ c_{12} & c_{11} & c_{12} & 0 & 0 & 0 \\ c_{12} & c_{12} & c_{11} & 0 & 0 & 0 \\ 0 & 0 & 0 & c_{44} & 0 & 0 \\ 0 & 0 & 0 & 0 & c_{44} & 0 \\ 0 & 0 & 0 & 0 & 0 & c_{44} \end{bmatrix}$$

with $c_{12} = c_{11} - 2c_{44}$. The relations between the elements c and the Lamé's parameters λ and μ of isotropic linear elasticity are:

$$c_{11} = \lambda + 2\mu \quad c_{12} = \lambda \quad c_{44} = \mu \quad (2.19)$$

Transversely isotropic - five independent constants:

$$\begin{bmatrix} c_{11} & c_{12} & c_{13} & 0 & 0 & 0 \\ c_{12} & c_{11} & c_{13} & 0 & 0 & 0 \\ c_{13} & c_{13} & c_{33} & 0 & 0 & 0 \\ 0 & 0 & 0 & c_{44} & 0 & 0 \\ 0 & 0 & 0 & 0 & c_{44} & 0 \\ 0 & 0 & 0 & 0 & 0 & c_{66} \end{bmatrix}$$

with $c_{66} = \frac{1}{2}(c_{11} - c_{22})$.

Orthorhombic - nine independent constants:

$$\begin{bmatrix} c_{11} & c_{12} & c_{13} & 0 & 0 & 0 \\ c_{12} & c_{22} & c_{23} & 0 & 0 & 0 \\ c_{13} & c_{23} & c_{33} & 0 & 0 & 0 \\ 0 & 0 & 0 & c_{44} & 0 & 0 \\ 0 & 0 & 0 & 0 & c_{55} & 0 \\ 0 & 0 & 0 & 0 & 0 & c_{66} \end{bmatrix}$$

2.5 Seismic velocities

- For isotropic symmetry the phase velocity of wave propagations given by:

$$v_P^2 = \frac{\lambda + 2\mu}{\rho} \equiv \frac{c_{11}}{\rho} \quad (2.20)$$

$$v_S^2 = \frac{\mu}{\rho} \equiv \frac{c_{44}}{\rho} \quad (2.21)$$

In anisotropic media there are, in general, three modes of propagation (quasi-longitudinal, quasi-shear and pure shear) with mutually orthogonal polarizations.

- For a medium with transversely isotropic (hexagonal) symmetry, the wave slowness surface is always rotationally symmetric about the axis of symmetry. The velocities of the three modes in any plane containing the symmetry axis are given as:

quasi-longitudinal mode (transversely isotropic)

$$v_P = (c_{11} \sin^2 \theta + c_{33} \cos^2 \theta + c_{44} + \sqrt{M})^{1/2} (2\rho)^{-1/2} \quad (2.22)$$

quasi-shear mode (transversely isotropic)

$$v_{SV} = (c_{11} \sin^2 \theta + c_{33} \cos^2 \theta + c_{44} - \sqrt{M})^{1/2} (2\rho)^{-1/2} \quad (2.23)$$

pure shear mode (transversely isotropic)

$$v_{SH} = \left(\frac{c_{66} \sin^2 \theta + c_{44} \cos^2 \theta}{\rho} \right)^{1/2} \quad (2.24)$$

where

$$M = [(c_{11} - c_{44}) \sin^2 \theta - (c_{33} - c_{44}) \cos^2 \theta]^2 + (c_{13} + c_{44})^2 \sin^2 2\theta \quad (2.25)$$

and θ is the angle between the wave vector and the axis of symmetry.

- For the more general orthorhombic symmetry the velocities of the three modes propagating in the three symmetry planes (XZ , YZ , and XY) are given for the XZ plane as follows:

quasi-longitudinal mode (orthorhombic - XZ plane)

$$v_P = \left(c_{55} + c_{11} \sin^2 \theta + c_{33} \cos^2 \theta + \sqrt{(c_{55} + c_{11} \sin^2 \theta + c_{33} \cos^2 \theta)^2 - 4A} \right)^{1/2} (2\rho)^{-1/2} \quad (2.26)$$

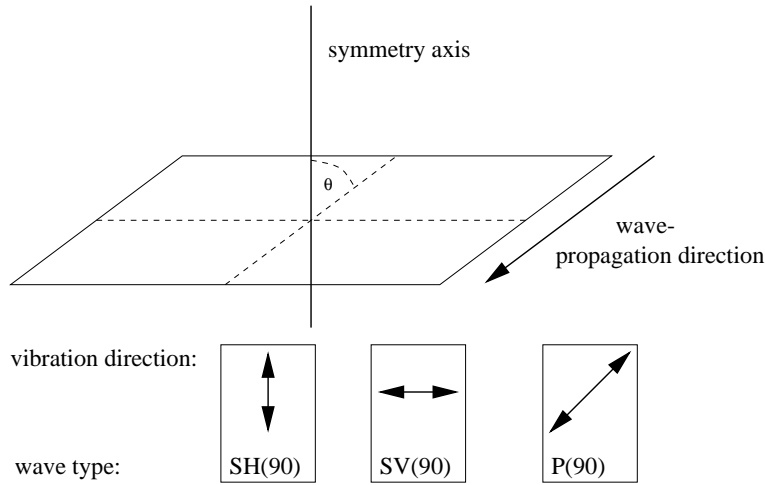


Figure 2.1: This figure illustrates three types (SH(90), SV(90) and P(90)) of waves in transversely isotropic media. This type of media is used in chapter “Effective velocities in fractured media”.

quasi-shear mode (orthorhombic - X Z plane)

$$v_{\text{SV}} = \left(c_{55} + c_{11} \sin^2 \theta + c_{33} \cos^2 \theta - \sqrt{(c_{55} + c_{11} \sin^2 \theta + c_{33} \cos^2 \theta)^2 - 4A} \right)^{1/2} (2\rho)^{-1/2} \quad (2.27)$$

pure shear mode (orthorhombic - X Z plane)

$$v_{\text{SH}} = \left(\frac{c_{66} \sin^2 \theta + c_{44} \cos^2 \theta}{\rho} \right)^{1/2} \quad (2.28)$$

where

$$A = (c_{11} \sin^2 \theta + c_{55} \cos^2 \theta)(c_{55} \sin^2 \theta + c_{33} \cos^2 \theta) - (c_{13} + c_{55}) \sin^2 \theta \cos^2 \theta \quad (2.29)$$

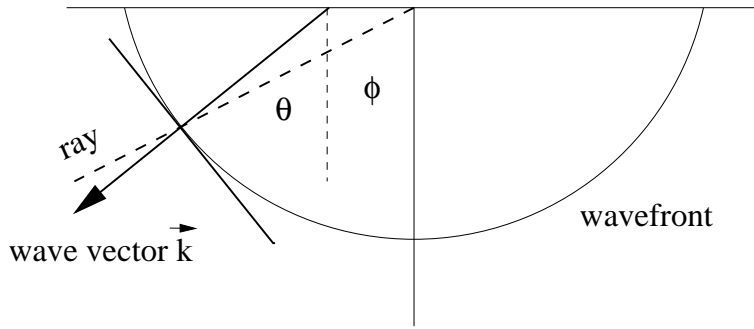


Figure 2.2: This figure graphically indicates the definitions of phase (wavefront) angle θ and group (ray) angle ϕ .

2.6 Phase angle θ and ray angle ϕ

It is important to clarify the distinction between the phase angle θ and the ray angle ϕ (along which energy propagates). Referring to Figure 2.2, the wavefront is locally perpendicular to the propagating vector \mathbf{k} , since \mathbf{k} points in the direction of maximum rate of increase of phase. The phase velocity $v(\theta)$ is also called the wavefront velocity, since it measures the velocity of advance of the wavefront along $\mathbf{k}(\theta)$. Since the wavefront is nonspherical, it is clear that θ (also called the wavefront-normal angle) is different from ϕ , the ray angle from source point to the wavefront. The exact relations between θ and ϕ can be found e.g. in [Berryman, 1979].

2.7 The elastodynamic wave equation

The propagation of elastic waves is described by the elastodynamic wave equation (e.g. [Gubernatis et al., 1977]), also called generalized Hooke's law (based on the linear stress-strain relation and Newton's second law):

$$\rho(\mathbf{r})\ddot{u}_i(\mathbf{r}) = (c_{ijkl}(\mathbf{r})u_{k,l}(\mathbf{r}))_{,j} + f_i(\mathbf{r}) \quad (2.30)$$

In this equation, u denotes the displacement (deviation of a point from its position without any forces), ρ denotes the density and c_{ijkl} denotes the stiffness tensor. f_i is the force applied at the point \mathbf{r} . If only the propagation of waves is under concern and not the origin, f_i can be omitted in this equation.

Here (and from now on), standard tensor index convention is used. Indices that occur twice imply summation, the subscript $,i$ denotes differentiation with respect to the i -coordinate.

Chapter 3

Theory of the rotated staggered finite-difference grid

In this chapter I present the rotated staggered grid finite-difference method as tool for numerical solutions of the elastodynamic wave equation. The accuracy of the proposed method was justified by a so-called von Neumann style analysis.

This chapter is based on: [Saenger et al., 1998, 1999a,b,c, 2000a]

3.1 Introduction

Only in rather simple cases the propagation of elastic waves can be described by exact analytical expressions. In more complex situations, Born or Rytov type approximations provide expressions that become exact in the limit of low frequency or low contrast. Another type of approximation widely used in seismology are the Ray-tracing methods (e.g. [Moser and Pajchel, 1997]). These techniques based on ray theory (e.g. [Cerveny et al., 1977; Achenbach et al., 1982]) are valid for high frequencies and correspond to geometrical optics. For relatively simple models the computing time required by ray tracing methods is significantly smaller than the computing time for a Finite Difference (FD) scheme. This changes, however, for the case of very complicated models, because the time required for Ray-tracing increases with complexity of the model, whereas the computing time for FD methods remains the same.

FD methods discretize the wave equation on a grid. They replace spatial derivatives by FD operators using neighboring points. The wavefield is also discretized in time, and the wavefield for the next timestep is calculated in general by using a Taylor expansion (other studies apply e.g. Chebyshev expansion [Tal-Ezar et al., 1987]). Elastic FD methods can be separated in time domain FD methods [Dablain, 1986; Kneib and Kerner, 1993; Karrenbach, 1995; Igel et al., 1995], using the 2nd order wave equation, and velocity stress methods, solving two coupled first order equations [Virieux, 1986; Levander, 1988; Graves, 1996].

The main idea using a staggered grid is to calculate spatial derivatives halfway between two gridpoints. Hence, some modeling parameters are defined on intergrid locations, such that they have to be averaged or the grid values halfway between two gridpoints have to be used.

This yields in both methods mentioned above inaccurate results or instability problems when the propagation of waves in media with strong fluctuations of the elastic parameters (cracks, pores) is simulated although the von Neumann stability is fulfilled (see e.g. [Crase, 1990; Seron et al., 1996; Robertsson, 1996; Graves, 1996]). In such situations, different types of Finite Element (FE) methods or Finite Integral (FI) methods seem to be more appropriate (see, e.g., a sound study in [Fellinger et al., 1995]). The standard way to handle the quasi-infinite elastic contrast of rock/air is to apply boundary conditions described e.g. in Section 4.2, by Robertsson [1996], or by Graves [1996].

In this thesis, however, I propose a new approach to FD staggered grid modeling of the elastic wave propagation in arbitrary heterogeneous and, in principle, arbitrary anisotropic media. I start in Section 3.2 with the basic numerical procedures and requirements for the FD modeling. Based on a modification of the elementary cell, described in Section 3.3, the new approach – a rotated staggered grid – allows to model the interaction of the wavefield with voids, cracks and other high-contrast inclusions. It is also possible to incorporate complex-shaped boundaries. In principle the method does not require any hard coded boundary conditions. For example, scattering at the interface rock/air can be modeled directly using the corresponding elastic properties and densities of these materials. In Section 3.4 the discretization of derivatives of the new rotated staggered grid is given in detail for the 2D and 3D case. I perform in Section 3.5 a comprehensive standard stability and dispersion analysis for the new rotated grid for comparison with the standard staggered grid and other techniques. In the following chapter I present modeling examples in order to demonstrate the enhanced possibilities of the new rotated grid mentioned above.

3.2 Basic numerical procedures and requirements for the FD modeling

The propagation of elastic waves is described by the elastodynamic wave equation (e.g. [Aki and Richards, 1980]):

$$\rho(\mathbf{r})\ddot{u}_i(\mathbf{r}) = (c_{ijkl}(\mathbf{r})u_{k,l}(\mathbf{r}))_{,j} + f(\mathbf{r}). \quad (3.1)$$

For modeling elastic waves with finite-differences, it is necessary to discretize the stiffness tensor c_{ijkl} , the density ρ and the wavefield u_i on a grid. Calculation of $u(t + \Delta t)$ from $u(t)$ and $u(t - \Delta t)$ and maybe from the wavefield at timesteps before, when applying a Taylor time update of higher order than two, requires the following steps (when neglecting outer forces and boundary conditions):

- Calculation of the strain $\epsilon_{kl} = u_{k,l}$.
- Calculation of the stress $\sigma_{ij} = c_{ijkl}u_{k,l}$.
- Calculation of the divergence of stress $\sigma_{ij,j}$.
- Calculation of the acceleration $\ddot{u}_i = \frac{1}{\rho}\sigma_{ij,j}$.
- Performing the time update by the calculation of $u(t + \Delta t)$.

The calculation of $u(t + \Delta t)$ from $u(t)$ and $u(t - \Delta t)$ requires differentiations to calculate ϵ_{kl} from the wavefield and to determine the divergence of the stress. Also three multiplications are necessary to calculate the stress, the acceleration, and the wavefield at the time $t + \Delta t$.

The second order Taylor time update can be derived in the following way (for higher orders see Dablain [1986]):

$$u_i(\mathbf{r}, t + \Delta t) = u_i(\mathbf{r}, t) + \Delta t u_i(\mathbf{r}, t) + \frac{1}{2} \Delta t^2 \ddot{u}_i(\mathbf{r}, t) + \dots \quad (3.2)$$

$$u_i(\mathbf{r}, t - \Delta t) = u_i(\mathbf{r}, t) - \Delta t u_i(\mathbf{r}, t) + \frac{1}{2} \Delta t^2 \ddot{u}_i(\mathbf{r}, t) - \dots \quad (3.3)$$

$$(3.2) - (3.3) : \quad u_i(\mathbf{r}, t + \Delta t) + u_i(\mathbf{r}, t - \Delta t) = 2u_i(\mathbf{r}, t) + \Delta t^2 \ddot{u}_i(\mathbf{r}, t) + \dots \quad (3.4)$$

$$\Rightarrow \quad u_i(\mathbf{r}, t + \Delta t) = 2u_i(\mathbf{r}, t) - u_i(\mathbf{r}, t - \Delta t) + \Delta t^2 \ddot{u}_i(\mathbf{r}, t) \quad (3.5)$$

In the recent years, staggered grids have been developed, where derivatives belong to the central location between the points where the original parameters are given. This reduces numerical dispersion. Since the result of a differentiation in an arbitrary direction i is shifted half a grid spacing in i -direction compared with the original parameters and – for reasons of accuracy – no parameters located at different positions should be multiplied, the five operations described above constrain possible combinations of parameter locations.

3.3 Discretization of media and wavefields

For the sake of simplicity, I consider an isotropic elastic medium in two dimensions with equal grid spacing in **z**- and **x**-direction. However, the considerations in this Section are also valid for rectangular cells in three dimensions and all kinds of anisotropic elastic media.

3.3.1 Standard staggered grids

The standard way of discretization was first described by Virieux [1986], resulting in the locations of the modeling parameters for an isotropic elastic medium shown in Figure 3.1a. With regard to the above mentioned operations that are necessary to calculate the wavefield at the next timestep, all parameters are defined at the correct location. However, the density and the Lamé parameter μ are defined twice within the elementary cell. In most cases,

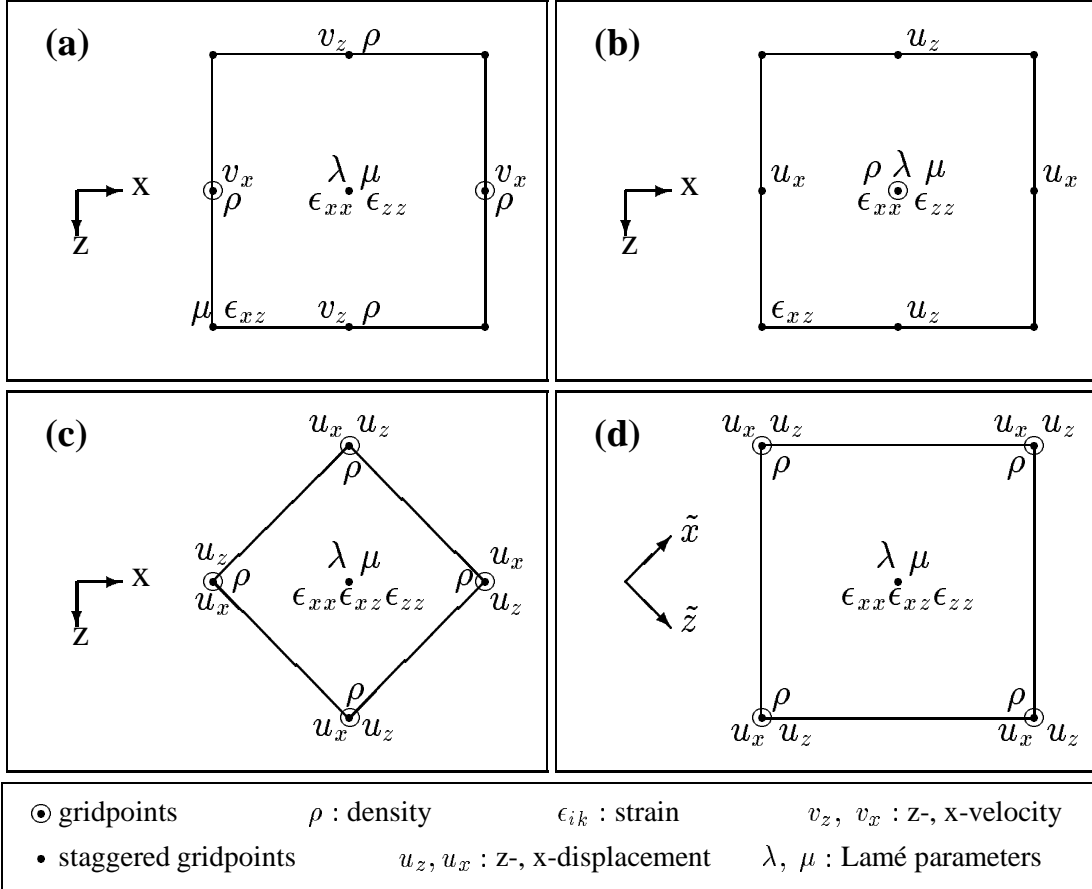


Figure 3.1: Elementary cells of different staggered grids. Locations where strains, displacement (velocity) and elastic parameters are defined. **(a)** The elementary cell defined by Virieux [1986]. Note that the velocity components are not defined at the same location. **(b)** Locations on a standard staggered grid (e.g. [Kneib and Kerner, 1993]) if no averaging of medium parameters is performed. **(c)** Locations of parameters in the elementary cell for a modified staggered grid under the conditions mentioned in the text. **(d)** Elementary cell of the new rotated staggered grid. Spatial derivatives are performed along the \tilde{x} - and \tilde{z} -axes. The wave equation and the elements of the stiffness tensor are the same as in **(b)**.

the medium consists of a rectangular grid with parameters known at the center of the cells. Therefore, it is necessary to interpolate the density and the shear modulus in the grid shown in Figure 3.1a or to take parameters from positions half a grid spacing away.

Interpolating the density causes no problem, assuming that the elementary cells are homogeneous. In this case the use of the averaged values of the cells above and below (for densities located at the same position as v_z) or left and right (densities at v_x positions) is permitted. The remaining problem of this grid is the accurate averaging of the shear modulus in the corners of the cell.

Under the additional assumptions that the elastic parameters within an elementary cell and the stress components at the surface of the cell are constant, the elastodynamic finite integration technique (EFIT) [Fellinger et al., 1995] averages the inverse shear moduli of the four cells surrounding the corner. Taking that into account, the modeling of arbitrary contrasts in the medium becomes feasible.

Another method, using parameters from positions nearby, is also often used (see e.g. [Kneib and Kerner, 1993; Karrenbach, 1995]). The main reason for using this method is that small scale medium fluctuations are not suppressed, because no averaging (or smoothing) of medium parameters has to be done. Figure 3.1b shows the elementary cell, replacing, for example, the density at the left and the lower side by the density of the center and replacing the shear modulus at the lower left corner by the shear modulus at the center.

Now, there is only one density location and one location for the Lamé parameter μ in an elementary cell. Thus, the calculation of the stress component σ_{xz} has to be done by multiplying the values of strain and stiffness defined at different positions. This leads to necessity of replacing, for example, the density at the left and the lower side by the density of the center and replacing the shear modulus at the lower left corner by the shear modulus at the center. The same difficulties arises for the calculation of the acceleration, since the density must be taken from a different location. One effect of this mismatch between positions of modeling parameters is an anisotropic behavior of the wavefield in the case of medium inhomogeneities. When the wavefield hits inhomogeneities (e.g. cracks) with high contrasts of elastic parameters or density, stability problems can occur. Here one obtain an unstable modeling of a wavefield diffraction on a crack. Note, that such stability problems exist although the von Neumann stability criterion is fulfilled.

3.3.2 The rotated staggered grid

All these problems described above can be avoided by choosing another configuration of the grid. Placing all components of the stiffness tensor at the same position within the elementary grid cell (e.g., the center), the positions of the modeling parameters are found directly as shown in Figure 3.1c.

The grid in Figure 3.1c satisfies all conditions stated in the previous section with respect to the five operations that are necessary to perform a timestep. Parameters that have to be multiplied are defined at the same location and derivatives are defined between the parameters that have to be differentiated. Since the density is not located at the same position as the stiffness tensor elements two alternatives are possible. The density can be given on an additional (staggered) grid. Another, more practical approach suggests a density averaging using the four surrounding cells. In the case of homogeneous cells or a linear behavior of the density between the stiffness locations, the density coincides with the exact density after averaging.

Other than the grids before, this grid consists of rhombus instead of rectangles. Therefore, horizontal or vertical boundaries are jagged. Since in most cases the medium parameters are discretized in quadratic or rectangular cells, a rotation of the whole grid by 45 degrees (this is possible only for the case that the grid spacing in x- and z-direction is equal) seems to be useful. However, in this case a transformation of the whole elastodynamic wave equation would be necessary. Another solution is to change only the directions of derivatives, leaving the wave equation and the stiffness tensor unchanged. Figure 3.1d shows the elementary cell of the grid obtained for this case. The directions of spatial derivatives have changed from x and z to \hat{x} and \hat{z} . In the following Section, I describe how the derivatives must be performed in the new system of coordinates. The application of the new rotated staggered grid to a model with a crack is shown in Figure 4.1 which has been obtained after several time steps. Let me point out that one cannot model this with a standard staggered grid because of strong-heterogeneity stability problems at the crack !

I found some examples in the literature where rotated differentiation operators were used (see e.g. [Stekl and Pratt, 1998; Cole, 1994; Jo et al., 1996]). The goal to apply such operators is to reduce numerical grid anisotropy. So far, I did not find publications mentioning the combination of the staggered grid technique and the usage of rotated differentiation operators.

It is important to realize that the limitation of isotropic media and of squared elementary cells can now be rejected. For an arbitrarily anisotropic medium all elements of the stiffness tensor must be located at the position of λ and μ in Figure 3.1d. Thus, the grid can be applied to all kinds of anisotropy (up to triclinic).

3.4 Discretization of derivatives of the new rotated staggered grid

3.4.1 2D case

In the case of a grid with rectangular elementary cells of length Δz and Δx , one yields for the new derivative directions (in two dimensions):

$$\tilde{\mathbf{z}} = \frac{\Delta x}{\Delta r} \mathbf{x} + \frac{\Delta z}{\Delta r} \mathbf{z}, \quad (3.6)$$

$$\begin{aligned} \tilde{\mathbf{x}} &= \frac{\Delta x}{\Delta r} \mathbf{x} - \frac{\Delta z}{\Delta r} \mathbf{z}, \\ \Delta r &= \sqrt{\Delta z^2 + \Delta x^2}. \end{aligned} \quad (3.7)$$

Since the new derivative directions $\tilde{\mathbf{z}}$ and $\tilde{\mathbf{x}}$ replace the old directions \mathbf{z} and \mathbf{x} , it is necessary to express derivatives along old directions by a linear combination of derivatives along the new directions.

$$\frac{\partial}{\partial z} = \frac{\Delta r}{2\Delta z} \left(\frac{\partial}{\partial \tilde{z}} - \frac{\partial}{\partial \tilde{x}} \right), \quad (3.8)$$

$$\frac{\partial}{\partial x} = \frac{\Delta r}{2\Delta x} \left(\frac{\partial}{\partial \tilde{z}} + \frac{\partial}{\partial \tilde{x}} \right). \quad (3.9)$$

In order to perform numerical simulations, one must define differentiation operators D_x and D_z that perform the derivatives $\frac{\partial}{\partial x}$ and $\frac{\partial}{\partial z}$. The conventional 2nd order operators that perform derivatives in \mathbf{x} - and \mathbf{z} -directions are:

$$D_x u(z, x, t) = \frac{1}{\Delta x} \left[u \left(z, x + \frac{\Delta x}{2}, t \right) - u \left(z, x - \frac{\Delta x}{2}, t \right) \right], \quad (3.10)$$

$$D_z u(z, x, t) = \frac{1}{\Delta z} \left[u \left(z + \frac{\Delta z}{2}, x, t \right) - u \left(z - \frac{\Delta z}{2}, x, t \right) \right]. \quad (3.11)$$

Analogous to equation (3.10) and (3.11) it is possible to define the differentiation operators $D_{\tilde{x}}$ and $D_{\tilde{z}}$ for the derivatives $\frac{\partial}{\partial \tilde{x}}$ and $\frac{\partial}{\partial \tilde{z}}$ in $\tilde{\mathbf{x}}$ - and $\tilde{\mathbf{z}}$ -direction:

$$D_{\tilde{x}} u(z, x, t) = \frac{1}{\Delta r} \left[u \left(z - \frac{\Delta z}{2}, x + \frac{\Delta x}{2}, t \right) - u \left(z + \frac{\Delta z}{2}, x - \frac{\Delta x}{2}, t \right) \right], \quad (3.12)$$

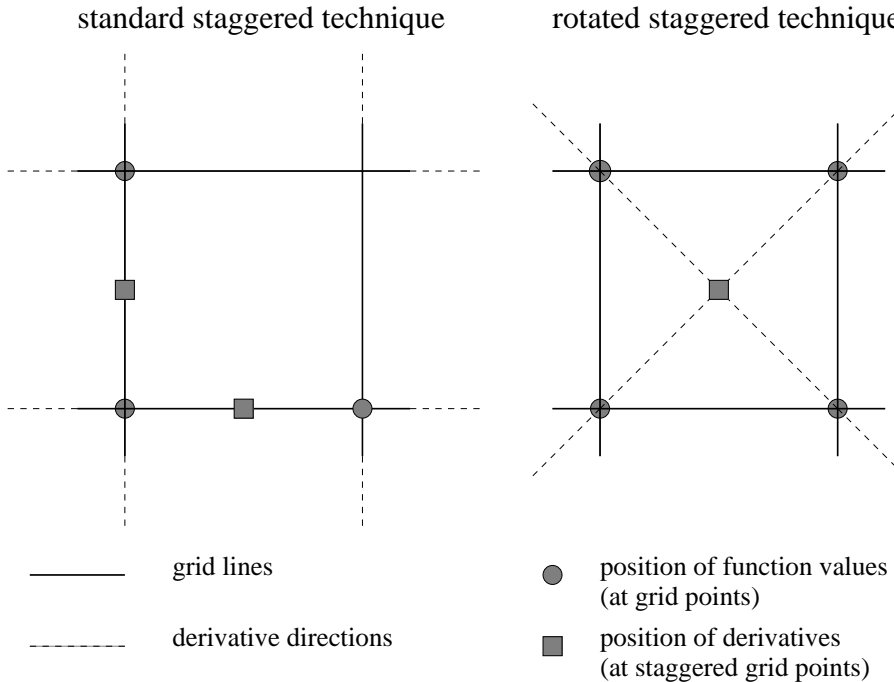


Figure 3.2: This figure illustrates the shift of the position of the derivative from the standard staggered grid technique to the rotated staggered grid technique (2D case). The technique makes use of the well known formula $\frac{\delta f}{\delta \mathbf{m}}(P_0) = \mathbf{grad}f(P_0) \cdot \mathbf{m}$ to calculate the derivatives in the old directions (axes).

$$D_z u(z, x, t) = \frac{1}{\Delta r} \left[u\left(z + \frac{\Delta z}{2}, x + \frac{\Delta x}{2}, t\right) - u\left(z - \frac{\Delta z}{2}, x - \frac{\Delta x}{2}, t\right) \right]. \quad (3.13)$$

With equations (3.8), (3.9), (3.12) and (3.13), numerical differentiation operators are obtained that perform the spatial derivatives in \mathbf{z} - and \mathbf{x} -direction in the new grid (i.e., using the new derivative directions):

$$\frac{\partial}{\partial z} u(z, x, t) \approx \frac{\Delta r}{2\Delta z} (D_{\tilde{z}} u(z, x, t) - D_{\tilde{x}} u(z, x, t)), \quad (3.14)$$

$$\frac{\partial}{\partial x} u(z, x, t) \approx \frac{\Delta r}{2\Delta x} (D_{\tilde{z}} u(z, x, t) + D_{\tilde{x}} u(z, x, t)). \quad (3.15)$$

Instead of a 2nd order differentiation operator (equations (3.10) to (3.13)), the use of higher order operators is possible. Equation (3.14) and (3.15) remain unchanged.

3.4.2 3D case

For the 3-dimensional case the necessary derivative directions are:

$$\tilde{\mathbf{d}}_1 = \frac{\Delta x}{\Delta l} \mathbf{x} + \frac{\Delta z}{\Delta l} \mathbf{z} + \frac{\Delta y}{\Delta l} \mathbf{y}, \quad (3.16)$$

$$\tilde{\mathbf{d}}_2 = \frac{\Delta x}{\Delta l} \mathbf{x} - \frac{\Delta z}{\Delta l} \mathbf{z} + \frac{\Delta y}{\Delta l} \mathbf{y}, \quad (3.17)$$

$$\tilde{\mathbf{d}}_3 = \frac{\Delta x}{\Delta l} \mathbf{x} + \frac{\Delta z}{\Delta l} \mathbf{z} - \frac{\Delta y}{\Delta l} \mathbf{y}, \quad (3.18)$$

$$\tilde{\mathbf{d}}_4 = \frac{\Delta x}{\Delta l} \mathbf{x} - \frac{\Delta z}{\Delta l} \mathbf{z} - \frac{\Delta y}{\Delta l} \mathbf{y}, \quad (3.19)$$

$$\Delta l = \sqrt{\Delta z^2 + \Delta x^2 + \Delta y^2}.$$

With an analogous calculation as in the 2D case I receive the following result for the derivatives in **z**-, **x**- and **y**-direction:

$$\frac{\partial}{\partial x} u(z, x, y, t) \approx \frac{\Delta l}{4\Delta x} (D_{\tilde{d}_1} + D_{\tilde{d}_2} + D_{\tilde{d}_3} + D_{\tilde{d}_4}) u(z, x, y, t), \quad (3.20)$$

$$\frac{\partial}{\partial y} u(z, x, y, t) \approx \frac{\Delta l}{4\Delta y} (D_{\tilde{d}_1} + D_{\tilde{d}_2} - D_{\tilde{d}_3} - D_{\tilde{d}_4}) u(z, x, y, t), \quad (3.21)$$

$$\frac{\partial}{\partial z} u(z, x, y, t) \approx \frac{\Delta l}{4\Delta z} (D_{\tilde{d}_1} - D_{\tilde{d}_2} + D_{\tilde{d}_3} - D_{\tilde{d}_4}) u(z, x, y, t). \quad (3.22)$$

Therefore, each derivative in **z**-, **x**- and **y**-direction is replaced by a linear combination of four derivatives.

At a first glance, a disadvantage of the method described above is the increased computing time, since one derivative along a direction of the previous coordinate system (**x**, **z** or **y**) is replaced by a linear combination of two (or four, 3D case) derivatives along the new directions \tilde{z} and \tilde{x} (or \tilde{d}_1 , \tilde{d}_2 , \tilde{d}_3 and \tilde{d}_4 , 3D case). However, the result of a differentiation along a new direction can be used to calculate derivatives along all old axes. For example, to yield the derivative of a parameter in **z**-direction, it is necessary to calculate the derivatives along the \tilde{z} - and \tilde{x} -direction. Both derivatives can be also used for calculating the derivative of the parameter in **x**-direction. Hence, computation time remains the same.

3.5 Stability and dispersion

Since FD modeling approximates derivatives by numerical operators and uses Taylor polynomials to perform the time update, inaccuracies occur, especially for coarse grids. One can separate these numerical errors into amplitude and phase errors. For a plane wave propagating through an infinite, isotropic and homogeneous medium, the amplitude must be conserved, and the velocity of propagation is not frequency-dependent. In FD modeling, it is possible that the amplitude increases exponentially with every timestep. In this case, the modeling scheme is said to be unstable. Frequency-dependent velocity errors, also called numerical dispersion, cannot be excluded completely but can be estimated and, therefore, reduced to a known and acceptable degree. The goal of this section is to make a standard von Neumann style analysis (see e.g. [von Neumann, 1943; O'Brien et al., 1951; Marfurt, 1984; Smith, 1985; Dablain, 1986; Virieux, 1986; Levander, 1988; Crase, 1990; Kneib and Kerner, 1993; Stekl and Pratt, 1998; Moczo et al., 2000]) for the new rotated staggered grid. The resulting von Neumann stability criterion and the dispersion error are compared with that for the standard staggered grid.

Note, that the von Neumann stability criterion is not in connection with the stability problems for high contrast inclusions. In a bounded and arbitrary heterogeneous media many wave modes (e.g. surface waves) exist and the analysis of numerical errors and stability is going to be extremely complicated. A general recipe of the problems associated with such an analysis can be found in Marfurt [1984]. The work of van Vossen et al. [2000] is an approach to discuss such problem from the experimental point of view. As mentioned in Crase [1990], stability limits and error analysis of finite-difference schemes which include anisotropy and attenuation has never been performed.

3.5.1 Neumann Stability

A way to derive the stability criterion of the grid is the method of von Neumann [von Neumann, 1943; O'Brien et al., 1951; Smith, 1985], using a time-harmonic plane wave ansatz for the wavefield:

$$u_i(z, x, y, t) = u_i(0, 0, 0, 0) e^{i(k_z z + k_x x + k_y y)} e^{-i\omega t}. \quad (3.23)$$

The propagation of the wavefield in a homogeneous unbounded medium can be described in matrix form:

$$\mathbf{U}(t + \Delta t) = \mathbf{A} \mathbf{U}(t). \quad (3.24)$$

In this equation, vector \mathbf{U} denotes some kind of generalized wavefield, containing all wavefield parameters that are necessary to calculate the next timestep. The modeling is stable if the absolute values of the eigenvalues of matrix \mathbf{A} are not larger than 1.

In the following a homogeneous, isotropic and unbounded medium is considered. The calculation is done for a FD scheme with time update in 2nd order. This provides the following expression for the wavefield:

$$u_i(t + \Delta t) = 2u_i(t) - u_i(t - \Delta t) + \Delta t^2 \ddot{u}_i(t). \quad (3.25)$$

Equation (3.25) contains the wavefield at three different times. To get an expression equivalent to equation (3.24), the generalized wavefield must be a function of the wavefield at two timesteps.

Equation (3.25) can be written in the form of equation (3.24), using

$$(\mathbf{U}(t))^T = (u_z(t), u_x(t), u_y(t), u_z(t - \Delta t), u_x(t - \Delta t), u_y(t - \Delta t))$$

and

$$\mathbf{A} = \begin{pmatrix} 2 + \Delta t^2 \left(\frac{\partial}{\partial t} \right)^2 & 0 & 0 & -1 & 0 & 0 \\ 0 & 2 + \Delta t^2 \left(\frac{\partial}{\partial t} \right)^2 & 0 & 0 & -1 & 0 \\ 0 & 0 & 2 + \Delta t^2 \left(\frac{\partial}{\partial t} \right)^2 & 0 & 0 & -1 \\ 1 & 0 & 0 & 0 & 0 & 0 \\ 0 & 1 & 0 & 0 & 0 & 0 \\ 0 & 0 & 1 & 0 & 0 & 0 \end{pmatrix}. \quad (3.26)$$

The 2nd order time derivations must be replaced by expressions that include spatial derivatives using the elastic wave equation (3.1). Then a matrix equation is obtained, where the matrix \mathbf{A} with the elements A_{ij} has zero entries for i and $j > 3$ and contains the shear and compressional wave velocity. The next step is to apply the 3D differentiation operators to the plane wave in equation (3.23). I obtain the following result for the case of 2nd order spatial differentiations for a plane wave:

$$D_{zz} u = \frac{-4}{\Delta z^2} X_2^2 X_3^2 X_5^2 u, \quad D_{zx} u = \frac{-4}{\Delta x \Delta z} X_1 X_2 X_3 X_4 X_5^2 u, \quad (3.27)$$

$$D_{xz} u = \frac{-4}{\Delta x^2} X_1^2 X_4^2 X_5^2 u, \quad D_{zy} u = \frac{-4}{\Delta y \Delta z} X_1 X_2 X_3^2 X_5 X_6 u, \quad (3.28)$$

$$D_{yy} u = \frac{-4}{\Delta y^2} X_1^2 X_3^2 X_6^2 u, \quad D_{xy} u = \frac{-4}{\Delta x \Delta y} X_1^2 X_3 X_4 X_5 X_6 u \quad (3.29)$$

with abbreviations:

$$\begin{aligned} X_1 &= \cos\left(\frac{k_z \Delta z}{2}\right), & X_3 &= \cos\left(\frac{k_x \Delta x}{2}\right), & X_5 &= \cos\left(\frac{k_y \Delta y}{2}\right), \\ X_2 &= \sin\left(\frac{k_z \Delta z}{2}\right), & X_4 &= \sin\left(\frac{k_x \Delta x}{2}\right), & X_6 &= \sin\left(\frac{k_y \Delta y}{2}\right). \end{aligned}$$

Thus, using equations (3.27) - (3.29) and the elastic wave equation, matrix \mathbf{A} in equation (3.24) can be calculated.

As mentioned above, the eigenvalues of \mathbf{A} have to be not larger than 1. The calculation of the eigenvalues provides the following condition for the case of 2nd order spatial differentiations that have to be satisfied:

$$\Delta t^2 v_{p,s}^2 \left(\frac{X_2^2 X_3^2 X_5^2}{\Delta z^2} + \frac{X_1^2 X_4^2 X_5^2}{\Delta x^2} + \frac{X_1^2 X_3^2 X_6^2}{\Delta y^2} \right) \leq 1. \quad (3.30)$$

Since the S-wave velocity is always smaller than the P-wave velocity, it is possible to take the P-wave velocity in equation (3.30) as the stronger condition to be satisfied. Assuming the worst case for the values of X_1 up to X_6 and for equal grid spacing ($\Delta h = \Delta x = \Delta y = \Delta z$) a simple stability criterion is yielded:

$$\frac{\Delta t v_p}{\Delta h} \leq 1. \quad (3.31)$$

With an analogous calculation (but with very long expressions) I can give the result for $(2n)$ -th order spatial differentiations. For the new rotated grid the stability criterion for the 3D case and the 2D case are the same. I obtain:

$$\frac{\Delta t v_p}{\Delta h} \leq 1 / \left(\sum_{k=1}^n |c_k| \right). \quad (3.32)$$

In this equation c_k denotes the difference coefficients (e.g. Holberg coefficients [Holberg, 1987; Kindelan et al., 1990]). This result yields the von Neumann stability criterion for the new rotated grid for all wavenumbers.

For the standard staggered grid the following criteria can be obtained (for 3D case see [Virieux, 1986; Rodrigues and Mora, 1992], for 2D case see [Kneib and Kerner, 1993; Virieux, 1986; Levander, 1988; Crase, 1990]):

$$\frac{\Delta t v_p}{\Delta h} \leq 1 / (\sqrt{3} \sum_{k=1}^n |c_k|) \quad (3D \text{ case}), \quad (3.33)$$

$$\frac{\Delta t v_p}{\Delta h} \leq 1 / (\sqrt{2} \sum_{k=1}^n |c_k|) \quad (2D \text{ case}). \quad (3.34)$$

Note, that these stability considerations are valid only in the case of homogeneous media and for 2nd order operator in time.

A comparison with EFIT [Fellinger et al., 1995] and the standard staggered grid for 2nd order spatial differentiations shows that the stability criteria are exactly the same. As shown above, the stability condition for the new rotated grid is less restrictive. This corresponds to the fact that the spatial differentiation directions of the new rotated grid enlarge the spacing between the gridpoints.

3.5.2 Dispersion relation

To determine the dispersion relation, the 2nd order time update and a time harmonic plane wave are used again:

$$u_i(t + \Delta t) - 2u_i(t) + u_i(t - \Delta t) - \Delta t^2 \ddot{u}_i(t) = 0. \quad (3.35)$$

Splitting the wavefield into a part with spatial dependency and a part containing the variation in time, yields

$$u_i(\mathbf{r}, t) = u_i(\mathbf{r}) e^{-i\hat{\omega}t}. \quad (3.36)$$

Combining equation (3.36) and (3.35), an equation for $u_i(z, x, y)$ is obtained:

$$\begin{aligned} 0 &= \left(e^{-i\hat{\omega}\Delta t} - 2 + e^{i\hat{\omega}\Delta t} \right) u_i(z, x, y) - \Delta t^2 \ddot{u}_i(z, x, y) \\ &= \left(-4 \sin^2 \left(\frac{\hat{\omega}\Delta t}{2} \right) - \Delta t^2 \frac{d^2}{dt^2} \right) u_i(z, x, y). \end{aligned} \quad (3.37)$$

Analogous to the calculation of the stability criterion, I use the elastodynamic wave equation (3.1) to find the expressions for \ddot{u}_i . The following matrix equation is derived:

$$\mathbf{B} \mathbf{u} = 0, \quad (3.38)$$

where B_{ij} are the elements of a 3 x 3 matrix. Since the wavefield in equation (3.38) has to be different from zero, matrix \mathbf{B} has to satisfy

$$\det(\mathbf{B}) = 0. \quad (3.39)$$

Splitting the determinant into three multiplicative factors yields dispersion equations for the P-wave and the S-wave. For the case of 2nd order spatial differentiations, I obtain for the new rotated staggered grid (for 4th order spatial differentiations see Equation A.1):

$$\begin{aligned} \sin^2\left(\frac{\hat{\omega}\Delta t}{2}\right) &= \frac{\Delta t^2 v_{p,s}^2}{\Delta z^2} \sin^2\left(\frac{k_z \Delta z}{2}\right) \cos^2\left(\frac{k_x \Delta x}{2}\right) \cos^2\left(\frac{k_y \Delta y}{2}\right) \\ &+ \frac{\Delta t^2 v_{p,s}^2}{\Delta x^2} \cos^2\left(\frac{k_z \Delta z}{2}\right) \sin^2\left(\frac{k_x \Delta x}{2}\right) \cos^2\left(\frac{k_y \Delta y}{2}\right) \\ &+ \frac{\Delta t^2 v_{p,s}^2}{\Delta y^2} \cos^2\left(\frac{k_z \Delta z}{2}\right) \cos^2\left(\frac{k_x \Delta x}{2}\right) \sin^2\left(\frac{k_y \Delta y}{2}\right). \end{aligned} \quad (3.40)$$

The analogous calculation for the 2D case and for 2nd order spatial differentiations gives (for 8th order spatial differentiations see Equation A.2):

$$\begin{aligned} \sin^2\left(\frac{\hat{\omega}\Delta t}{2}\right) &= \frac{\Delta t^2 v_{p,s}^2}{\Delta z^2} \sin^2\left(\frac{k_z \Delta z}{2}\right) \cos^2\left(\frac{k_x \Delta x}{2}\right) \\ &+ \frac{\Delta t^2 v_{p,s}^2}{\Delta x^2} \cos^2\left(\frac{k_z \Delta z}{2}\right) \sin^2\left(\frac{k_x \Delta x}{2}\right). \end{aligned} \quad (3.41)$$

Other than for the stability, where a modeling scheme is stable if the stability condition is satisfied, numerical dispersion can only be reduced to some degree. Therefore, the dispersion relations (e.g. equation (3.40) and (3.41)) enable one to consider the effect of numerical dispersion.

Focus on the fact that the dispersion relations for the new rotated staggered grid are independent of any value of the Poisson ratio. This allows to handle the liquid-solid contact without applying boundary conditions (see e.g. [Virieux, 1986; Crase, 1990]). Note, not all modeling algorithms yield satisfactory results for high Poissons ratios [Kerner, 1990]. This is explicitly the case for centered finite-difference schemes [Marfurt, 1984].

3.5.3 Dispersion analysis

For the dispersion analysis (similar to [Virieux, 1986; Crase, 1990; Marfurt, 1984]) I define a dispersion parameter γ given by

$$\gamma = v_{ph} \frac{\Delta t}{\Delta h}. \quad (3.42)$$

The maximum values for γ are associated with the stability criteria. They are given for the different cases by the absolute values of the right-hand sides of inequalities (3.32), (3.33) and (3.34). The quantity H given by

$$H = \Delta h / \lambda = \frac{k \Delta h}{2\pi} \quad (3.43)$$

controls the number of nodes per wavelength of the plane wave. The maximum value of H is 0.5 given by the Nyquist-theorem. To obtain the relative accuracy of the phase velocity A_{rel} as a function of the quantity H , the dispersion parameter γ and the direction of wave propagation (ϑ, φ) , I define:

$$\begin{aligned} A_{rel}(H, \gamma, \varphi, \vartheta) &:= \frac{v_{ph, numerical}}{v_{ph}} \\ &= \frac{\hat{\omega}(kx, ky, kz, \Delta h, v_{ph}, \Delta t, c_1, c_2, \dots, c_n)}{v_{ph} |\vec{k}|} \end{aligned} \quad (3.44)$$

with:

$$\begin{aligned} kx &= H \frac{2\pi}{\Delta h} \sin \varphi \sin \vartheta, \\ kz &= H \frac{2\pi}{\Delta h} \cos \varphi \sin \vartheta, \\ ky &= H \frac{2\pi}{\Delta h} \cos \vartheta, \\ \varphi &\in [0, 2\pi], \vartheta \in [0, \pi], \\ \Delta t &= \gamma \frac{\Delta h}{v_{ph}}. \end{aligned}$$

Note that $\hat{\omega}(kx, ky, kz, \Delta h, v_{ph}, \Delta t, c_1, c_2, \dots, c_n)$ is given from the dispersion relations (see Section 3.5.2 or for the standard staggered grid in [Cruse, 1990; Rodrigues and Mora, 1992]).

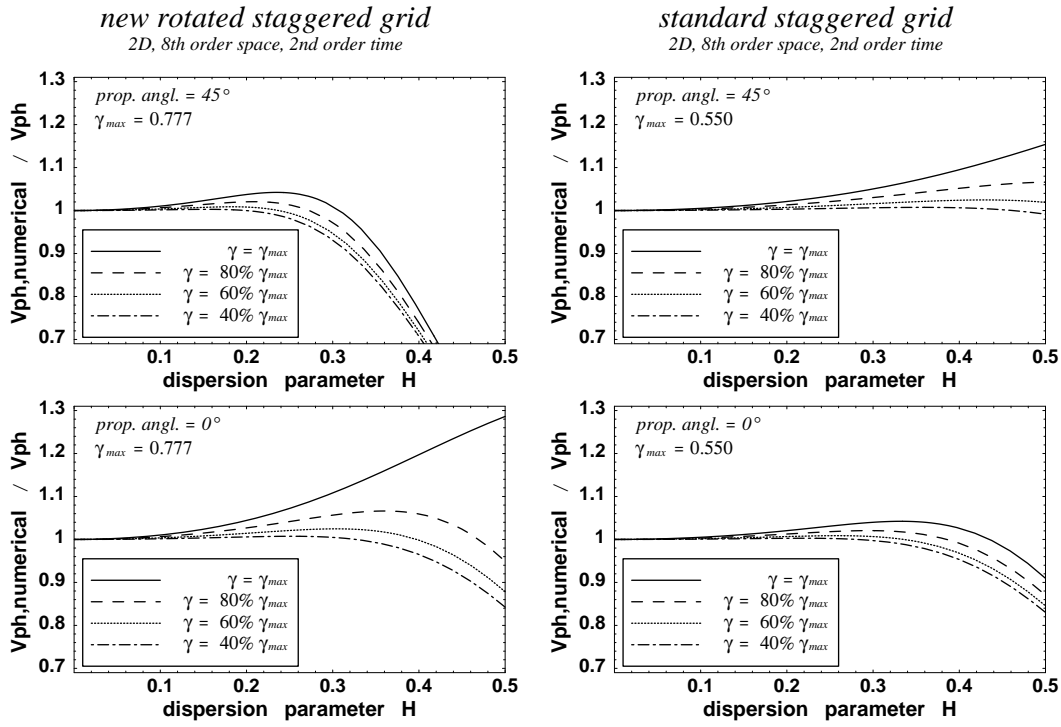


Figure 3.3: Curves showing modeling errors caused by numerical dispersion for the new rotated staggered grid (left side) and the standard staggered grid (right side) for the 2D case ($\vartheta = \pi/2$). In the top row the angle between the direction of wave propagation and the axes is 45 degrees ($\varphi = \pi/4$). For the bottom row the angle is 0 degree ($\varphi = 0$). In each plot γ varies from γ_{max} (top) to 40% of γ_{max} (bottom) in steps of 20%. All curves are calculated for 8th order spatial differentiations using Central Limit coefficients [Karrenbach, 1995] (similar to Holberg coefficients [Holberg, 1987; Kindelan et al., 1990]) and 2nd order time update. Note that γ_{max} has different values for the different grids (see Section 3.5.3).

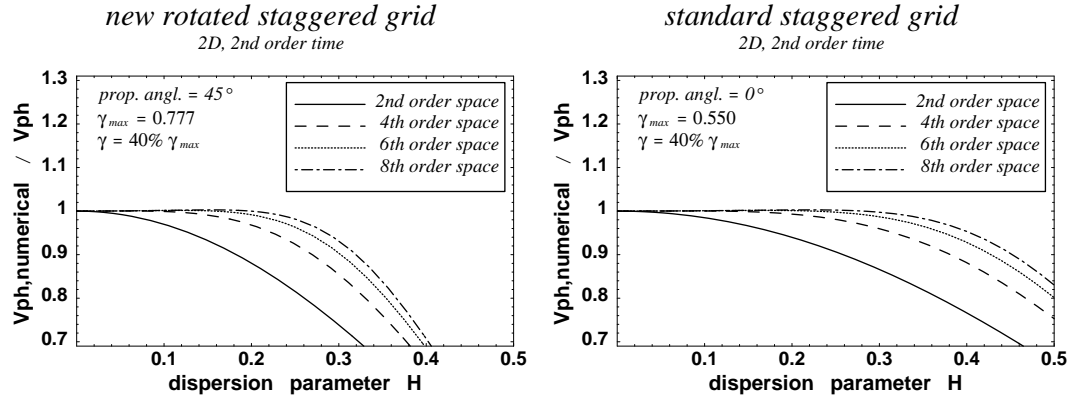


Figure 3.4: Curves showing modeling errors caused by numerical dispersion for the new rotated staggered grid (left side) and the standard staggered grid (right side) for the 2D case ($\vartheta = \pi/2$). The angle between the direction of wave propagation and the axes is 45 degrees ($\varphi = \pi/4$) on the left and 0 degree ($\varphi = 0$) on the right side. In each plot the order of spatial differentiations varies from 8 (top) to 2 (bottom) in steps of 2. All curves are calculated with Central Limit coefficients [Karrenbach, 1995; Kindelan et al., 1990] and 2nd order time update. γ is set to 40 % of γ_{max} .

2D case

In the following, I compare the numerical dispersion of the new rotated grid with that for the standard staggered grid. First, I have a closer look at the 2D case ($\vartheta = \pi/2$).

There are different ways to reduce numerical dispersion for a given FD-scheme. I concentrate on the following possibilities:

- Calculate with large wavelength with respect to the grid spacing (minimizing H).
- Calculate with a small dispersion parameter γ with respect to γ_{max} .
- Calculate with high order spatial differentiations (2nd, 4th, 6th, ...).

Figure 3.3 and 3.4 show the relative phase velocity error for the new rotated staggered grid for different cases. For comparison, the relative phase velocity error is given in dependence of the same parameters for the standard staggered grid in the same Figures. It is easy to see that the three possibilities described above work for both grids. The particularity of the rotated grid is in the following. In general the maximum error of phase velocity is in the direction of 45 degrees to the axes and not along the axes as for the standard staggered grid.

If one compare a calculation with exactly the same values of H and γ for both grids one can see exactly the same errors on the axes but different maximum phase velocity errors (see Figure, 3.5 left side).

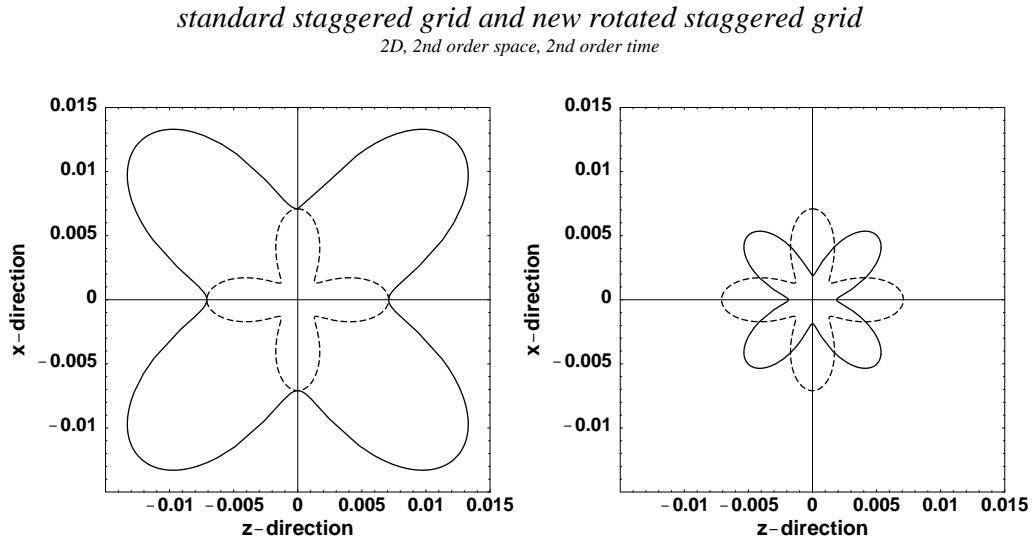


Figure 3.5: The spatial variation of the relative error of the phase velocity for the new rotated staggered grid (solid lines), and the standard staggered grid (dotted lines) is depicted. The computation is done for 2nd order spatial differentiations and 2nd order time update (2D case). The distance between the curve and the origin has the value $|A_{rel} - 1|$ (see Section 3.5.3) of the corresponding direction. In each Figure γ' and H' belong to the new rotated grid and γ and H to the standard staggered grid. Figure on the left side: $\gamma' = \gamma$ ($= 80\% \cdot \gamma_{max}$), $H' = H$ ($= 0.1$). Figure on the right side: $\gamma' = \sqrt{2} \cdot \gamma$ ($= 80\% \cdot \gamma'_{max}$), $H' = 1/\sqrt{2} \cdot H$ ($= 1/\sqrt{2} \cdot 0.1$).

But if H is decreased by a factor of $1/\sqrt{2}$ and γ increased by a factor of $\sqrt{2}$ for a calculation with the new rotated staggered grid the same maximum phase velocity errors (see Figure 3.5, right side) are obtained. This is valid for spatial differentiations of arbitrary order. The only difference is that the maximum error of phase velocity is in another direction (as mentioned above). Let us note that only for the case of 2nd order spatial differentiations the maximum error for the same values of H and γ have the ratio two. Two possibilities exist in order to receive the same accuracy for the new rotated staggered grid and for the standard staggered grid. The first one is to refine the grid by a factor of $1/\sqrt{2}$ ($\Delta h_{new} = 1/\sqrt{2} \Delta h_{old}$). The second is to increase the number of gridpoints per wavelength by a factor of $\sqrt{2}$. The advantage in this case is the computation of larger timesteps (factor of $\sqrt{2}$).

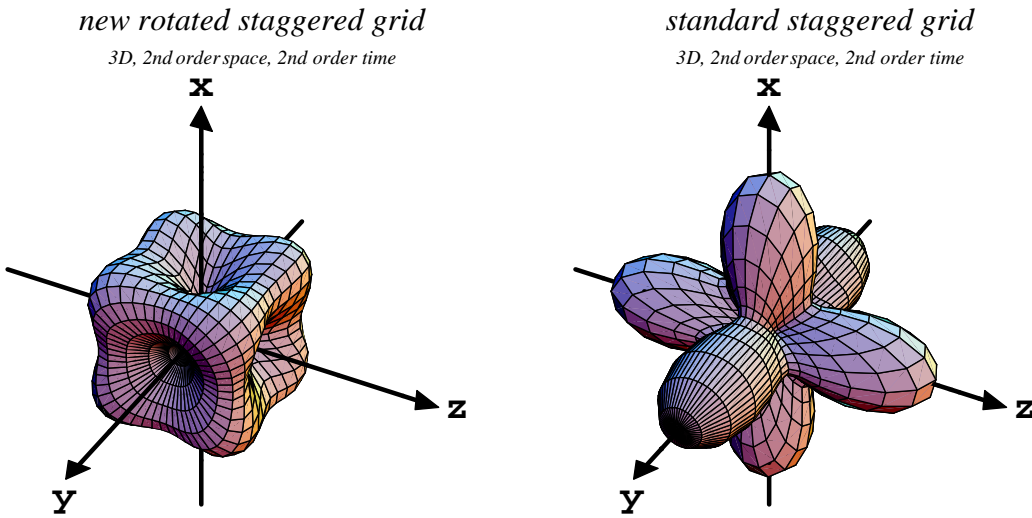


Figure 3.6: The spatial variation of the relative error of the phase velocity (compare with Figure 3.5) for the new rotated grid (left side), and the standard staggered grid (right side) is depicted. The computation is done for 2nd order spatial differentiations and 2nd order time update (3D case). Figure on the left side (new rotated staggered grid): $\gamma' = 80\% \gamma'_{max}$, $H' = 0.1$. Figure on the right side (standard staggered grid): $\gamma = 80\% \gamma_{max} = 1/\sqrt{3} \cdot \gamma'$, $H = H' \cdot \sqrt{3}$. Note that the maximum phase velocity error of the new rotated staggered grid shown in this figure is 2.82%. This is less than the maximum error of the standard staggered grid (3.93%).

3D case

Now, I have a closer look at the 3D case. I compare the phase velocity error for the new rotated staggered grid with the parameters γ' and H' with the error of the standard staggered grid with the parameters γ and H (see Figure 3.6).

They are related as follows: $\gamma = 1/\sqrt{3} \gamma'$ and $H = \sqrt{3} H'$. I found that in this case the maximum error of the new rotated grid is always lower than for the standard staggered grid. Consequently the same can be performed as in the 2D case using a factor $\sqrt{2}$, but now with a factor $\sqrt{3}$ for the 3D case.

3.6 Conclusions

Since FD modeling discretizes the medium and the wavefield on a grid and not by finite volumes (like, e.g., Finite Element schemes), it requires very few assumptions. If the discretization is done correctly, FD modeling is very fast and accurate. I find that the problem of arbitrary high contrasts of the medium parameters cannot be solved with a standard staggered grid. The grid modifications found in this paper make it possible. Moreover, it enables one to model arbitrary inhomogeneities without boundary conditions. In contrast to a standard staggered grid high-contrast inclusions do not cause instability problems for the rotated staggered grid. With a von Neumann style analysis I showed that the new rotated staggered grid has accuracy criteria and limitations similar to those of the standard staggered grid.

Chapter 4

Applications of the rotated staggered finite-difference grid

In this chapter I want to demonstrate the wide range of applications of the rotated staggered finite-difference grid.

For example it can be applied for:

- 2D crack modeling
- Free-surface modeling in the presence of topography
- 3D modeling of aluminum
- 3D modeling of Lamb waves in thin plates
- Modeling transversely isotropic media
- Modeling elastic waves in concrete

This applications are shown in the following sections.

This chapter is based on: [Saenger et al., 1999c, 2000a,b]

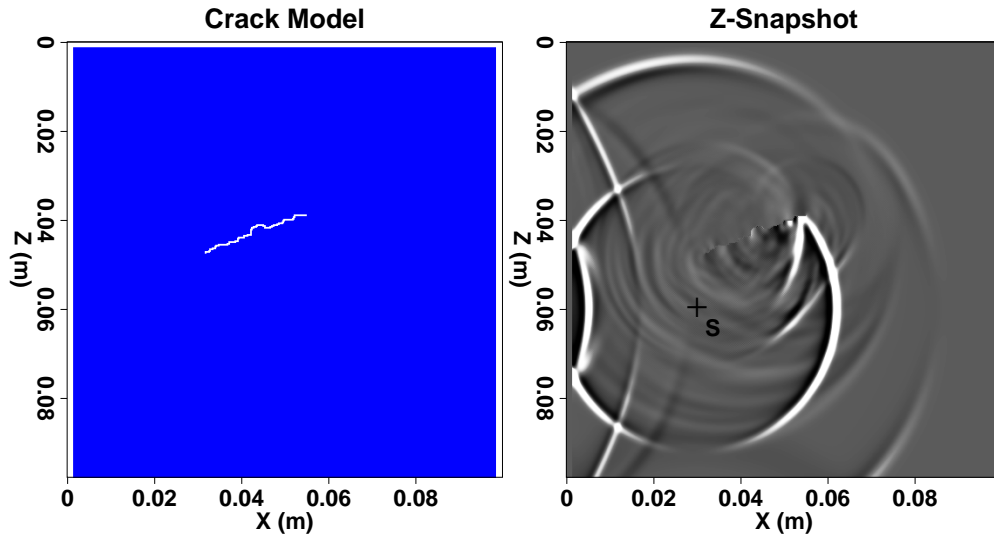


Figure 4.1: Modeling result (right side) for the 2D model shown on the left side. The new rotated staggered grid was used and a stable result was obtained. Compressional and shear waves and the influence of the crack and the boundaries can be seen very well. For details of the modeling see Section 4.1.

4.1 Example 1: 2D crack modeling

In the first example I created a relatively simple 2D crack model. I want to demonstrate that the new rotated grid can model cracks and the high contrasts at the three ('free') surfaces in the model (Figure 4.1) in 2D very well. Additionally, I show that standard exponential damping boundaries (see e.g. [Karrenbach, 1995]), applied at the bottom of the model, can be implemented. Other possibilities to implement absorbing boundary conditions can be found e.g. in Cerjan et al. [1985] or Clayton and Engquist [1977]. The model (gridspacing $\Delta h = 0.0002\text{m}$) consists of a $10\text{cm} \times 10\text{cm}$ area in which the compressional and shear wave velocity is set to $3950\frac{\text{m}}{\text{s}}$ and $2244\frac{\text{m}}{\text{s}}$; the density is $2.172\frac{\text{g}}{\text{cm}^3}$. In three directions around this area and in the crack I set the velocities to zero and the density to $0.000001\frac{\text{g}}{\text{cm}^3}$ (compare with Section 4.3). A body force source ($f_{fund} = 8 \cdot 10^5 \frac{1}{\text{s}}$, $f_{max} \approx 2.5 \cdot 10^6 \frac{1}{\text{s}}$, $\Delta t = 7 \cdot 10^{-9}\text{s}$) in \mathbf{z} -direction is placed at the point 'S'. The modeling is done with 2nd order time update and with a combination of 2nd and 8th order spatial differentiation operators [Gold et al., 1997]. I find that in general the modification of the grid enhances the stability for high medium contrasts for every order of the space differentiation operator. For the, in principle, arbitrary high contrasts at the crack and at the three interfaces of the area described above I apply 2nd order spatial differentiation operators. In order to increase the accuracy of the modeling I applied at the other grid points of the model 8th order spatial differentiation operators.

4.2 Example 2: Free-surface modeling in the presence of topography

In this second example, I want to demonstrate that the rotated staggered finite-difference technique is a powerful tool to model exploration surveys with surface topography. Obviously, the earth's surface is far from flat. Since this is usually the location at which seismic observations are made, topography may have a significant influence on recorded data. As mentioned in chapter 3 topography does not pose a problem for finite-element methods. The ability to model complicated and irregular boundary conditions is one of the principal advantages of such methods. Finite-element methods are, however, rarely used to simulate seismic wave propagation problems because of the excessive computational costs in comparison with explicit finite-difference schemes [Strang and Fix, 1973; Cohen et al., 1993].

Because the air-solid earth interface exhibits the strongest possible impedance contrast (of seismic modeling), modeling the topography along such a free surface is significant. For finite-difference modeling of horizontal free surfaces, several authors have employed the implicit condition of Vidale and Clayton [1986], which although stable is limited to second-order accuracy. In a staggered scheme [Virieux, 1986], the free-surface condition becomes explicit, but problems with accuracy and convergence may arise. Levander [1988] proposed an alternative flat free-surface implementation based on a so-called image method.

Jih et al. [1988] described a finite-difference method in which irregular free surfaces are decomposed into segments approximated by piecewise continuous lines. Following a predefined classification scheme, the different segments are treated using a one-sided difference approximation of the free-surface condition. Frankel and Leith [1992] modeled the topographic effects on seismic waves generated by a hypothetical nuclear explosion at a Russian test site. Surface topography in the finite-difference grid was modeled using a vacuum to solid density taper. Although the method is simply to apply, it was not thoroughly benchmarked and likely requires a densely sampled wave field to yield accurate results. Fornberg [1988] presented a pseudo spectral scheme in which the interior of the finite-difference grid is deformed to match exactly smooth internal boundaries. Tessmer et al. [1992] and Carcione and Wang [1993] employed an elegant solution to the free-surface problem by isolating the incoming characteristic modes near the surface and calculating the outgoing modes by scaling the incoming modes in accordance with the impedance contrast. By combining this pseudo spectral technique with the scheme presented in Fornberg [1988], they accurately modeled wave propagation near a free surface with topography. Hestholm and Ruud [1994] used Fornberg's [1988] technique and a free-surface condition similar to that of Vidale and Clayton [1986] to model wave propagation in the presence of topography on a staggered finite-difference grid. Based on an image method another approach for modeling irregular free-surfaces is presented in Robertsson [1996].

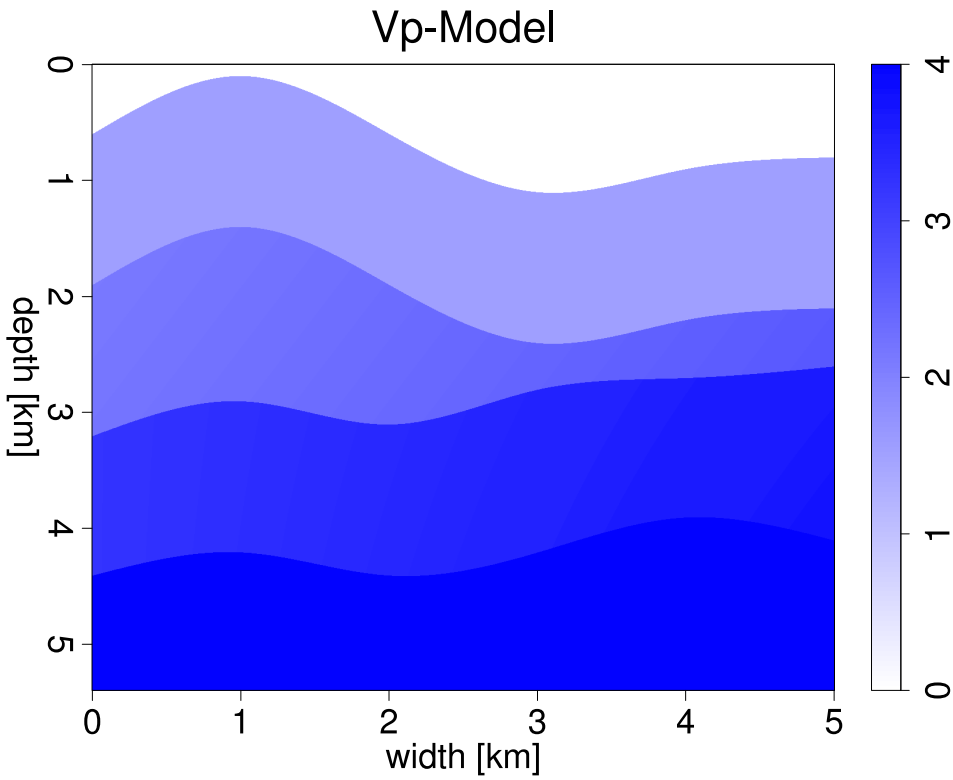


Figure 4.2: A typical geophysical situation with topography.

The rotated staggered grid method can be used to avoid the implementation of computationally expensive free surface boundary conditions as described above. As stated in chapter 3 the method is able to handle the quasi-infinite contrast of the elastic properties of the interface rock/air without applying boundary conditions. Furthermore this is not only the case for a flat free surface. The presence of topography does not require additional specifications in the modeling algorithm. In order to demonstrate this quality I use the geophysical model shown in Figure 4.2. I create a region ($5\text{ km} \times 5\text{ km}$, $\Delta x = \Delta z = 5\text{ m}$) with four layers including topography. The P-wave to S-wave velocity ratio is set to $\sqrt{3}$. Where the P-wave velocity is equal zero I set the density to $0.000001 \frac{\text{g}}{\text{cm}^3}$ (air). In the four layers the density varies from $2 \frac{\text{g}}{\text{cm}^3}$ (top layer) to $2.5 \frac{\text{g}}{\text{cm}^3}$ (bottom layer). The explosion source is placed at the top of the first layer (width=1 km, depth=140 m). The source wavelet is the derivative of a Gaussian with fundamental frequency 9 Hz ($\Delta t = 0.0003125\text{ s}$). The modeling is done with 2nd order time update and with a combination of 2nd and 8th order spatial differentiation operators (compare with Section 4.1). The modeling results are shown in Figure 4.3 and 4.4. Please note the successful modeling of the surface wave (Positions: ca. (1.5 km, 0.5 km) in Figure 4.3 and ca. (2.5 km, 1 km) in Figure 4.4).

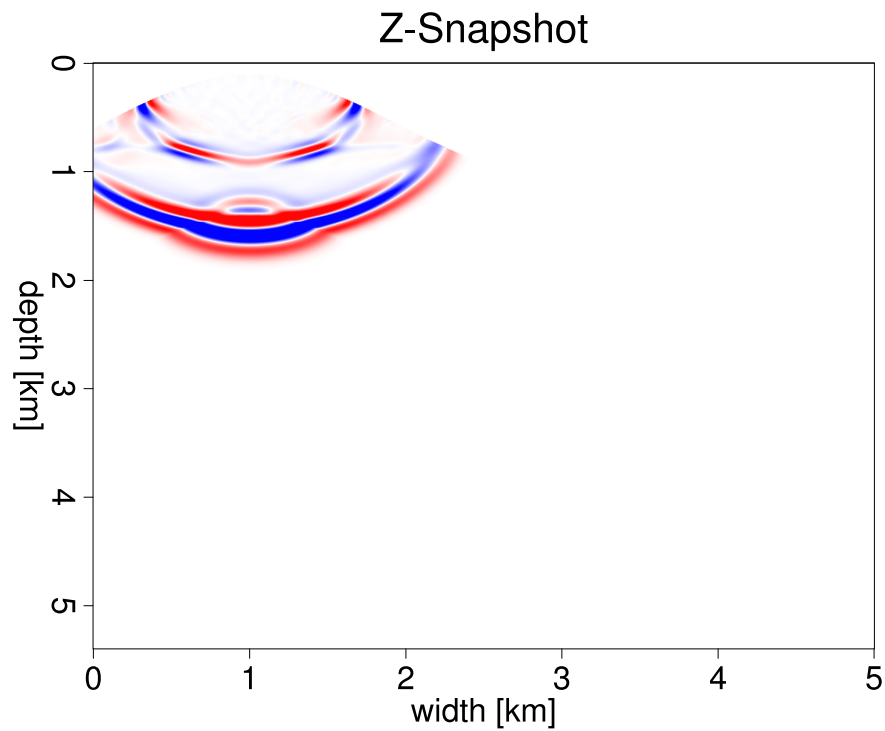


Figure 4.3: X-component-Snapshot at 1.09375s

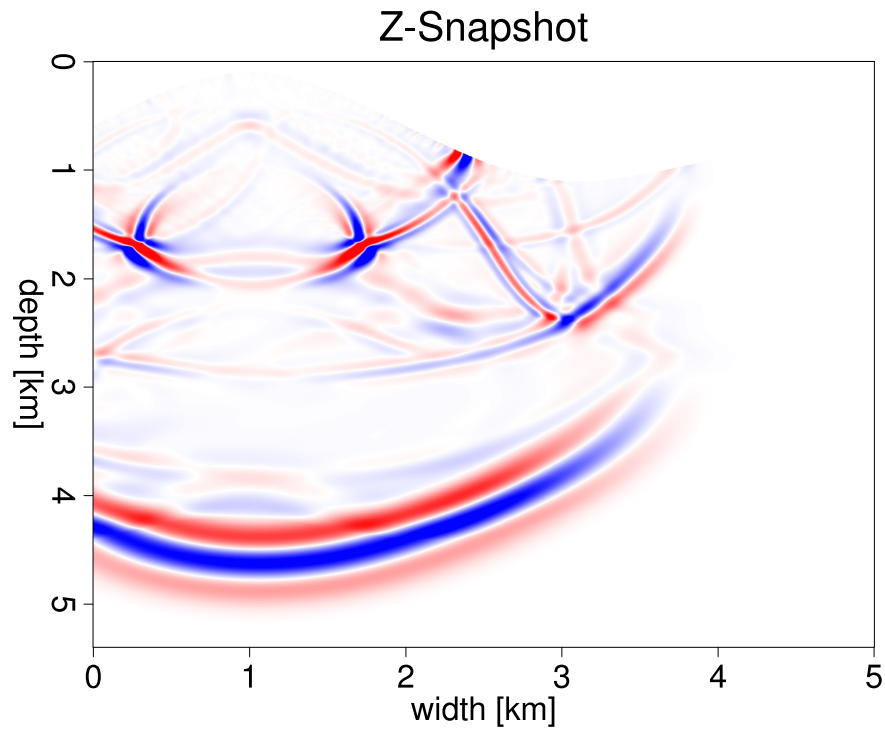


Figure 4.4: Z-component-Snapshot at 2.1875s

4.3 Example 3: 3D aluminum plate - a comparison with laboratory data

The second example is a part of a non-destructive testing experiment [Eberle and Gold, 1998] carried out by a research group in the frame of the Collaborative Research Center 381 (SFB 381) of the German Research Society (DFG). With this example I want to demonstrate that the new rotated staggered grid works very well in 3D with high contrasts of the elastic parameters. Additionally, I show that the synthetic result is in good agreement with the experimental result. In three spatial dimensions, I have modeled the propagation of a short ultrasonic pulse in an aluminum plate with two small artificial cracks (see Figure 4.5).

For the $320\text{mm} \times 120\text{mm} \times 4\text{mm}$ plate, a cubic elementary cell with dimensions $1\text{mm} \times 1\text{mm} \times 1\text{mm}$ was chosen ($\Delta h = 1\text{mm}$). The compressional and shear wave velocity of aluminum is $5769 \frac{\text{m}}{\text{s}}$ and $3077 \frac{\text{m}}{\text{s}}$; the density is $2.7 \frac{\text{g}}{\text{cm}^3}$. To take into account surface effects, the model was extended by a few grid points in all directions. At these grid points and in the two cracks I set the compressional and shear wave velocities to zero and defined a very small value for the density ($0.000001 \frac{\text{g}}{\text{cm}^3}$) which shall approximate vacuum. The density cannot be set to zero as the acceleration is proportional to the inverse of density (see Section 3.2). At the left side of Figure 4.5 I show a slice of the 3D model at the surface of the aluminum plate.

As a source ($f_{fund} = 27000 \frac{1}{\text{s}}$, $f_{max} \approx 65000 \frac{1}{\text{s}}$, $\Delta t = 10^{-7} \text{s}$), I have used a body force perpendicular to the plate, simulating a blow with a hammer. The modeling is done with 2nd order time update and 2nd order space differentiation operators. Neither at the surface, nor inside the cracks, boundary conditions were applied.

Figure 4.5 shows the development of the simulated wave field at the surface of the aluminum plate at different moments of time. In the snapshots on the right-hand side, a situation is shown, where the wave is reflected many times at the upper and lower surface of the plate. The modeling carried on for more than $300\mu\text{s}$ of the real-time propagation without instabilities. Note that the wavelength of the propagation wave is big with respect to the two cracks. Because of that it is not easy to detect visually the cracks in the snapshots.

In Figure 4.6 I compare the result of the simulation with experimental results. Taking into account that the wave form of the source signal was not exactly known from the experiment, I may say that both curves match rather well. The differences at the right hand sides of the curves can be explained by the fact that for experimental reasons the metal plate was not totally fixed. Therefore, it started to move as a whole when hit by the hammer and did not return to its original equilibrium position after the wave had been attenuated. Obviously many other experimental sources of errors can also occur and it should be noted that possible experimental non linear effects and attenuation are not taken into account in the FD program.

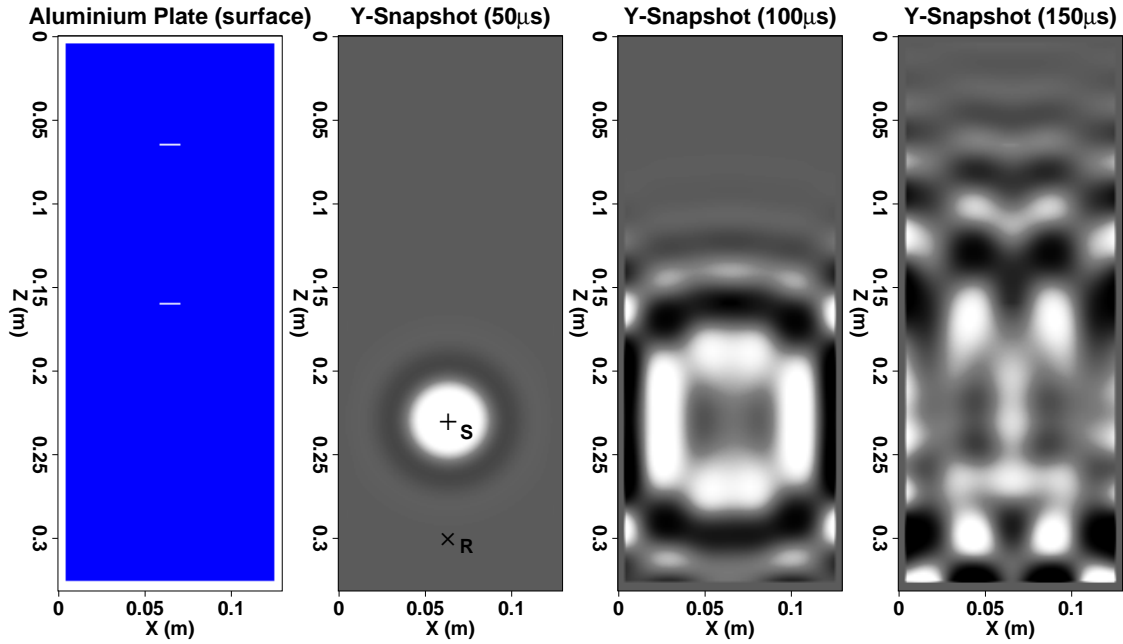


Figure 4.5: A slice of the 3D aluminum plate model and three snapshots of the component of the displacement vector perpendicular to the plate at the surface of the aluminum plate at $50\mu\text{s}$, $100\mu\text{s}$ and $150\mu\text{s}$ after applying the source pulse at the point "S". Black (white) colors denote high positive (negative) amplitudes. Note that on the left-hand Figure the white area around the aluminum plate corresponds to the vacuum part of the model. The thin black line denotes the boundary of the model. The curves in Figure 4.6 were recorded at the point "R".

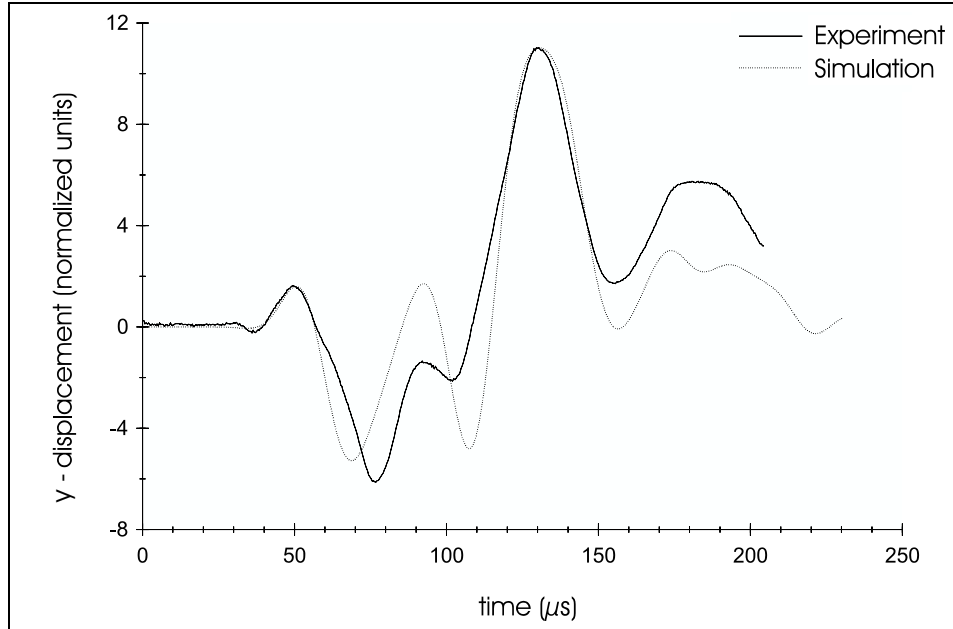


Figure 4.6: Comparison of experimental data to the result of the simulation: Signal recorded by an ultrasonic (point) receiver located at the point "R" in Figure 4.5.

4.4 Example 4: 3D modeling of Lamb waves in thin plates

Lamb waves refer to elastic perturbations propagating in a solid plate (or layer) with free boundaries, for which displacements occur both in the direction of wave propagation and perpendicularly to the plane of the plate. Lamb waves represent one of the types of normal or plate modes in an elastic waveguide, in this case a plate with free boundaries. For this reason, Lamb waves are sometimes simply called normal modes in a plate. But this definition is rather loose, insofar as another type of normal mode can exist in a plate with free boundaries, namely transverse normal modes, wherein the motion is perpendicular to the direction of propagation and parallel to the boundaries of the plate. The transverse normal modes are called antisymmetrical Lamb waves. The deformation of the plate during propagation is illustrated in Figure 4.7.

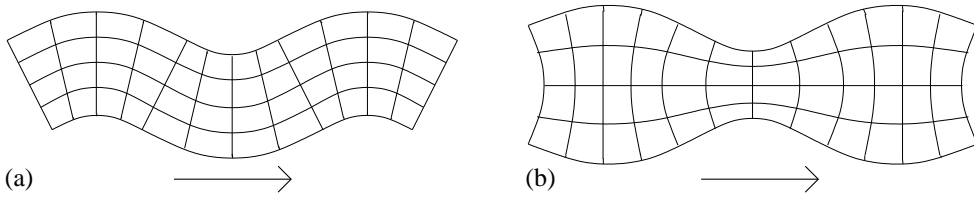


Figure 4.7: The deformation of a thin plate during propagation of antisymmetrical Lamb waves (a) and symmetrical Lamb waves (b) is shown. The arrows mark the direction of wave propagation.

In a thin plate of given thickness and at a given frequency of a source there can exist only a finite number of symmetrical and antisymmetrical Lamb waves. In this example only the first transverse normal mode exists. The physical dispersion of such an antisymmetrical Lamb wave is very strong (see Figure 4.8). Note, if the frequency of a wave tends to zero the velocity of this wave tends to zero, too. For a more detailed description of Lamb waves in thin plates please refer to Viktorov [1967].

In three spatial dimensions, I have modeled the propagation of a short ultrasonic pulse in an aluminum plate with one small artificial crack. For the $305\text{mm} \times 350\text{mm} \times 1.5\text{mm}$ plate, a cubic elementary cell with dimensions $0.15\text{mm} \times 0.15\text{mm} \times 0.15\text{mm}$ was chosen. The compressional and shear wave velocity of aluminum is set to $5769 \frac{\text{m}}{\text{s}}$ and $3077 \frac{\text{m}}{\text{s}}$; the density is $2.7 \frac{\text{g}}{\text{cm}^3}$. To take into account surface effects, the model was extended by a few grid points in all directions. At these grid points and within the crack I set the values of the compressional and shear wave velocities to zero and defined a very small value for the density ($0.000001 \frac{\text{g}}{\text{cm}^3}$) which approximates vacuum conditions. In Figure 4.10 I show a slice of the used 3D model at the surface of the aluminum plate.

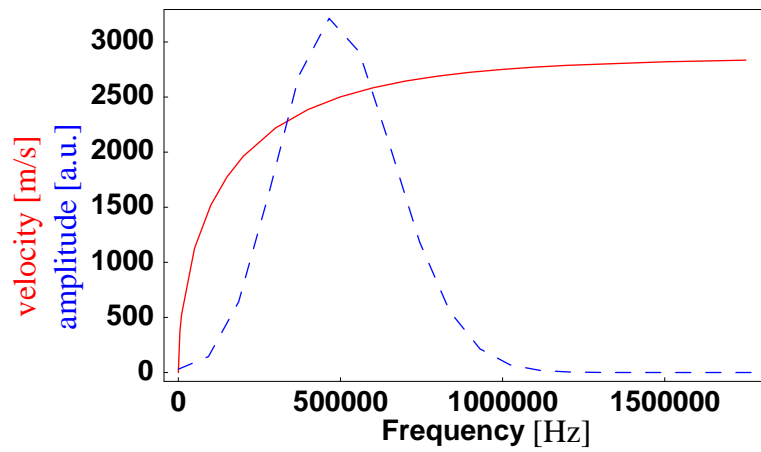


Figure 4.8: The strong physical dispersion of the generated antisymmetric Lamb waves is depicted (solid line). For comparison the amplitude spectrum of the wavelet (source-time function) is plotted (dashed line) in the same diagram.

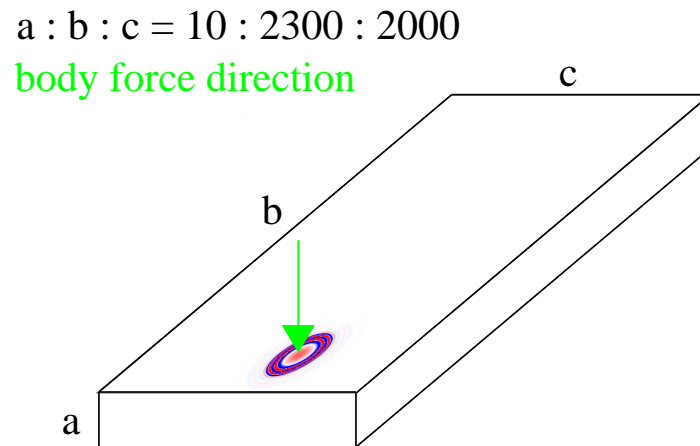


Figure 4.9: Principle of the experiment

As a source ($f_{\text{fund}} = 560000 \frac{1}{s}$, $\Delta t = 2.1 * 10^{-8} s$), I used a body force perpendicular to the plate, simulating a pulse of a transducer. The modeling is done with 2nd order time update and 2nd order space differentiation operators. Neither at the surface, nor inside the cracks, boundary conditions were applied. Figure 4.9 illustrates the experimental setup.

Figures 4.11-4.15 show the development of the simulated wave field at the surface of the aluminum plate at five different timesteps. The antisymmetric Lamb waves generated by the body force perpendicular to the thin plate show the expected strong physically dispersive behavior. The reflections at the boundaries and at the crack can be observed very well. Note, the color scale is normalized in each snapshot to the specific maximum. To obtain such an accurate modeling result with 5000 time steps I use the large scale computer Cray T3E. For the example described above 180 processors need 10 hours calculation time.

A very interesting detail in this modeling is the quasi-static deformation of the aluminum plate at the source location. This effect can be explained with the dispersion relation and the amplitude spectrum of the source wavelet. As mentioned above, the low frequency part has a very slow propagation velocity (it tends to zero, see Figure 4.8). Due to the geometrical spreading effect the amplitudes of the wavefield far from the source location is getting small and therefore the quasi-static part at the source location can be seen very well, as shown in the snapshots in Figures 4.11-4.15.

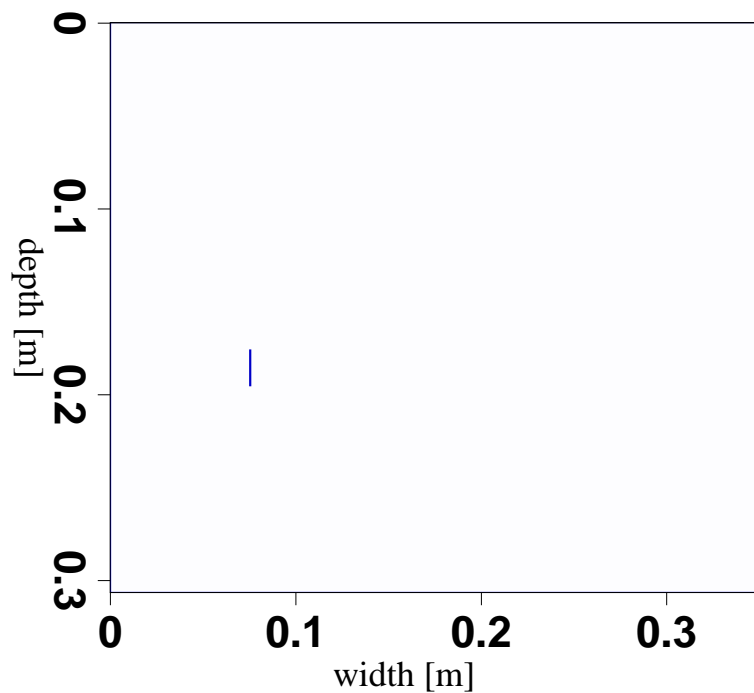


Figure 4.10: A slice of the 3D aluminum plate model is shown. It is easy to detect the crack in the homogeneous plate.

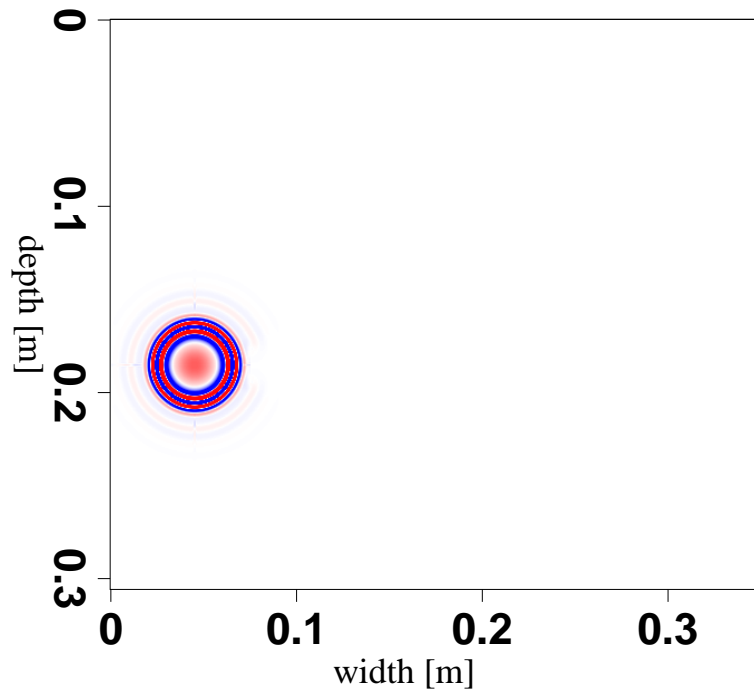


Figure 4.11: Snapshots of the wave field at $10.5\mu s$.

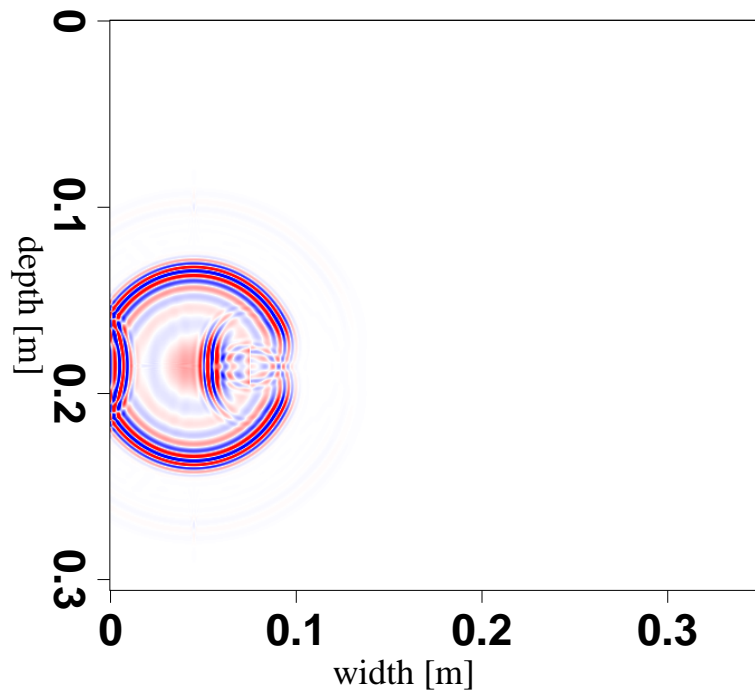


Figure 4.12: Snapshots of the wave field at $21\mu s$.

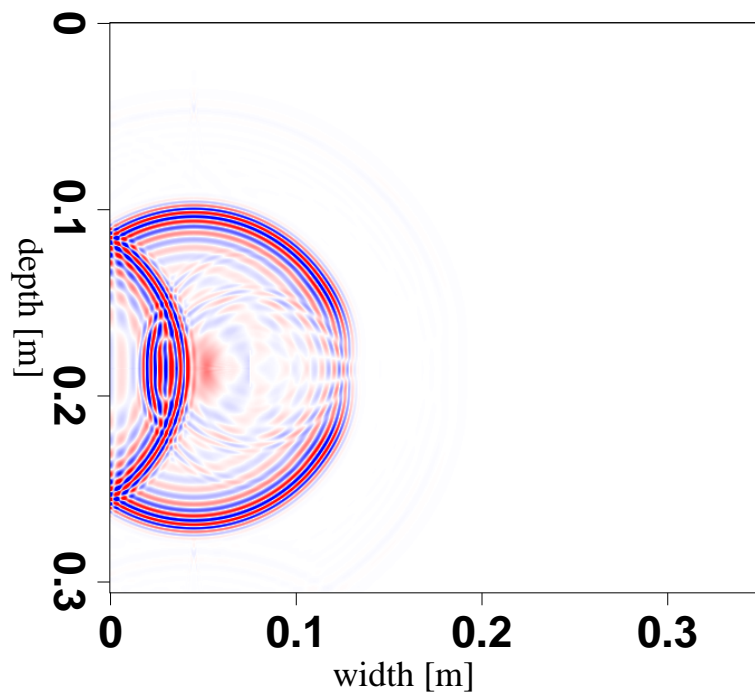


Figure 4.13: Snapshots of the wave field at $31.5\mu s$.

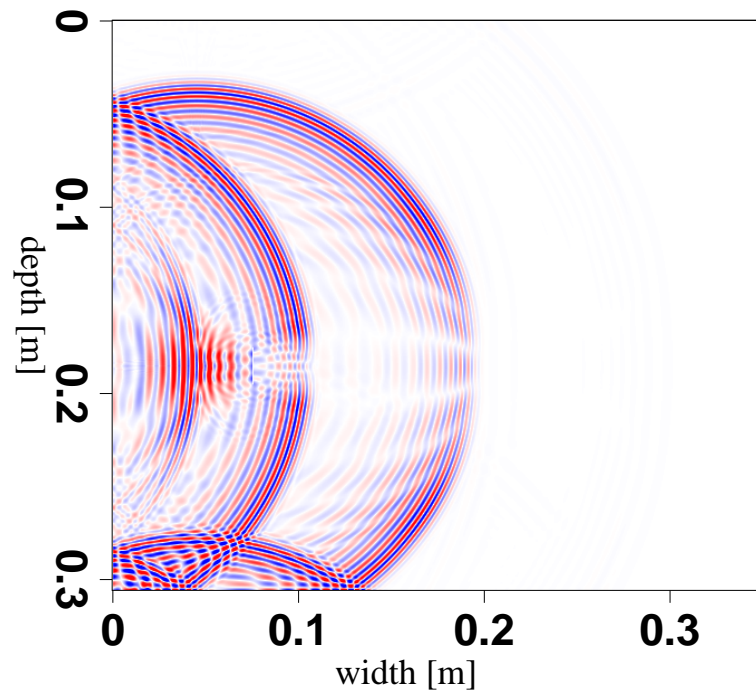


Figure 4.14: Snapshots of the wave field at $52.5 \mu s$.

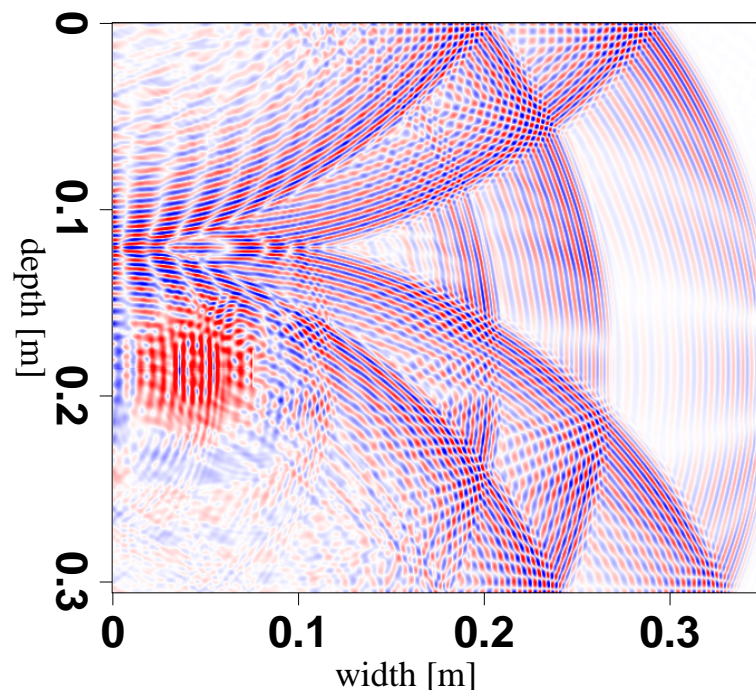


Figure 4.15: Snapshots of the wave field at $105 \mu s$.

4.5 Example 5: Modeling transversely isotropic media

In this example I want to demonstrate that the rotated staggered finite-difference grid can be applied for wave propagation modeling in anisotropic media. Hence, I build a 3D-model with $125 \times 125 \times 125$ grid points including 2 grid points of vacuum at each side ($\Delta d = 0.001m$).

The elastic parameters of the transversal isotropic homogeneous block are: $c_{11} = 7.500 \times 10^{10} \frac{kg}{s^2 m}$, $c_{33} = 4.800 \times 10^{10} \frac{kg}{s^2 m}$, $c_{44} = 2.700 \times 10^{10} \frac{kg}{s^2 m}$, $c_{66} = 3.675 \times 10^{10} \frac{kg}{s^2 m}$, $c_{13} = 1.875 \times 10^{10} \frac{kg}{s^2 m}$, $\rho = 3000 \frac{kg}{m^3}$. The body force source in X-direction is placed at position (42,42,42). I use the first derivative of a Gaussian with $d_t = 3.0 \times 10^{-8}s$ and $f_{fund} = 210kHz$. Therefore, a S-wave polarized in the X-direction propagates in the Z-Y-plane. Figure 4.16 shows some snapshots of the wave field in the Z-Y-plane (X=42) at different timesteps. The different propagation velocities in the Z- and the Y- direction, determined by the chosen elastic constants, can be clearly observed.

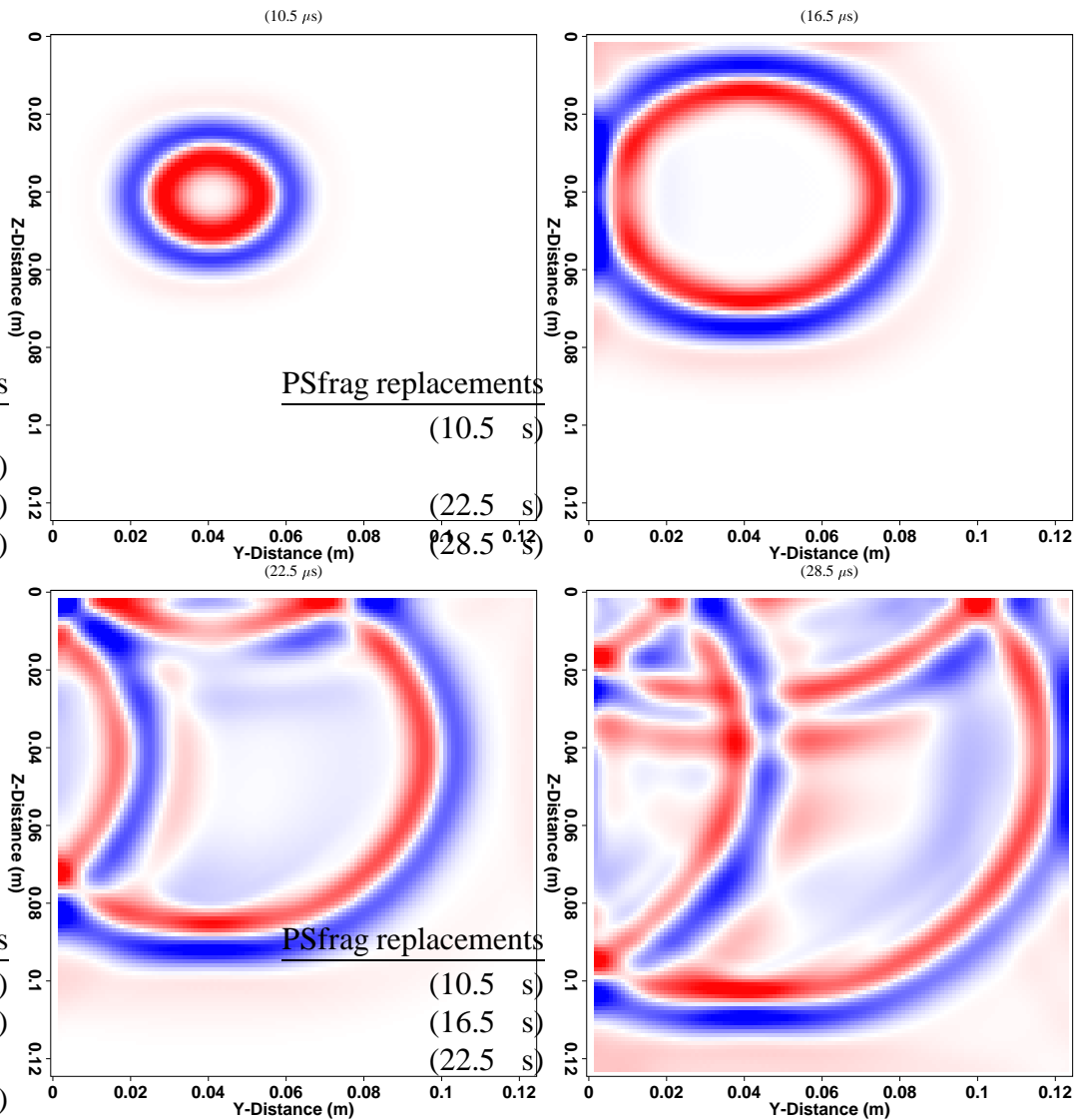


Figure 4.16: Modeling of wave propagation in transversely isotropic medium. The details are in section 4.5

4.6 Example 6: Modeling elastic waves in concrete

Concrete as a strongly heterogeneous and high-packed composite material represents a very important but also very difficult object for ultrasonic Non-Destructive-Testing (NDT) methods. Due to the high scatterer density, ultrasonic wave propagation in this material consists of a complex mixture of multiple scattering, mode conversion and diffusive energy transport. In order to obtain a better understanding of the effect of aggregates and porosity on elastic wave propagation in concrete and to optimize inverse reconstruction techniques, e.g. SAFT [Burr et al., 1997], it is useful to model the wave propagation and scattering process explicitly in the time domain.

To demonstrate that the rotated grid can model elastic waves in concrete the model shown in Figure 4.17 was created. The model (grid spacing $\Delta h = 0.0002m$) consist of a $10cm \times 10cm$ homogeneous area in which the compressional and shear wave velocity is set to $3950\frac{m}{s}$ and $2244\frac{m}{s}$; the density is $2.172\frac{g}{cm^3}$. Around this area and within the crack and in the air inclusions I set the the velocities to zero and the density to $0.000001\frac{g}{cm^3}$ which approximates vacuum conditions. The ellipses which represent gravel ($vp = 4030\frac{m}{s}$, $vs = 2327\frac{m}{s}$, $\rho = 2.59\frac{g}{cm^3}$) of different sizes make up 50% of the overall area. A body force line source ($f_{fund} = 8 \cdot 10^{5}\frac{1}{s}$, $f_{max} \approx 2.5 \cdot 10^{6}\frac{1}{s}$, $\Delta t = 7 \cdot 10^{-9}s$) in z-direction is placed at the interface rock/vacuum. The modeling is done with 2nd order time update and with a combination of 2nd and 8th order spatial differentiation operators [Gold et al., 1997].

A study of Vieth et al. [1999] makes use of a synthetic data set recorded at this numerical experiment. A goal of this study is to image the crack in the heterogeneous embedding. They make use of the well known Kirchhoff migration (see e.g. [Langenberg et al., 1993]) and compute afterwards the envelope which improves the image, i.e. it is easier to localize the crack. The result is shown in Figure 4.18.

A more detailed study of crack imaging in concrete based on synthetic data produced with the help of the rotated staggered grid using the Common Reflection Surface Stack [Müller, 1999] can be found in Hubral [1999].

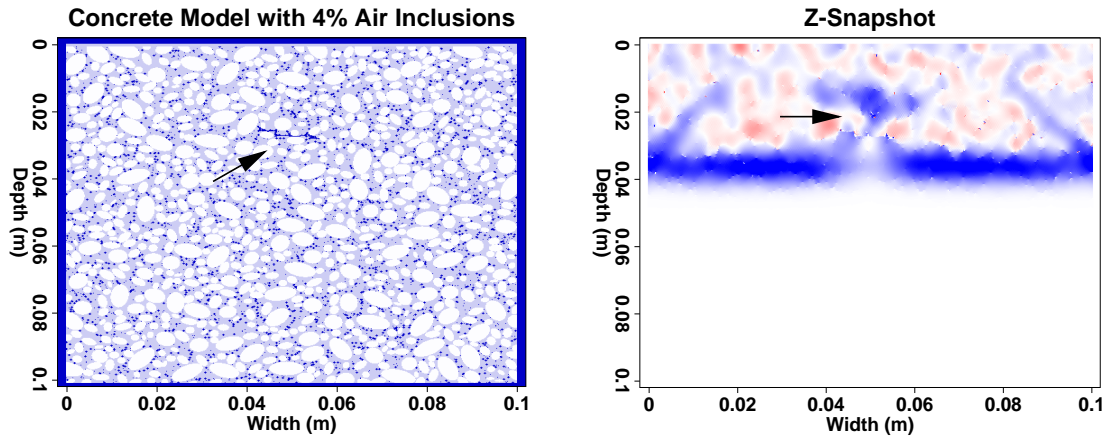


Figure 4.17: On the **left** side a heterogeneous concrete model with a defect, i.e. the crack, is shown. The ellipses represent gravel within cement. The concrete model is bounded by a thin layer of air. The **right** figure shows a Z-snapshot after a part of a plane wave has been reflected by the crack.

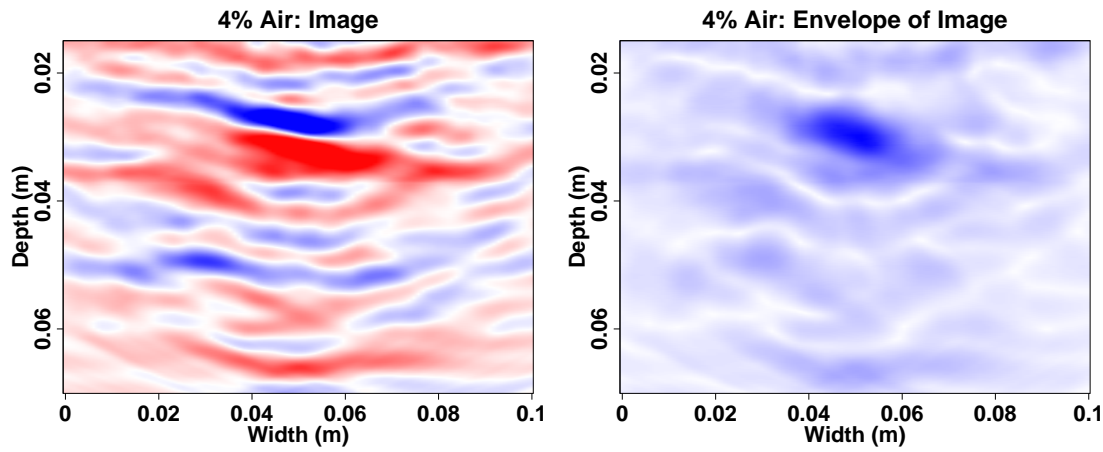


Figure 4.18: The migration of the plane-wave response is on the left. On the right is the envelope of the migrated section

Chapter 5

Effective velocities in fractured media

This chapter shows the application of the rotated staggered grid technique to obtain effective velocities in fractured media. After a comprehensive discussion of theories the numerical results are shown.

This chapter is based on: [Saenger and Shapiro, 1999a,b, 2000a,b,c; Saenger et al., 2000b]

5.1 Introduction

The problem of effective elastic properties of fractured solids is of considerable interest for geophysics, for material science, and for solid mechanics. Particularly, it is important for constitutive modeling of brittle micro cracking materials. For obvious reasons of practicality, the problem of a three-dimensional medium permeated by circular or elliptical planar cracks has received more attention in the literature. In this thesis I consider the problem of a fractured medium in two dimensions. This may seem to be a significant oversimplification. However, I think that with this work some broad generalizations can be elucidated that will help solving problems with more complicated geometries.

Strong scattering caused by many dry cracks can be treated only by numerical techniques because an analytical solution of the wave equation is not available. So-called boundary integral methods are well suited to handle such discrete scatterers in a homogeneous embedding. They allow the study of SV-waves [Davis and Knopoff, 1995; Murai et al., 1995], SH-waves [Dahm and Becker, 1998] and P-waves [Kelner et al., 1999] in multiple fractured media, but they are restricted to non-intersecting cracks.

Since the FD approach is based on the wave equation without physical approximations, the method accounts not only for direct waves, primary reflected waves, and multiply reflected waves, but also for surface waves, head waves, converted reflected waves, and waves observed in ray-theoretical shadow zones [Kelly et al., 1976]. Additionally, it automatically accounts for the proper relative amplitudes. Consequently, FD solutions of the wave equa-

tion are widely used to study scattering of waves by heterogeneities (e.g. [Frankel and Clayton, 1986; Kneib and Kerner, 1993; Andrews and Ben-Zion, 1997; Kusnandi et al., 2000]). In the present numerical study, however, I apply the rotated staggered grid [Saenger et al., 2000a] for the modeling of elastic wave propagation in arbitrary heterogeneous media.

In this chapter I present a numerical study of effective velocities of three types of fractured 2D-media. I model the propagation of a plane wave through a well defined fractured region. The numerical setup is described in section 5.3.1 . I use randomly distributed and randomly oriented rectilinear dry thin cracks in the first two kinds of fractured media. For the first type of media I examine only non-intersecting cracks. The numerical results for P-, SV- and SH-waves (see section 5.3.2) are compared comprehensively with several theories (see section 5.2.3) that predict the effective velocities for such a case. Additionally, I compare my results with the numerical results of Davis and Knopoff [1995], Murai et al. [1995] and Dahm and Becker [1998]. In the second type of fractured media I consider intersecting cracks. For this case the theories for non-intersecting cracks and boundary integral methods are beyond their range of validity. However, I have found that the theory of Mukerji et al. [1995], including a so called critical-porosity concept, can be applied to take into account the fact of intersecting cracks. Combining the concept of critical porosity (i.e., critical crack density) with the so-called modified self-consistent theory I propose in section 5.2.4, a new analytical formulation which is able to handle the case of intersecting cracks. The predictions of this new heuristic formalism are in excellent agreement with our numerical results shown in section 5.3.3 . In the third type of media I consider parallel cracks. I show that the theory for non-interacting cracks is also in this case restricted to dilute crack densities.

5.2 Theory

5.2.1 Formulas for transversal isotropic media

In the first two kinds of 2D fractured media the models are filled at random with randomly oriented rectilinear dry thin cracks (see section 5.2.3 and 5.2.4). Therefore I consider 2D isotropic effective media. But from a theoretical point of view this fractured 2D models also represent a 3D transversely isotropic fractured situation with symmetry axis perpendicular to the 2D-plane. Hence, I use the same notation as Thomsen [1986]. The elastic moduli and the velocities in those media are related with well known formulas (compare with Eq. 2.22-2.24 in section 2.5):

$$\rho_g v_{SV}^2(90^\circ) = c_{44}, \quad (5.1)$$

$$\rho_g v_{SH}^2(90^\circ) = c_{66}, \quad (5.2)$$

$$\rho_g v_P^2(90^\circ) = c_{11}, \quad (5.3)$$

where c_{11} , c_{44} and c_{66} are elements of the stiffness tensor, ρ_g is the gravitational density and $v_{SV}(90^\circ)$, $v_{SH}(90^\circ)$ and $v_P(90^\circ)$ are the phase velocities of SV-, SH- and P- waves perpendicular to the symmetry axis of the transversely isotropic medium.

5.2.2 Formulas for orthorhombic media

For the case of parallel cracks (see section 5.2.5) I consider orthorhombic media. With Eq. 2.26-2.28 in section 2.5 one can derive the following formulas, which are relating seismic velocities with elements of the stiffness tensor for orthorhombic media:

$$\rho_g v_{SV}^2(90^\circ) = c_{55}, \quad (5.4)$$

$$\rho_g v_{SH}^2(90^\circ) = c_{66}, \quad (5.5)$$

$$\rho_g v_P^2(90^\circ) = c_{11}, \quad (5.6)$$

where c_{11} , c_{55} and c_{66} are elements of the stiffness tensor, ρ_g is the gravitational density and $v_{SV}(90^\circ)$, $v_{SH}(90^\circ)$ and $v_P(90^\circ)$ are the phase velocities of SV-, SH- and P- waves in the XZ plane of the orthorhombic medium.

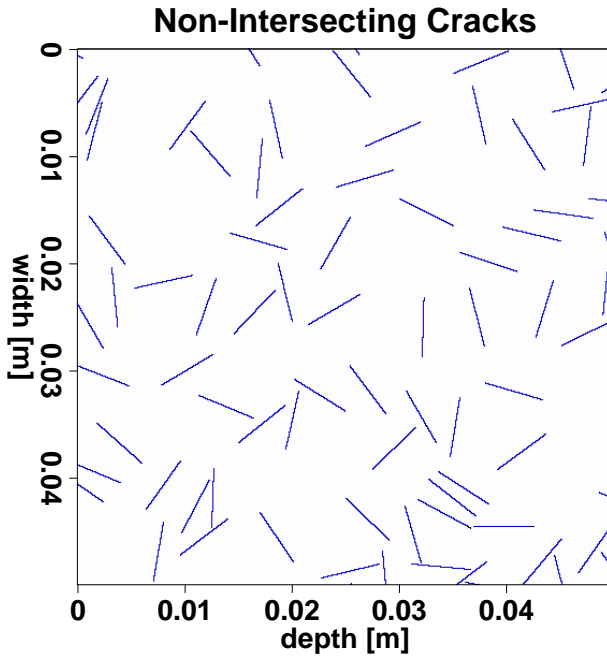


Figure 5.1: Randomly distributed and randomly oriented rectilinear non-intersecting thin dry cracks in homogeneous 2D-media. A part of Model 7.1 is shown (see Table 5.1).

5.2.3 Non-intersecting Cracks

In this section I consider randomly distributed rectilinear non-intersecting thin dry cracks in 2D-media (see Figure 5.1). Papers of Kachanov [1992] and of Davis and Knopoff [1995] provide sound descriptions of theoretical approaches in this case. Both papers discuss three different theories for 2D-media that predict an effective velocity for fractured models. Namely, these are the “theory for non-interacting cracks”(NIC), the “self-consistent theory” (SC) and the “modified (or differential) self-consistent theory” (MSC). They can be used to predict effective wave velocities in the long wavelength limit. In order to later compare my numerical results with different theoretical predictions I summarize here the ideas and results for these theories. For the definition of the crack density parameter ρ [Kachanov, 1992], I use:

$$\rho = \frac{1}{A} \sum_{k=1}^n l_k^2 , \quad (5.7)$$

where $2l_k$ is the length of rectilinear cracks, n is the number of cracks, and A is the representative area.

First, I concentrate on one type of shear waves: SH(90°) -waves. The theory for non-interacting cracks is derived for the case of a dilute crack density. It assumes that the energy per unit crack length, needed for inserting a single anti plane crack, is just added n times to the energy of the unfractured medium. With this assumption one can calculate the effective shear modulus $\langle \mu_{NIC} \rangle$ ($\hat{=} \langle c_{66} \rangle$) [Davis and Knopoff, 1995]:

$$\langle \mu_{NIC} \rangle = \mu_0 \frac{1}{1 + \pi(\rho/2)}, \quad (5.8)$$

where μ_0 is the shear modulus of the unfractured isotropic medium and ρ is the crack density.

In the simplest form of self-consistent calculations, to determine the properties at higher orders it is argued that an individual crack is introduced into an already cracked medium and hence should be subjected to the stress field in the flawed system (i.e. in the effective medium) and not to that in the unflawed system [Budiansky and O'Connell, 1976; O'Connell and Budiansky, 1974, 1976]. This yields the following prediction for the effective shear modulus $\langle \mu_{SC} \rangle$:

$$\langle \mu_{SC} \rangle = \mu_0 [1 - \pi(\rho/2)]. \quad (5.9)$$

However, Chatterjee et al. [1978], Hudson [1980], and Hudson and Knopoff [1989] showed that although the interaction between cracks is considered in the self-consistent model, the dipole-dipole interactions are neglected and may have a practical importance at high crack densities.

Two other studies [Bruner, 1976; Henyey and Pumphrey, 1982] argue that the change in energy should be calculated sequentially by introducing new cracks in sequentially altered effective media. This argument leads to the shear modulus as the solution to a simple differential equation. The result of such a consideration, called the modified (or differential) self-consistent theory, is the following exponential formula for the effective shear modulus $\langle \mu_{MSC} \rangle$:

$$\langle \mu_{MSC} \rangle = \mu_0 e^{-\pi(\rho/2)}. \quad (5.10)$$

To complete my overview I give briefly the formulas of effective moduli of the three theories for P(90°)- and SV(90°) -waves [Kachanov, 1992]:

$$\langle c_{11} \rangle = \frac{\langle E \rangle (1 - \langle \nu \rangle)}{(1 + \langle \nu \rangle)(1 - 2\langle \nu \rangle)} \quad (5.11)$$

$$\langle c_{44} \rangle = \frac{\langle E \rangle}{2(1 + \langle \nu \rangle)} \quad (5.12)$$

- Theory for non-interacting cracks:

$$\langle E_{NIC} \rangle = E_0 \frac{1}{1 + \pi\rho}, \quad (5.13)$$

$$\langle \nu_{NIC} \rangle = \nu_0 \frac{1}{1 + \pi\rho}. \quad (5.14)$$

- Self-consistent theory:

$$\langle E_{SC} \rangle = E_0(1 - \pi\rho), \quad (5.15)$$

$$\langle \nu_{SC} \rangle = \nu_0(1 - \pi\rho). \quad (5.16)$$

- Modified (differential) self-consistent theory:

$$\langle E_{MSC} \rangle = E_0 e^{-\pi\rho}, \quad (5.17)$$

$$\langle \nu_{MSC} \rangle = \nu_0 e^{-\pi\rho}. \quad (5.18)$$

In this equations E_0 denotes Young's modulus and ν_0 Poisson's ratio of the unfractured isotropic medium. Note, that in first order (i.e., to the terms $O(\pi\rho)$) all three theories predict the same effective modulus.

Figure 5.5 illustrates the theories for non-intersecting cracks (for $\nu_0 = 0.25$). The three dashed lines are due to the prediction by the theory for non-interacting cracks. The three dashed-dotted lines are the prediction by the self-consistent theory and the three solid lines are due to the prediction by the modified (or differential) self-consistent theory. The top curves result from SH(90°) -waves. The other shear wave results (SV(90°) -waves) are depicted in the middle. The bottom curves result from compressional (P(90°)-) waves.

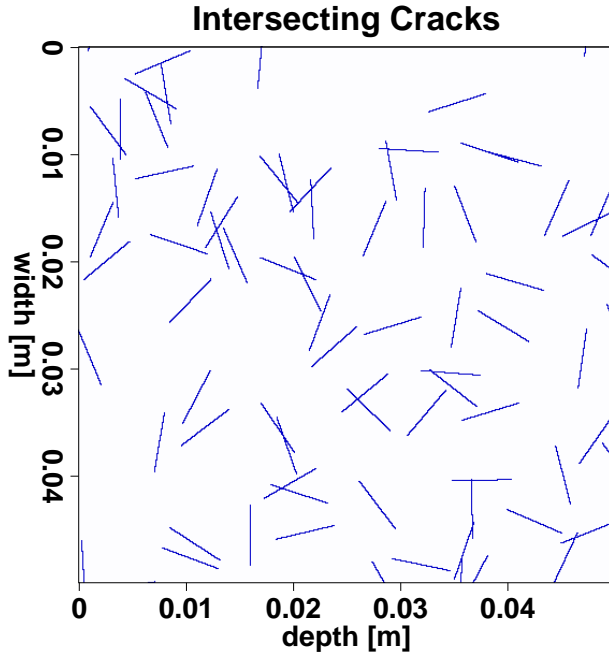


Figure 5.2: Randomly distributed and randomly oriented rectilinear intersecting thin dry cracks in homogeneous 2D-media. A part of Model 10x.1 is shown (see Table 5.1).

5.2.4 Intersecting Cracks

Let us now consider randomly distributed and randomly oriented rectilinear intersecting thin dry cracks in 2D-media (see Figure 5.2). The theories described in section 5.2.3 are not applicable in this case, because they are derived in particular for non-intersecting cracks. For example, for a crack density of $\rho = 1.43$ the effective modulus predicted by the modified self-consistent theory for SH(90°)-waves (Eq. 5.10) is $\langle \mu \rangle = 0.10 \mu_0$. But at this crack density in the case of intersecting cracks I observe a modulus of $\langle \mu \rangle = 0$ because there is no path for the wave through the skeleton of fractured medium. In the case of intersecting cracks the medium clearly demonstrates a kind of percolation behavior. It is a monolith for small ρ . However, it falls apart for large ρ . Therefore, to predict the effective velocities it is necessary to use another approach taking into account such a critical behavior.

In the case of porous media Mukerji et al. [1995] proposed to use the differential effective medium (DEM) theory [Norris, 1985; Zimmermann, 1991] modified by including the concept of the critical porosity [Nur, 1992]. Note, in this formalism the effective velocities are predicted in terms of porosity ϕ rather than in terms of crack density ρ .

The first step to use this modified DEM-theory for fractured media is to determine the critical porosity (or the critical crack density). At the percolation porosity, the material is a loose packing of grains barely touching each other. This value can be derived with the help of percolation theory (see e.g. [Sahimi, 1995]). The special case of percolation in my

models is discussed and calculated by Robinson [1983, 1984]. The result corresponding to my models (intersecting rectilinear thin cracks in 2D media with constant length) is a critical crack density of $\rho_c = 1.43$ (or a critical porosity of $\phi_c = 0.13$). For $\rho > \rho_c$ only finite-size clusters exist where an elastic wave can propagate. This is illustrated in Fig.1 of Robinson [1983].

The second step is to calculate the effective elastic parameters at the critical porosity. The moduli at the percolation point are equal to the Reuss (harmonic) average of the constituent moduli, because in general case of filled pores or cracks the medium tends to a suspension. In my case of dry cracks I obtain a value of zero for all moduli at the critical density:

$$\mu_c = \lim_{\mu_2 \rightarrow 0 \text{ Pa}} \frac{2}{1/\mu_1 + 1/\mu_2} = 0 \text{ Pa} \quad (5.19)$$

and

$$K_c = \lim_{K_2 \rightarrow 0 \text{ Pa}} \frac{2}{1/K_1 + 1/K_2} = 0 \text{ Pa.} \quad (5.20)$$

The third step is to calculate the effective moduli in dependence of the porosity ($\langle K \rangle = K(y)$ and $\langle \mu \rangle = \mu(y)$). For arbitrary distributed cracks in 3D I have to solve two coupled differential equations [Berryman, 1992] with critical porosity initial conditions that can be found in [Mukerji et al., 1995]:

$$(1 - y) \frac{d}{dy} [K(y)] = [K_2 - K(y)] P(y), \quad (5.21)$$

$$(1 - y) \frac{d}{dy} [\mu(y)] = [\mu_2 - \mu(y)] Q(y). \quad (5.22)$$

with initial conditions $K(0) = K_1$ and $\mu(0) = \mu_1$. The main idea to involve the critical porosity in this equations is to set: $K_2 = K_c$ and $\mu_2 = \mu_c$. With this definition, y denotes the concentration of the critical phase in the material and now the total porosity is $\phi = y\phi_c$.

Using this approach I observed, that the predicted effective velocity for S-waves for needle-like inclusions [Berryman, 1980; Wu, 1966; Eshelby, 1957] is in a good agreement with numerical results for SH(90°)-waves in 2D-media with intersecting cracks (see [Saenger and Shapiro, 2000a] and Figure 5.7).

For the case of needle like dry cracks equations 5.21 and 5.22 are reduced to:

$$(1 - y) \frac{d}{dy} [K(y)] = -K(y) P(y), \quad (5.23)$$

$$(1 - y) \frac{d}{dy} [\mu(y)] = -\mu(y) Q(y). \quad (5.24)$$

with:

$$P(y) = 1 + \frac{K(y)}{\mu(y)}, \quad (5.25)$$

$$Q(y) = \frac{1}{5} \left[6 + \frac{2\mu(y)}{\gamma(y)} \right], \quad (5.26)$$

and

$$\gamma(y) = \frac{\mu(y) [3 K(y) + \mu(y)]}{3 K(y) + 7 \mu(y)}. \quad (5.27)$$

However, my 2D fractured models with rectilinear cracks represent 3D transversely isotropic media with symmetry axis perpendicular to the 2D-plane. The modified DEM-theory is (so far) only derived for 3D isotropic fractured media. 3D Transversely isotropic fractured media are discussed for dilute crack densities for example in [Nur, 1971]. The difficulty to incorporate percolation behavior in a DEM-theory is the requirement of a solution for high crack densities. Some general ideas in this direction can be found in [Cheng, 1993].

From the other hand there are a lot in common in physical concepts of the DEM theory and the MSC theory. The most important here is the principle of sequential introduction of new cracks leading in simple situations to exponential formulas for effective moduli. Taking this into account I suggest here a new heuristic critical crack density (CCD) formulation for 2D (i.e. 3D transversely isotropic) fracturing configurations. I introduce into results of the MSC-theory (described in section 5.2.3) an additional factor to include the physical behavior at the critical crack density. I propose the following formulae (compare with Eq. (5.10), (5.17) and (5.18)):

$$\langle \mu_{CCD} \rangle = \mu_0 e^{-\pi(\rho/2) \left(\frac{\rho_c}{\rho_c - \rho} \right)^n}, \quad (5.28)$$

$$\langle E_{CCD} \rangle = E_0 e^{-\pi\rho \left(\frac{\rho_c}{\rho_c - \rho} \right)^n}, \quad (5.29)$$

$$\langle \nu_{CCD} \rangle = \nu_0 e^{-\pi\rho \left(\frac{\rho_c}{\rho_c - \rho} \right)^n}, \quad (5.30)$$

where ρ_c denotes the critical crack density.

This heuristic formalism fulfills the following important conditions:

- For the critical crack density the elastic moduli are zero. For example:

$$\lim_{\rho \rightarrow \rho_c} \langle \mu_{CCD} \rangle = 0. \quad (5.31)$$

- For an infinite critical crack density the theory gives the same predictions as the MSC-theory. The necessity of this limit follows from the physically evident fact that an infinite critical crack density for randomly distributed and oriented rectilinear thin cracks implies non-intersecting cracks. For example:

$$\lim_{\rho_c \rightarrow \infty} \langle \mu_{CCD} \rangle = \langle \mu_{MSC} \rangle. \quad (5.32)$$

- For dilute crack densities the CCD-theory gives (in first order) the same predictions as the MSC-theory. For example:

$$\frac{\partial}{\partial \rho} \langle \mu_{CCD} \rangle (0) = \frac{\partial}{\partial \rho} \langle \mu \rangle (0), \quad (5.33)$$

$$\langle \mu_{CCD} \rangle (0) = \langle \mu_{MSC} \rangle (0) = \langle \mu_0 \rangle. \quad (5.34)$$

The effective velocities of SH(90°), SV(90°), and P(90°)- waves predicted by this new CCD- formulations are plotted in Figure 5.8 with solid lines ($\nu_0 = 0.25$, $\rho_c = 1.43$, $n = 0.5$).

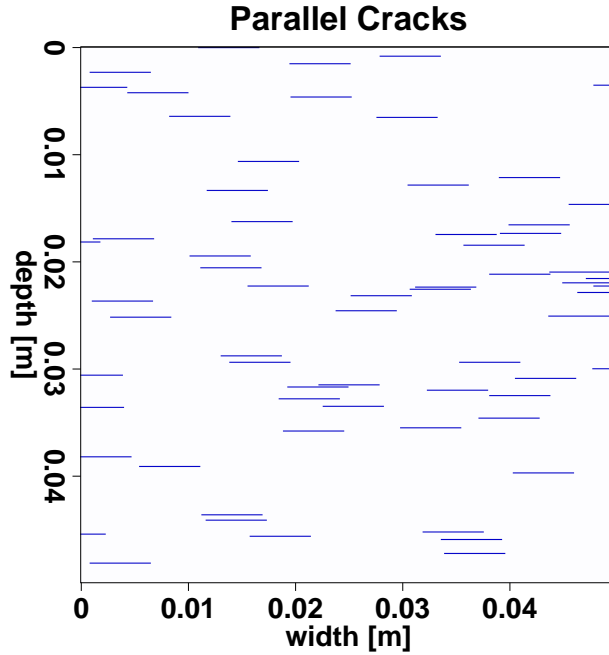


Figure 5.3: Randomly distributed rectilinear parallel non-intersecting thin dry cracks in homogeneous 2D-media. A part of Model 18p is shown (see Table 5.1).

5.2.5 Parallel Cracks

This section considers randomly distributed rectilinear parallel non-intersecting thin dry cracks in 2D-media (see Figure 5.3). The paper of Kachanov [1992] discusses a theoretical description of effective velocities in such a case. For parallel cracks only the solution for non-interacting cracks is given. To obtain c_{11} from E_1 one can use Eq. 5.11 because under uniaxial loading conditions in one of the principal symmetry directions, the presence of cracks does not cause any additional Poisson effect.

$$E_1 = E_0 \frac{1}{1 + 2\pi\rho} \quad (5.35)$$

$$\nu_1 = \nu_0 \frac{1}{1 + 2\pi\rho} \quad (5.36)$$

$$\langle c_{44} \rangle = \langle G_{12} \rangle = G_0 \frac{1}{1 + 2\pi(G_0/E_0)\rho} \quad (5.37)$$

The effective velocities of SV(90°) and P(90°)- waves predicted by this non-interacting theory for parallel cracks are plotted in Figure 5.9 using dashed lines ($\nu_0 = 0.25$).

5.3 Numerical Experiments

5.3.1 Experimental Setup

As described above, the rotated staggered FD scheme is a powerful tool for testing theories about fractured media. This formalisms discussed in section 5.2 predict the effective elastic moduli of multiply fractured media as a function of crack density ρ or porosity ϕ . In order to test this formalisms I design some numerical elastic models which include a region with a well known crack density and porosity. The cracked region was filled at random with randomly oriented cracks. In Figure 5.4 (left hand side) we can see a typical model with non-intersecting cracks. This model contains 1000×1910 grid points with an interval of 0.0001m . In the homogeneous region I set $v_p = 5100 \frac{\text{m}}{\text{s}}$, $v_s = 2944 \frac{\text{m}}{\text{s}}$ and $\rho_g = 2700 \frac{\text{kg}}{\text{m}^3}$. Table 5.1 is the summary of relevant parameters of all the models I use for my experiments. For the dry cracks I set $v_p = 0 \frac{\text{m}}{\text{s}}$, $v_s = 0 \frac{\text{m}}{\text{s}}$ and $\rho_g = 0.0001 \frac{\text{kg}}{\text{m}^3}$ which approximate vacuum. Therefore each additional crack increases the porosity.

It is important to note that I perform my modeling experiments with periodic boundary conditions in the horizontal direction. For this reason my elastic models are generated also with this periodicity. Hence, it is possible for a single crack to start at the right side of the model and to end at its left side.

To obtain effective velocities in different models I apply a body force line source at the top of the model. The plane wave generated in this way propagates through the fractured medium (see Figure 5.4). With two horizontal lines of 1000 geophones at the top (depth=0.01m) and at the bottom (depth=0.152m), it is possible to measure the time-delay of the mean peak amplitude of the plane wave caused by the inhomogeneous region. With the time-delay one can calculate the effective velocity. Additionally, the attenuation of the plane wave can be studied. Note that the time-delay and the attenuation do not significantly depend on the particular realization of my model for a given fixed crack density. This will be demonstrated in the following with error bars.

The direction of the body force and the source wavelet (i.e. source time function) can vary to generate two types of shear (SH- and SV-) waves and one compressional (P-) wave. The source wavelet in my experiments is always the first derivative of a Gaussian with different dominant frequencies and with a time increment of $\Delta t = 5 * 10^{-9}\text{s}$. In Table 5.2 one can find details of the wavelets.

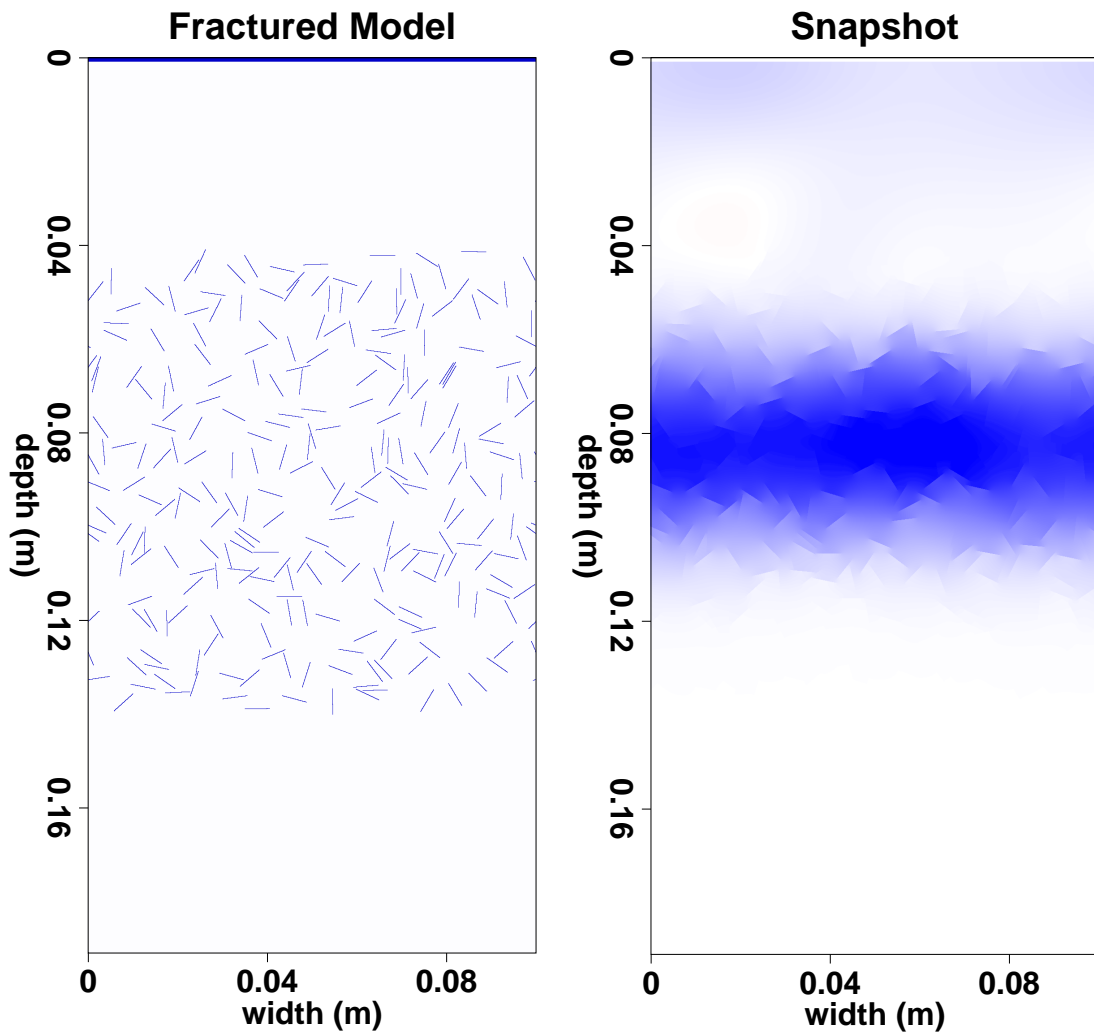


Figure 5.4: The left hand side shows a typical fractured model (No. 7.1 of Table 5.1) used for the numerical experiments. I introduce a cracked region in a homogeneous material. At the top I place a small strip of vacuum. This is advantageous for applying a body force line source with the rotated staggered grid. The right side is a snapshot of a plane wave propagating through the cracked region.

No.	crack density ρ	length of cracks [0.0001m] \\ aspect ratio of cracks	number of cracks	porosity ϕ of the crack region	number of model realizations
1.1-1.4	0.200	7 \ 0.14	15280	0.1407	4
2.1-2.7	0.200	14 \ 0.077	3881	0.0708	7
3	0.200	28 \ 0.04	996	0.0358	1
4	0.025	56 \ 0.021	31	0.0022	1
5	0.050	56 \ 0.021	63	0.0046	1
6.1-6.5	0.100	56 \ 0.021	126	0.0091	6
7.1-7.11	0.200	56 \ 0.021	252	0.0181	11
8x	0.050	56 \ 0.021	63	0.0045	1
9x	0.100	56 \ 0.021	126	0.0091	1
10x.1-10x.6	0.200	56 \ 0.021	252	0.0181	6
11x	0.300	56 \ 0.021	378	0.0270	1
12x.1-12x.6	0.401	56 \ 0.021	504	0.0360	6
13x	0.601	56 \ 0.021	756	0.0539	1
14x	0.801	56 \ 0.021	1007	0.0720	1
15p	0.025	56 \ 0.021	32	0.0018	1
16p	0.050	56 \ 0.021	64	0.0036	1
17p	0.100	56 \ 0.021	128	0.0073	1
18p	0.200	56 \ 0.021	255	0.0145	1

Table 5.1: Crack models for numerical calculations. The models with an x attached to its number have intersection of cracks. The models with a p attached to its number have parallel cracks (normal to vertical direction). Note, 0.0001m is the size of grid spacing and the size of the crack region is always 1000*1000 grid points.

No.	f_{dom} (Hz)	P- wavelength (dom.) [0.0001 m]	S- wavelength (dom.) [0.0001 m]
1	2200000	23	13
2	800000	64	37
3	400000	128	74
4	120000	425	245
5	50000	1020	588
6	22000	2318	1338

Table 5.2: Information of the different wavelets of the numerical study. Note, 0.0001m is the size of grid spacing.

From the modeling point of view it is important to note that all computations are performed with second order spatial FD operators and with a second order time update. In order to reduce the dispersion error I model only with 25% of the allowed maximum time increment ($\gamma = 0.25 \gamma_{max}$; see section 3.5.3). The number of grid points per dominant wavelength N_λ depends on the wavelet of the modeling and is in general larger than 588 (see Table 5.2). Therefore, with this configuration my measurements are for a model with a crack density of $\rho = 0$ a velocity of $v_p = 5101.86 \frac{m}{s}$ (relative error: 0.036%) and $v_s = 2943.62 \frac{m}{s}$ (relative error: 0.013%). To obtain such accurate modeling results with up to 40000 time steps I have to use large scale parallel computers (e.g. Cray T3E). Owing to this computational cost I have to restrict myself to significant cases of model variations in determining the error bars.

Note, the number of grid points per dominant wavelength N_λ is also important in respect to small-scale structures in FD modeling. In Saenger et al. [2000] an accurate modeling of a single arbitrarily shaped crack with $N_\lambda \geq 14$ is shown. It is generally known that increasing of N_λ increases numerical accuracy for arbitrarily steep structures (e.g. [Robertsson, 1996]).

A very similar and successful experimental setup to test effective parameters in acoustic media can be found in Shapiro and Kneib [1993].

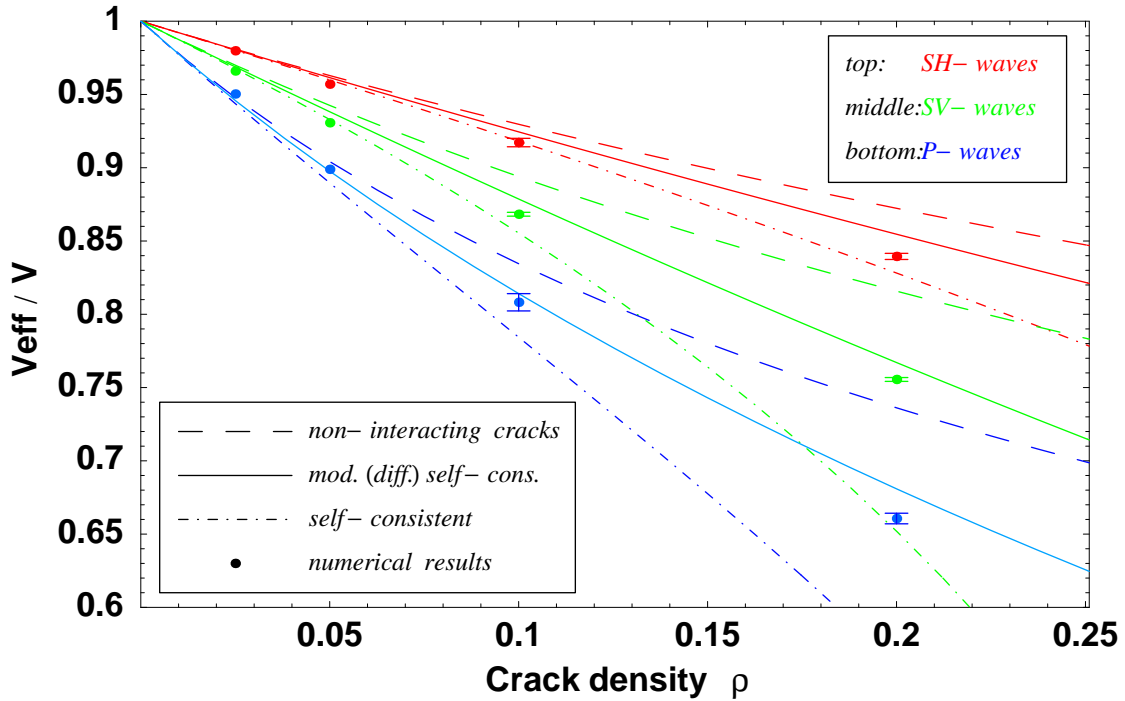


Figure 5.5: Normalized effective velocity versus crack density. Dots: Numerical results of this study, Lines: Different theoretical predictions. The error bar denotes the standard deviation for different model realizations (see Table 5.1).

5.3.2 Numerical results for non-intersecting cracks

The numerical results on effective wave velocities for non-intersecting cracks are depicted with dots in Figure 5.5. For comparison, the predictions of the three theories described above are shown in the same Figure with lines.

I show the normalized effective velocities for three types of waves. The relative decrease of the effective velocity for one given crack density is in the following succession: For SH-waves I obtain the smallest decrease followed by SV-waves. For P-waves it is largest. For each wave type I perform numerical FD-calculations with four different crack densities. For the case of non-intersecting cracks I use the models No. 4,5,6.1-6.5,7.1-7.11 ($2l = 0.0056m$, see Tab. 5.1) and the wavelet No. 5 ($\lambda_{\text{dom}}(S)=0.0588m$, $\lambda_{\text{dom}}(P)=0.1020m$, see Tab. 5.2). The ratio of the crack length to the dominant wavelength is given by the parameter p :

$$p = \frac{2l}{\lambda_{\text{dom}}} \quad (5.38)$$

(rectilinear cracks of length $2l$, dominant wavelength λ_{dom}). Hence for these calculations follows a value of $p = 0.095$ for S-waves, and $p = 0.055$ for P-waves. In agreement with

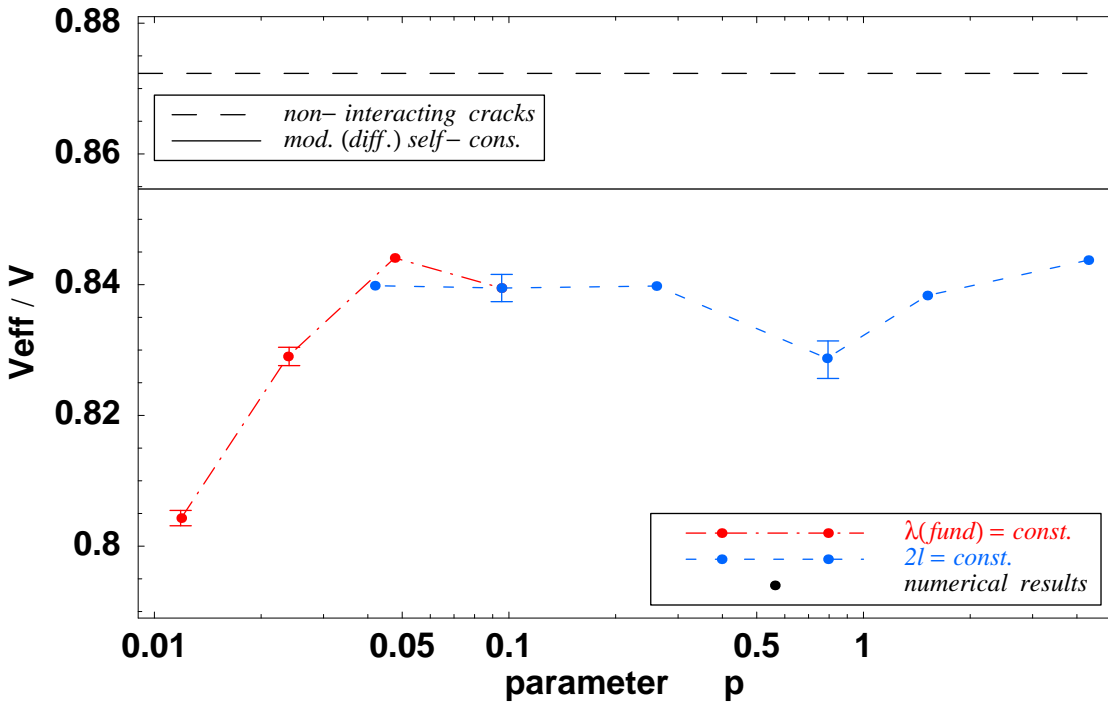


Figure 5.6: Normalized effective velocity (SH-waves) versus $p = 2l / \lambda_{\text{dom}}$ (normalized frequency), for crack density $\rho = 0.2$. Dots: Numerical results of this study, Two horizontal lines at the top: Different theoretical predictions. The error bar denotes the standard deviation for different model realizations (see Table 5.1). Note, the numerical result depicted at $p=0.095$ is depicted in Figure 5.5, too.

the paper of [Murai et al., 1995] this is a very good approximation for the long wavelength limit.

The aspect ratio of the cracks I used in my numerical experiments should not significantly influence the results of the three discussed theories for non-intersecting cracks (compare with [Douma, 1988]). A final result is that my numerical simulations of P-, SV- and SH-wave velocities are in an excellent agreement with the predictions of the modified (or differential) self-consistent theory.

Now I examine the influence on my results of the ratio of crack length to the dominant wavelength. The ratio is given by p (Eq. 5.38). I restrict myself to study only the influence with one single crack density ($\rho = 0.2$) and for shear waves with vibration direction perpendicular to the 2D-model. This enables me to compare my results with the results of Davis and Knopoff [1995] because they use the same mode of deformation and randomly distributed and randomly oriented cracks. In contrast to my study Murai et al. [1995] consider a fractured situation with randomly distributed parallel cracks and a crack density of $\rho \leq 0.02$.

There are two possibilities to vary the parameter p . The first possibility is to vary λ_{dom}

by using all wavelets in Table 5.2 and not to change the length of the cracks using model No. 7 (Table 5.1). The numerical results are shown in Figure 5.6 (dots joined with dashed line). The three theories for non-intersecting cracks mentioned above are derived for wavelengths much larger than the crack length (discussed e.g. by [Peacock and Hudson, 1990]). Therefore, it is interesting to observe that in a wide range of p (by vary λ_{dom}) there is no significant change of the effective velocity.

For the second curve in Figure 5.6 (dots joined with dashed-dotted line) I always use wavelet No. 5 and vary the length of the cracks using models No. 1.1-1.4,2.1-2.7,3,7.1-7.11 (see Table 5.2). Note, that with decreasing length of cracks the porosity of the fractured region increases. Hence, the decrease of the effective velocity for small values of p in this curve can be explained by the increasing influence of the porosity of the used models.

An additional result is that my calculated effective velocities (dots in Figure 5.6) always match the prediction by the modified self consistent theory (solid horizontal line) better than the prediction by the theory for non-interacting cracks (dashed horizontal line) for all values of p . This fact underlines the numerical based conclusion that the modified self consistent theory predicts effective velocities always in the most accurate way.

This conclusion is in contrast to some conclusions of Davis and Knopoff [1995]. They propose that the theory for non-interacting cracks has a wider validity range than expected. In connection with this I would like to note the following. The paper of Andrews and Ben-Zion [1997] shows that in respect to the accuracy FD methods are at least as good as the boundary integral methods. From the other hand the above mentioned conclusions of Davis and Knopoff [1995] are under discussion in the literature (e.g. [Liu et al., 2000]). A similar to Davis and Knopoff [1995] boundary integral study and an additional finite element study by Dahm and Becker [1998] suggest that crack interactions cannot be simply ignored for high crack densities. The corresponding conclusions of their study are in agreement with my conclusions. Moreover, even the trend that the numerically calculated effective velocities tend to be a bit lower than the effective velocities predicted by the MSC-theory shown by Dahm and Becker [1998] is in agreement with my numerical simulations. A more detailed discussion why the above mentioned discrepancy can arise in different studies is found in [Dahm and Becker, 1998].

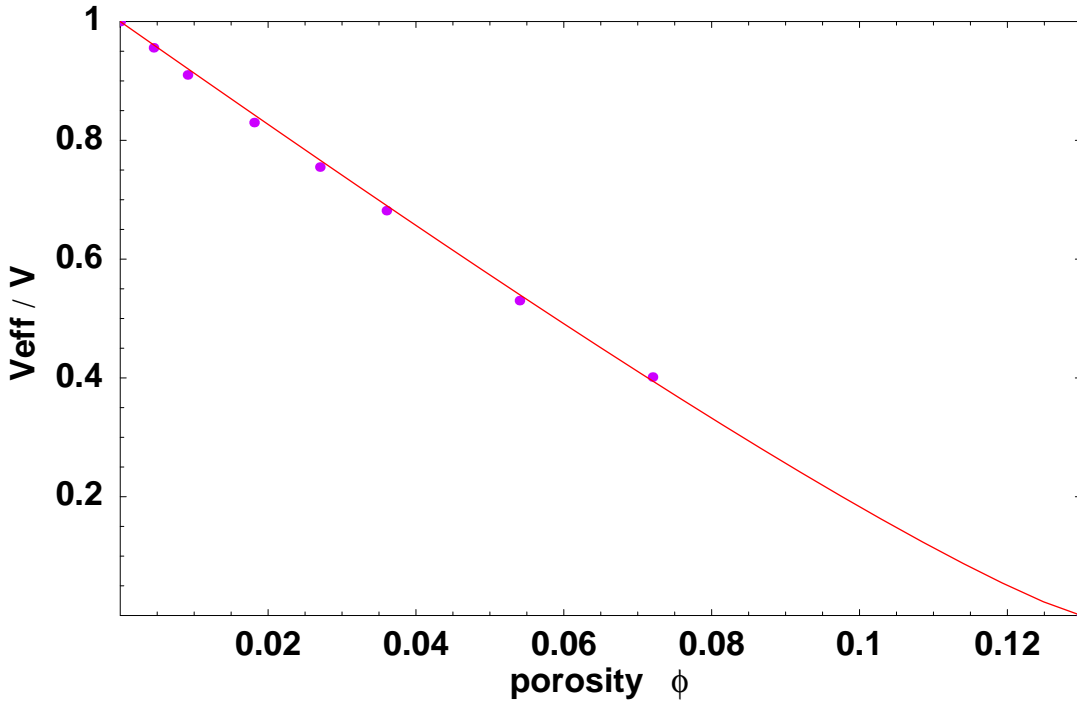


Figure 5.7: Normalized effective SH-wave velocities for intersecting cracks versus porosity. Dots: Numerical results, Line: Theoretical predictions of the modified DEM-theory.

5.3.3 Numerical results for intersecting cracks

My numerical results for intersecting cracks can be seen in Figure 5.7 and Figure 5.8. For the calculations of normalized effective velocities marked with dots I use always wavelet No. 5 (see Table 5.2). The models No. 8x,9x,10x,1-10x,6,11x,12x,1-12x,6,13x,14x for experiments are in Table 5.1. I show the calculation for three types of waves. The relative decrease of the effective velocity for one given porosity is in the following succession: For SH-waves I obtain the smallest decrease followed by SV-waves. For P-waves it is largest.

The numerical results shown in Figure 5.7 for SH(90°)-waves in a transversely isotropic fractured medium and the differential effective medium formulations for an isotropic fractured medium (!), including a critical porosity, are in a good agreement.

But in fact, my numerical results and the new CCD- formulation, including a critical crack density, are in an excellent agreement. It is important to note that the value of $n=0.5$, used to determine the effective velocities predicted by Eq. (5.28-5.30) in Figure 5.8, is found numerically (best fit).

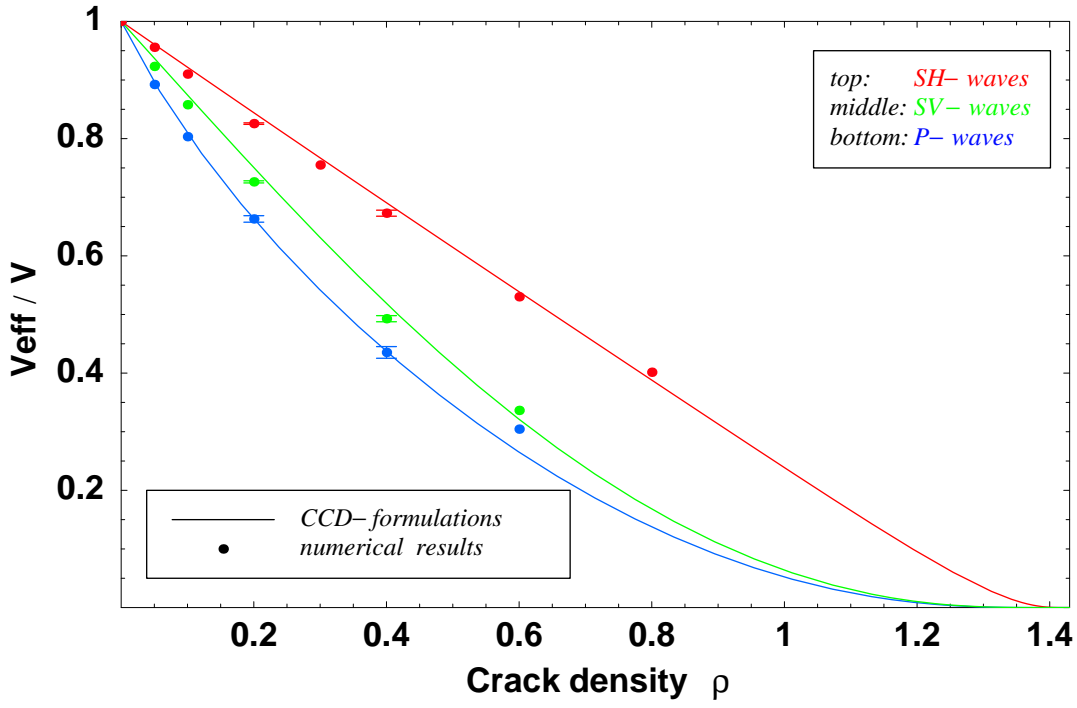


Figure 5.8: Normalized effective SH-, SV- and P-wave velocities for intersecting cracks versus crack density. Dots: Numerical results of this study, Lines: Theoretical predictions of the CCD-formulations. The error bar denotes the standard deviation for different model realizations (see Table 5.1).

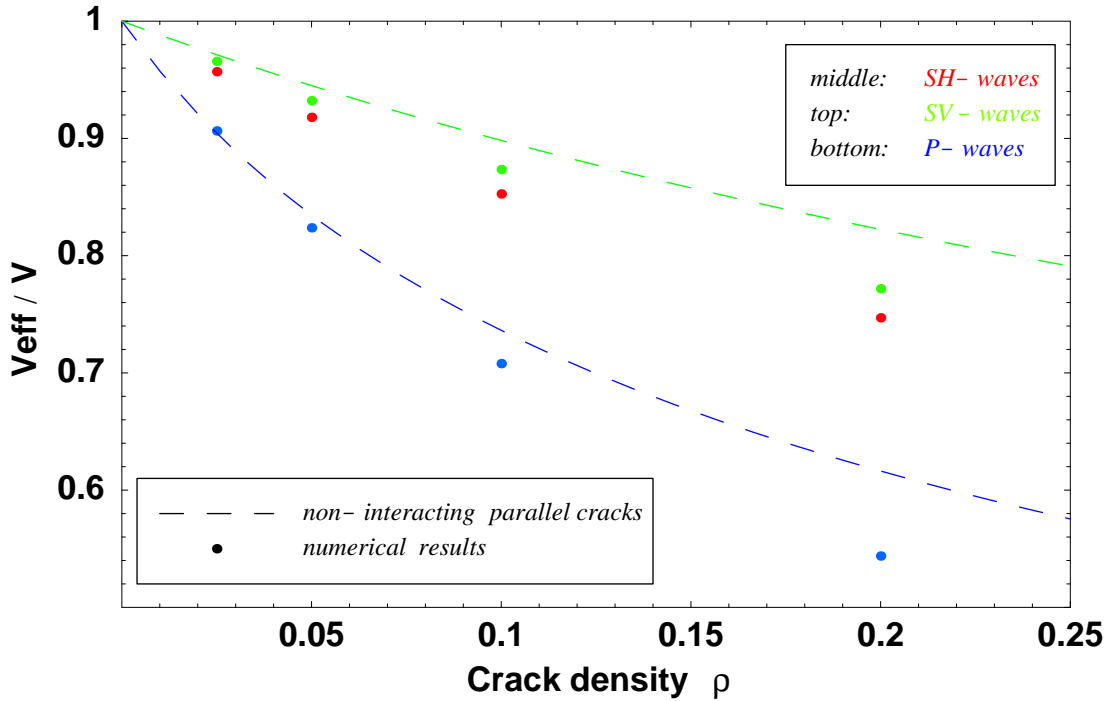


Figure 5.9: Normalized effective SH-, SV- and P-wave velocities for parallel cracks versus crack density. Dots: Numerical results, Dashed lines: Theoretical predictions of the theory for non-interacting parallel cracks.

5.3.4 Numerical results for parallel cracks

My numerical results for parallel cracks can be seen in Figure 5.9. For the calculations of normalized effective velocities marked with dots I use always wavelet No. 5 (see Table 5.2). Details of the models No. 15p-18p used for the experiments are displayed in Table 5.1. I show the calculations for three types of waves. The relative decrease of the effective velocity for one given crack density is in the following order: For $SV(90^\circ)$ -waves I obtain the smallest decrease followed by $SH(90^\circ)$ -waves. Note, this is in contrast to the numerical results for randomly oriented cracks. For $P(90^\circ)$ -waves the decrease of the effective velocity is largest.

The main result of the investigations in this section is the fact, that the non-interacting theory for parallel cracks can only be applied successfully to a dilute crack density.

5.4 Conclusions

The rotated staggered grid is a powerful numerical tool to calculate effective velocities in fractured media. My numerical modeling of elastic properties of dry rock skeletons can be considered as an efficient and well controlled computer experiment.

In this chapter I consider among others 2D isotropic (3D transversely isotropic) cracked media. I have numerically tested predictions of three different theoretical approaches: Theory for non-interacting cracks, self-consistent theory and modified self consistent theory. For non-intersecting rectilinear thin dry cracks the modified (differential) self consistent (MSC-) theory is most successful in predicting effective velocities for SV-, SH- and P-waves.

For the case of intersecting fractures it is important to take percolation behavior of the medium into account. The concept of the critical crack density must be introduced for explaining elastic properties of such media. I propose a heuristic approach called the critical crack density (CCD) formulation. This formulation introduces the critical crack density into the modified (differential) self consistent media theory. The CCD formulation predicts effective velocities for SV-, SH- and P-waves in fractured 2D-media with intersecting rectilinear thin dry cracks. The numerical results support predictions of this new formulation.

Chapter 6

Conclusions and perspectives

6.1 Extensions of the modeling scheme

6.1.1 General conclusions

The finite-difference (FD) method provides numerical solutions of the elastodynamic wave equation without physical approximations. In this thesis I present a rotated staggered grid (RSG) scheme [Saenger et al., 2000a] where all medium parameters are defined at appropriate positions within an elementary cell for the essential operations. Using this modified grid it is possible to simulate the propagation of elastic waves in a medium containing cracks, pores or free surfaces without applying boundary conditions. The question of numerical accuracy is clarified by a complete von Neumann style analysis. The stability criterion and the dispersion relations of the rotated staggered grid are similar to those of standard staggered grid schemes. As a result it turned out that the accuracy of the RSG is independent of the Poisson ratio. This fact is advantageous for modeling solid-liquid interfaces. In six synthetic examples I demonstrated successfully the wide range of applications of the rotated staggered FD technique in 2D and 3D media. In the following I present further perspectives of the new technique.

6.1.2 A new principle to solve other partial differential equations

Partial differential equations (PDE) are mathematical formulations of changing observable quantities. The elastodynamic wave equation is a so called hyperbolic PDE (simplest mathematical form: $\frac{\delta^2 u}{\delta t^2} = k \frac{\delta^2 u}{\delta x^2}$) which can be solved numerically by FD techniques. However, they are not only common for numerical solutions of the elastodynamic wave equation. For example heat flow can be described using a so-called parabolic PDE (simplest mathematical form: $\frac{\delta u}{\delta t} = k \frac{\delta^2 u}{\delta x^2}$). FD approaches to solve such problems are considered e.g. in Maucher et al. [1999] or in Karrenbach [1999]. From the modeling point of view only the time up-

date (see Section 3.2) is changing in comparison to the hyperbolic PDE. Therefore, the main idea of the rotated staggered grid, namely the combination of rotated and staggered spatial derivative operators can also be applied to other PDE's. This can be advantageous because of the new distribution of the modeling parameters.

6.1.3 Modeling viscoelastic wave propagation

Elasticity is a good model for mechanical wave propagation in a number of materials (e.g. rocks and metals). However, in reality these materials very often behave not perfectly elastic. Wave energy is gradually converted into heat. This inelastic behavior can be well described by viscoelastic models. The main idea is to model materials through their mechanical analogs using components such as springs and dashpots. The quality factor Q characterizes the attenuation of waves. Q labels the number of wavelengths a wave must propagate through the material before its amplitude drops by the factor $e^{-\pi}$. It requires special techniques to approximate a constant Q in a given frequency range when using a time domain FD scheme. Such techniques are described e.g. in Emmerich and Korn [1987]; Carcione et al. [1988]; Robertsson et al. [1994]; Karrenbach [1995]; Carcione [1995]. These methods can be straightforwardly incorporated into the rotated staggered finite difference scheme. Therefore, viscoelastic wave propagation in fractured structures without applying boundary conditions is a possible new application of the RSG method.

6.1.4 Modeling nonlinear wave propagation

Many numerical algorithms in geophysics assume linearity. Thus, they will work only on equations that behave linearly. For modeling nonlinear phenomena, the choice of algorithms becomes rather restrictive. FD algorithms have the advantage that they do not require any linearity assumptions in order to model nonlinear wave propagation [Karrenbach, 1995]. Hence, the linear stress-strain relation (see Eq. 2.14) used to calculate the stress in the FD scheme (see Section 3.2) has only to be replaced by a nonlinear stress-strain relation. However, this leads to the problem that it is much harder to calculate stability criteria properly, since many rigorous stability criteria are based on linearity. The common von Neumann style analysis uses linear transformations to calculate stability criteria and dispersion relations. Kosik [1993] makes use of a Crank-Nicholson FD scheme that is implicit and thus guarantees to exhibit stability for a certain range of parameters. However, how much such an implicit method averages out nonlinear effects is debatable. The explicit RSG finite-difference method presented in this thesis is a new possibility to handle nonlinear models, which include high material contrasts without applying any boundary conditions. There is no principal restriction to a nonlinear situation.

6.1.5 Modeling wave propagation in general anisotropic media

In Section 4.5 I demonstrated that the RSG technique can be applied to model elastic waves in transversal isotropic media. Furthermore, I showed in Section 3.3.2 that this technique can be even used in general anisotropic media. Here I want to point out that a major advantage of the RSG-method is that all elements of the stiffness tensor are located at one single position. In anisotropic media, the use of standard staggered grid schemes implies that some of the elements of the stress and strain tensors must be interpolated to calculate the Hook sum. This interpolation leads to additional errors in the wave properties [Igel et al., 1995]. Hence, one effect in practice is that standard FD schemes produce wrong reflections at interfaces. This problem can be smartly avoided by using the rotated staggered grid scheme.

6.2 Numerical Rock Physics

6.2.1 General conclusions

The rotated staggered grid allows an efficient and precise numerical study of effective velocities in fractured structures [Saenger and Shapiro, 2000b]. Using the RSG I modeled the propagation of plane waves through a set of different randomly cracked 2D media. These numerical experiments can be considered as a well controlled computer experiment to determine elastic properties of dry rock skeletons.

6.2.2 Effective velocities in 3D media

Similar considerations as in the 2D case to predict effective velocities (see Section 5) can be also performed in 3D fractured media. A 3D extension might be useful because most of the theories that predict effective elastic parameters are theories for randomly distributed heterogeneities in 3D media (e.g. [Hudson, 1981; Mukerji et al., 1995]). However, from the computational point of view the 3D approach is very expensive, because useful large-scale 3D numerical experiments can only be calculated on massive parallel computer devices.

6.2.3 Scattering attenuation in 2D and 3D media

Many theoretical estimates of scattering effects on attenuation have appeared (see Metha [1983] and Berryman [1992] for reviews). Most are in the long-wavelength limit and most assume that the concentration of scatterers is small, and thus only single scattering is considered. In this thesis I restricted myself to have a closer look to the effective velocities and obtained as a by-product to the numerical experiments the scattering attenuations of

the media. The attenuation values of the 2D experiments are given in Appendix C. A goal of a future study is the consideration of the relationship between scattering attenuation described by theory (e.g. [Hudson, 1981]) and the attenuation observed in numerical experiments using the rotated staggered finite-difference grid.

References

- Achenbach, J. D., Gautesen, A. K., and McMaken, H., *Ray Methods for Waves in Elastic Solids*, Pitman, Boston, 1982.
- Aki, K. and Richards, P. G., *Quantitative Seismology, Theory and Methods*, W.H. Freeman and Comp., San Francisco, 1980.
- Andrews, D. J. and Ben-Zion, Y., Wrinkle-like slip pulse on a fault between different materials, *Journal of Geophysical Research*, 102, No. B1, 553–571, 1997.
- Auld, B. A., *Acoustic Fields and Waves in Solids, Vol. 1*, John Wiley and Sons, New York, 1973.
- Berryman, J. G., Long-wave elastic anisotropy in transversely isotropic media, *Geophysics*, 44, 896–917, 1979.
- Berryman, J. G., Long-wavelength propagation in composite elastic media i. spherical inclusions and ii. ellipsoidal inclusions, *J. Acoust. Soc. Amer.*, 68, 1809–1831, 1980.
- Berryman, J. G., Single-scattering approximations for coefficients in biot's equations of poroelasticity, *J. Acoust. Soc. Amer.*, 91, 551–571, 1992.
- Birch, F., The velocity of compressional waves in rocks to 10 kilobars, part 2, *J. Geophys. Res.*, 66, 2199–2224, 1961.
- Bruner, W. M., Comment on "seismic velocities in dry and saturated cracked solids" by r. j. o'connell and b. budiansky, *J. Geophys. Res.*, 81, 2573–2576, 1976.
- Budiansky, B. and O'Connell, R. J., Elastic moduli of a cracked solid, *Int. J. Solids Struct.*, 12, 81–97, 1976.
- Burr, E., Gold, N., Grosse, C., and Reinhardt, H.-W., Simulation of ultrasonic flaw detection in concrete with a different percentage of air inclusions, *Otto-Graf-Journal*, 8, 19–29, 1997.
- Carcione, J. M., Constitutive model and wave equations for linear, viscoelastic, anisotropic media, *Geophysics*, 60, 537–548, 1995.
- Carcione, J. M., Kosloff, D., and Kosloff, R., Viscoacoustic wave propagation simulation in the earth, *Geophysics*, 53, 769–777, 1988.

- Carcione, J. M. and Wang, J. P., A chebyshev collocation method for the elastodynamic equation in generalized coordinates, *Comput. Fluid Dynamics J.*, 2, 269–290, 1993.
- Cerjan, C., Kosloff, D., Kosloff, R., and Reshef, M., A nonreflecting boundary condition for discrete acoustic-wave and elastic-wave equations (short note), *Geophysics*, 50, 705–708, 1985.
- Cerveny, V., Molotkov, I. A., and Psencik, I., *Ray Method in seismology*, Univ. of Karlova, 1977.
- Chatterjee, A., Mal, A., and Knopoff, L., Elastic moduli of a cracked solid, *Journal of Geophysical Research*, 83, 1785–1792, 1978.
- Cheng, C. H., Crack models for a transversely isotropic medium, *Journal of Geophysical Research*, 98(B1), 675–684, 1993.
- Claerbout, J. F., *Imaging the earth's interior*, Blackwell Scientific, Oxford, 1985.
- Clayton, R. and Engquist, B., Absorbing boundary conditions for acoustic and elastic wave equations, *Bulletin of the Seismological Society of America*, 67, 1529–1540, 1977.
- Cohen, G., Joly, P., and Tordjman, N., Construction and analysis of higher order finite elements with mass lumping for the wave equation, in *Proc. Second Internat. Conf. on Mathematical and Numerical Aspects of Wave Propagation*, Soc. for Ind. and Appl. Math., 1993, pp. 152–160.
- Cole, J. B., A nearly exact second-order finite-difference time-domain wave propagation algorithm on a coarse grid, *Computers in Physics*, 8, 730–734, 1994.
- Crampin, S., A review of wave motion in anisotropic and cracked media, *Wave Motion*, 3, 343–391, 1981.
- Crase, E., High-order (space and time) finite-difference modeling of the elastic wave equation, in *60th Annual Internat. Mtg., Soc. Expl. Geophys., Expanded Abstracts*, 1990, volume 90, pp. 987–991.
- Dablain, M. A., The application of high-order differencing to the scalar wave equation, *Geophysics*, 51, 54–66, 1986.
- Dahm, T. and Becker, T., On the elastic and viscous properties of media containing strongly interacting in-plane cracks, *Pure Appl. Geophys.*, 151, 1–16, 1998.
- Davis, P. M. and Knopoff, L., The elastic modulus of media containing strongly interacting antiplane cracks, *J. Geophys. Res.*, 100, 18.253–18.258, 1995.
- Douma, J., The effect of the aspect ratio on crack-induced anisotropy, *Geophysical Prospecting*, 36, 614–632, 1988.
- Eberle, K. and Gold, N., Impulswellenanalyse, *Materialprüfung*, 40(4), 144–148, 1998.

- Emmerich, H. and Korn, M., Incorporation of attenuation into time-domain computations of seismic wave fields, *Geophysics*, 52, 1252–1264, 1987.
- Eshelby, J. D., The determination of the elastic field of an ellipsoidal inclusion, and related problems, *Proc. Phys. Soc. London, A*, 241, 376–396, 1957.
- Fellinger, P., Marklein, R., Langenberg, K. J., and Klaholz, S., Numerical modelling of elastic wave propagation and scattering with efit - elastodynamic finite integration technique, *Wave Motion*, 21, 47–66, 1995.
- Fornberg, B., The pseudospectral method: Accurate representation of interfaces in elastic wave calculations, *Geophysics*, 53, 625–637, 1988.
- Frankel, A. and Clayton, R. W., Finite difference simulations of seismic scattering: Implications for the propagation of short-period seismic waves in the crust and models of crustal heterogeneity, *Journal of Geophysical Research*, 91, No. B6, 6465–6489, 1986.
- Frankel, A. and Leith, W., Evaluation of topographic effects on p- and s-waves of explosions at the northern novaya zemlya test site using 3-d numerical simulations, *Geophys. Res. Lett.*, 19, 1887–1890, 1992.
- Gold, N., Shapiro, S. A., and Burr, E., Modelling of high contrasts in elastic media using a modified finite difference scheme, in *67th Annual Internat. Mtg., Soc. Expl. Geophys., Expanded Abstracts*, 1997, volume 97, p. ST 14.6.
- Graves, R. W., Simulating seismic wave propagation in 3d elastic media using staggered-grid finite differences, *Bulletin of the Seismological Society of America*, 86, 1091–1106, 1996.
- Gubernatis, J. E., Domany, E., Krumhansl, J. H., and Huberman, M., The born approximation in the scattering of elastic waves by flaws, *J. appl. Phys.*, 48, 2812–2819, 1977.
- Henyey, F. S. and Pomphrey, N., Self-consistent elastic moduli of a cracked solid, *Geophys. Res. Lett.*, 9, 903–906, 1982.
- Hestholm, S. O. and Ruud, B. O., 2-d finite-difference elastic wave modeling including surface topography, *Geophys. Prosp.*, 42, 371–390, 1994.
- Holberg, O., Computational aspects of the choice of operator and sampling interval for numerical differentiation in large-scale simulation of wave phenomena, *Geophysical Prospecting*, 35, 629–655, 1987.
- Hubral, P., Theoretische untersuchung der wellenausbreitung in faserverbundwerkstoffen, in *Charakterisierung des Schädigungsverlaufes in Faserverbundwerkstoffen mittels zerstörungsfreier Prüfung, Sonderforschungsbereich 381, Ergebnisbericht 1997-1999*, Stuttgart, 1999, pp. 263–288.
- Hudson, J., Elastic moduli of a cracked solid, *Math. Proc. Camb. phil. Soc.*, 88, 371–384, 1980.

- Hudson, J. and Knopoff, L., Predicting the overall properties of composites – material with small-scale inclusions or cracks, *Pure Appl. Geophys.*, **131**, 551–576, 1989.
- Hudson, J. A., Wave speeds and attenuation of elastic waves in material containing cracks, *Geophys. J. Royal Astronom. Soc.*, **64**, 133–150, 1981.
- Igel, H., Mora, P., and Riollet, B., Anisotropic wave propagation through finite-difference grids, *Geophysics*, **60**, 1203–1216, 1995.
- Jih, R. S., McLaughlin, K. L., and Der, Z. A., Free-boundary conditions of arbitrary polygonal topography in a two-dimensional explicit elastic finite-difference scheme, *Geophysics*, **53**, 1045–1055, 1988.
- Jo, C. H., Shin, C. S., and Suh, J. H., An optimal 9-point, finite-difference, frequency-space, 2-d scalar wave extrapolator, *Geophysics*, **61**, 529–537, 1996.
- Kachanov, M., The elastic modulus of media containing strongly interacting antiplane cracks, *Appl. Mech. Rev.*, **45**(8), 304–335, 1992.
- Karrenbach, M., *Elastic tensor wavefields*, Ph.D. thesis, Stanford University, 1995.
- Karrenbach, M., *Modeling physical systems*, 1999.
- Kelly, K. R., Ward, R. W., Treitel, S., and Alford, R. M., Synthetic seismograms: A finite-difference approach, *Geophysics*, **41**, 2–27, 1976.
- Kelner, S., Bouchon, M., and Coutant, O., Numerical simulation of the propagation of p waves in fractured media, *Geophys. J. Int.*, **137**, 197–206, 1999.
- Kerner, C., Modeling of soft sediments and liquid solid interfaces: modified wavenumber summation method and application, *Geoph. Prosp.*, **38**, 111–137, 1990.
- Kindelan, M., Kamel, A., and Sguazzero, P., On the construction and efficiency of staggered numerical differentiators for the wave equation, *Geophysics*, **55**, 107–110, 1990.
- Kneib, G. and Kerner, C., Accurate and efficient seismic modelling in random media, *Geophysics*, **58**, 576–588, 1993.
- Knopoff, L., Energy release in earthquakes, *Geophys. J. R. Astron. Soc.*, pp. 44–52, 1958.
- Kosik, D. W., Propagation of a nonlinear seismic pulse in an anelastic homogeneous medium, *Geophysics*, **58**, 949–963, 1993.
- Kusnandi, van Baren, G., Mulder, W., Herman, G., and van Antwerpen, V., Sub-grid finite-difference modeling of wave propagation and diffusion in cracked media, in *70th Annual Internat. Mtg., Soc. Expl. Geophys., Expanded Abstracts*, 2000, volume 100, p. ST P1.2.
- Langenberg, K. J., Fellinger, P., Marklein, R., Zanger, P., Mayer, K., and Kreuter, T., Inverse methods and imaging, in *Evaluation of Materials and Structures by Quantitative Ultrasonics*, edited by J. D. Achenbach, Springer, 1993, pp. 317–398.

- Levander, A. R., Fourth-order finite-difference p-sv seismograms, *Geophysics*, 53, 1425–1436, 1988.
- Liu, E., Hudson, J. A., and Pointer, T., Equivalent medium representation of fractured rock, *Journal of Geophysical Research*, 105, No. B2, 2981–3000, 2000.
- Marfurt, K. J., Accuracy of finite-difference and finite-element modeling of the scalar and elastic wave equations, *Geophysics*, 49, 533–549, 1984.
- Maucher, U., Rist, U., Kloker, M., and Wagner, S., Dns of laminar-turbulent transition in separation bubbles, in *High Performance Computing in Science and Engineering '99*, Springer, 1999, pp. 279–294.
- Mavko, G., Mukerji, T., and Dvorkin, J., *The Rock Physics Handbook*, Cambridge University Press, Cambridge, 1998.
- Metha, C. H., Scattering theory of wave propagation in a two-phase medium, *Geophysics*, 48, 1359–1372, 1983.
- Moczo, P., Kristek, J., and Halada, L., 3d 4th-order staggered-grid finite-difference schemes: Stability and grid dispersion, *Bulletin of the Seismological Society of America*, p. in press, 2000.
- Moser, T. J. and Pajchel, J., Recursive seismic ray modelling: applications in inversion and vsp, *Geophysical Prospecting*, 45, 885–908, 1997.
- Mukerji, T., Berryman, J., Mavko, G., and Berge, P., Differential effective medium modeling of rock elastic moduli with critical porosity constraints, *Geophysical Research Letters*, 22(5), 555–558, 1995.
- Müller, T., *The Common Reflection Surface Stack Method*, Ph.D. thesis, University of Karlsruhe, 1999.
- Murai, Y., Kawahara, J., and Yamashita, T., Multiple scattering of sh waves in 2-d elastic media with distributed cracks, *Geophys. J. Int.*, 122, 925–937, 1995.
- Norris, A. N., A differential scheme for the effective moduli of composites, *Mech. of Mater.*, 4, 1–16, 1985.
- Nur, A., Effects of stress on velocity anisotropy in rocks with cracks, *Journal of Geophysical Research*, 76(8), 2022–2034, 1971.
- Nur, A., Critical porosity and the seismic velocities in rocks (abstract), *EOS Trans. AGU*, 73, 66, 1992.
- O'Brien, C. G., Hyman, M. A., and Kaplan, S., A study of the numerical solution of partial differential equations., *J. Math. Phys.*, 29, 223–251, 1951.
- O'Connell, R. J. and Budiansky, B., Seismic velocities in dry and saturated cracked solids, *J. Geophys. Res.*, 79, 5412–5426, 1974.

- O'Connell, R. J. and Budiansky, B., Reply, *J. Geophys. Res.*, **81**, 2577–2578, 1976.
- Peacock, S. and Hudson, J. A., Seismic properties of rocks with distributions of small cracks, *Geophys. J. Int.*, **102**, 471–484, 1990.
- Reinhardt, H.-W., Grosse, C., Weiler, B., Bohnert, J., and Windisch, N., P-wave propagation in setting and hardening concrete, *Otto-Graf-Journal*, **7**, 181–189, 1996.
- Robertsson, J. A., Blanch, J. O., and Symes, W. W., Viscoelastic finite difference modeling, *Geophysics*, **59**, 1444–1456, 1994.
- Robertsson, J. O. A., A numerical free-surface condition for elastic/viscoelastic finite-difference modeling in the presence of topography, *Geophysics*, **61**, 1921–1934, 1996.
- Robinson, P. C., Connectivity of fracture systems - a percolation theory approach, *J. Phys. A: Math. Gen.*, **16**, 605–614, 1983.
- Robinson, P. C., Numerical calculations of critical densities for lines and planes, *J. Phys. A: Math. Gen.*, **17**, 2823–2830, 1984.
- Rodrigues, D. and Mora, P., Analysis of a finite differences solution to 3-d elastic wave propagation, in *62th Annual Internat. Mtg., Soc. Expl. Geophys., Expanded Abstracts*, 1992, volume 92, pp. 1247–1250.
- Saenger, E. H., Gold, N., and Shapiro, S. A., Modeling of high contrasts in elastic media using a modified finite difference grid, in *Wave Inversion Technology: Annual Report No. 2*, 1998, pp. 145–153.
- Saenger, E. H., Gold, N., and Shapiro, S. A., Modeling of elastic waves in fractured media using the rotated staggered finite difference grid, in *69th Annual Internat. Mtg., Soc. Expl. Geophys., Expanded Abstracts*, 1999a, volume 99, p. STHRY 6.
- Saenger, E. H., Gold, N., and Shapiro, S. A., Modeling of high contrasts in elastic media using a modified finite-difference grid, in *4th Int. Conf. on Theoretical and Computational Acoustics, Trieste, Bolletino di Geofisica*, 1999b, p. 154.
- Saenger, E. H., Gold, N., and Shapiro, S. A., Modeling the propagation of elastic waves using a modified finite-difference grid, *Wave Motion*, **31**(1), 77–92, 2000a.
- Saenger, E. H., Hubral, P., Kirchner, A., Vieth, K.-U., Müller, T., and Shapiro, S. A., Summary of project 11172, in *High Performance Computing in Science and Engineering '99*, Springer, 1999c, pp. 26–51.
- Saenger, E. H., Müller, T. M., Sick, C., Priller, H., and Shapiro, S. A., Applications of the rotated staggered finite-difference grid, in *High Performance Computing in Science and Engineering 2000*, Springer, 2000b, p. submitted.
- Saenger, E. H. and Shapiro, S. A., Calculations of effective velocities in cracked media using the rotated staggered finite-difference grid, in *Wave Inversion Technology: Annual Report No. 3*, 1999a, pp. 79–91.

- Saenger, E. H. and Shapiro, S. A., Effective velocities in fractured media: A numerical study using the rotated staggered finite-difference grid, in *69th Annual Internat. Mtg., Soc. Expl. Geophys., Expanded Abstracts*, 1999b, volume 99, p. Workshop: Fracture Characterization and Imaging.
- Saenger, E. H. and Shapiro, S. A., Calculation of effective velocities in fractured media using the rotated staggered grid, in *62st Mtg. Eur. Assoc. Expl Geophys., Extended Abstracts*, European Association Of Geophysical Exploration, 2000a, pp. Session:D-34.
- Saenger, E. H. and Shapiro, S. A., Effective velocities in fractured media: A numerical study using the rotated staggered finite-difference grid, *J. Geophys. Res.*, p. submitted, 2000b.
- Saenger, E. H. and Shapiro, S. A., A numerical study of effective velocities in fractured media using the rotated staggered grid, in *70th Annual Internat. Mtg., Soc. Expl. Geophys., Expanded Abstracts*, 2000c, volume 100, p. ST 6.2.
- Sahimi, M., *Flow and Transport in Porous Media and Fractured Rock*, VCH, Weinheim, Germany, 1995.
- Seron, F. J., Badal, J., and Sabadell, F. J., A numerical laboratory for simulation and visualization of seismic wavefields, *Geophysical Prospecting*, 44, 603–642, 1996.
- Shapiro, S. A. and Kneib, G., Seismic attenuation by scattering: theory and numerical results, *Geophys. J. Int.*, 193(14), 373–391, 1993.
- Smith, G. D., *Numerical solution of partial differential equations: finite difference methods*, Clarendon press, Oxford, 1985.
- Strang, G. and Fix, G. J., *An analysis of the finite element method*, Prentice-Hall, 1973.
- Tal-Ezar, H., Kosloff, D., and Koren, Z., An accurate scheme for seismic forward modeling, *Geophysical Prospecting*, 35, 479–490, 1987.
- Tessmer, E., Kosloff, D., and Behle, A., Elastic wave propagation simulation in the presence of surface topography, *Geophys. J. Int.*, 108, 621–632, 1992.
- Thomsen, L., Weak elastic anisotropy, *Geophysics*, 51, 1954–1966, 1986.
- Timoshenko, S. P. and Goodier, J. N., *Theory of Elasticity*, McGraw-Hill, New York, 1934.
- van Vossen, R., Robertsson, J. O. A., and Chapman, C. H., Finite-difference modelling of wave propagation in a fluid/solid configuration, in *62st Mtg. Eur. Assoc. Expl Geophys., Extended Abstracts*, European Association Of Geophysical Exploration, 2000, pp. Session:C-41.
- Vidale, J. E. and Clayton, R. W., A stable free surface condition for two-dimensional elastic finite-difference simulations, *Geophysics*, 51, 2247–2249, 1986.

- Vieth, K.-U., Shapiro, S. A., and Hubral, P., Crack imaging in randomly heterogeneous media, in *High Performance Computing in Science and Engineering '99*, Springer, 1999, pp. 46–51.
- Viktorov, I. A., *Rayleigh and Lamb Waves*, Plenum Press, New York, 1967.
- Virieux, J., Velocity-stress finite-difference method, *Geophysics*, 51, 889–901, 1986.
- von Neumann, J., *Mathematische Grundlagen der Quantenmechanik*, Dover, New York, 1943.
- Stekl, I. and Pratt, R. G., Accurate viscoelastic modeling by frequency-domain finite differences using rotated operators, *Geophysics*, 63, 1779–1794, 1998.
- White, J. E., *Underground Sound: Application of seismic waves*, Elsevier, Amsterdam, 1983.
- Wu, T. T., The effect of inclusion shape on the elastic moduli of a two-phase material, *Int. J. Solids Struct.*, 2, 1–8, 1966.
- Yilmaz, O., *Seismic Data Processing*, Society of Exploration Geophysicists, Tulsa, Okla., 1987.
- Zimmermann, R. W., *Compressibility of sandstones*, Elsevier Science, Amsterdam, 1991.

Appendix A

Numerical Dispersion Relations

In this chapter I present the dispersion relations that are necessary to reproduce the Figures 3.3, 3.4, 3.5 and 3.6. The derivation is described in Section 3.5.2. The notation of the dispersion relations A.1 and A.2 is equal to the notation of Equation 3.40, 3.41 and 3.32 in Section 3.5.2.

Dispersion relation for the rotated staggered finite-difference grid (3D case, 2nd order time, 4th order space):

$$\begin{aligned}
& \sin^2 \left(\frac{\hat{\omega} \Delta t}{2} \right) = \\
& \frac{\Delta t^2 v_{p,s}^2}{\Delta z^2} \sin \left(\frac{\Delta z k_z}{2} \right)^2 \cos \left(\frac{\Delta x k_x}{2} \right)^2 \cos \left(\frac{\Delta y k_y}{2} \right)^2 \\
& \left(c_1 - 9 c_2 + 12 c_2 \cos \left(\frac{\Delta x k_x}{2} \right)^2 + \right. \\
& 12 c_2 \cos \left(\frac{\Delta y k_y}{2} \right)^2 - 16 c_2 \cos \left(\frac{\Delta x k_x}{2} \right)^2 \cos \left(\frac{\Delta y k_y}{2} \right)^2 + \\
& 36 c_2 \cos \left(\frac{\Delta z k_z}{2} \right)^2 - 48 c_2 \cos \left(\frac{\Delta x k_x}{2} \right)^2 \cos \left(\frac{\Delta z k_z}{2} \right)^2 - \\
& 48 c_2 \cos \left(\frac{\Delta y k_y}{2} \right)^2 \cos \left(\frac{\Delta z k_z}{2} \right)^2 + \\
& \left. 64 c_2 \cos \left(\frac{\Delta x k_x}{2} \right)^2 \cos \left(\frac{\Delta y k_y}{2} \right)^2 \cos \left(\frac{\Delta z k_z}{2} \right)^2 \right)^2 \\
& + \frac{\Delta t^2 v_{p,s}^2}{\Delta x^2} \cos \left(\frac{\Delta z k_z}{2} \right)^2 \sin \left(\frac{\Delta x k_x}{2} \right)^2 \cos \left(\frac{\Delta y k_y}{2} \right)^2 \\
& \left(c_1 - 9 c_2 + 36 c_2 \cos \left(\frac{\Delta x k_x}{2} \right)^2 + \right.
\end{aligned}$$

$$\begin{aligned}
& 12 c_2 \cos\left(\frac{\Delta y k_y}{2}\right)^2 - 48 c_2 \cos\left(\frac{\Delta x k_x}{2}\right)^2 \cos\left(\frac{\Delta y k_y}{2}\right)^2 + \\
& 12 c_2 \cos\left(\frac{\Delta z k_z}{2}\right)^2 - 48 c_2 \cos\left(\frac{\Delta x k_x}{2}\right)^2 \cos\left(\frac{\Delta z k_z}{2}\right)^2 - \\
& 16 c_2 \cos\left(\frac{\Delta y k_y}{2}\right)^2 \cos\left(\frac{\Delta z k_z}{2}\right)^2 + \\
& 64 c_2 \cos\left(\frac{\Delta x k_x}{2}\right)^2 \cos\left(\frac{\Delta y k_y}{2}\right)^2 \cos\left(\frac{\Delta z k_z}{2}\right)^2 \Big)^2 \\
& + \frac{\Delta t^2 v_{p,s}^2}{\Delta y^2} \cos\left(\frac{\Delta z k_z}{2}\right)^2 \cos\left(\frac{\Delta x k_x}{2}\right)^2 \sin\left(\frac{\Delta y k_y}{2}\right)^2 \\
& \quad \left(c_1 - 9 c_2 + 12 c_2 \cos\left(\frac{\Delta x k_x}{2}\right)^2 + \right. \\
& 36 c_2 \cos\left(\frac{\Delta y k_y}{2}\right)^2 - 48 c_2 \cos\left(\frac{\Delta x k_x}{2}\right)^2 \cos\left(\frac{\Delta y k_y}{2}\right)^2 + \\
& 12 c_2 \cos\left(\frac{\Delta z k_z}{2}\right)^2 - 16 c_2 \cos\left(\frac{\Delta x k_x}{2}\right)^2 \cos\left(\frac{\Delta z k_z}{2}\right)^2 - \\
& \quad \left. 48 c_2 \cos\left(\frac{\Delta y k_y}{2}\right)^2 \cos\left(\frac{\Delta z k_z}{2}\right)^2 + \right. \\
& \quad \left. 64 c_2 \cos\left(\frac{\Delta x k_x}{2}\right)^2 \cos\left(\frac{\Delta y k_y}{2}\right)^2 \cos\left(\frac{\Delta z k_z}{2}\right)^2 \right)^2 \tag{A.1}
\end{aligned}$$

Dispersion relation for the rotated staggered finite-difference grid (2D case, second order time, eight order space):

$$\begin{aligned}
& \sin^2\left(\frac{\hat{\omega} \Delta t}{2}\right) = \\
& \frac{\Delta t^2 v_{p,s}^2}{\Delta z^2} \cos\left(\frac{\Delta x k_x}{2}\right)^2 \sin\left(\frac{\Delta z k_z}{2}\right)^2 \\
& \left(c_1 + 3 c_2 + 5 c_3 + 7 c_4 - 4 c_2 \cos\left(\frac{\Delta x k_x}{2}\right)^2 - 20 c_3 \cos\left(\frac{\Delta x k_x}{2}\right)^2 - \right. \\
& \quad 56 c_4 \cos\left(\frac{\Delta x k_x}{2}\right)^2 + 16 c_3 \cos\left(\frac{\Delta x k_x}{2}\right)^4 + \\
& \quad 112 c_4 \cos\left(\frac{\Delta x k_x}{2}\right)^4 - 64 c_4 \cos\left(\frac{\Delta x k_x}{2}\right)^6 - \\
& \quad 12 c_2 \cos\left(\frac{\Delta z k_z}{2}\right)^2 - 60 c_3 \cos\left(\frac{\Delta z k_z}{2}\right)^2 - 168 c_4 \cos\left(\frac{\Delta z k_z}{2}\right)^2 + \\
& \quad 16 c_2 \cos\left(\frac{\Delta x k_x}{2}\right)^2 \cos\left(\frac{\Delta z k_z}{2}\right)^2 + 240 c_3 \cos\left(\frac{\Delta x k_x}{2}\right)^2 \cos\left(\frac{\Delta z k_z}{2}\right)^2 + \\
& \quad 1344 c_4 \cos\left(\frac{\Delta x k_x}{2}\right)^2 \cos\left(\frac{\Delta z k_z}{2}\right)^2 - 192 c_3 \cos\left(\frac{\Delta x k_x}{2}\right)^4 \cos\left(\frac{\Delta z k_z}{2}\right)^2 -
\end{aligned}$$

$$\begin{aligned}
& 2688 c_4 \cos\left(\frac{\Delta x k_x}{2}\right)^4 \cos\left(\frac{\Delta z k_z}{2}\right)^2 + 1536 c_4 \cos\left(\frac{\Delta x k_x}{2}\right)^6 \cos\left(\frac{\Delta z k_z}{2}\right)^2 + \\
& 80 c_3 \cos\left(\frac{\Delta z k_z}{2}\right)^4 + 560 c_4 \cos\left(\frac{\Delta z k_z}{2}\right)^4 - 320 c_3 \cos\left(\frac{\Delta x k_x}{2}\right)^2 \cos\left(\frac{\Delta z k_z}{2}\right)^4 - \\
& 4480 c_4 \cos\left(\frac{\Delta x k_x}{2}\right)^2 \cos\left(\frac{\Delta z k_z}{2}\right)^4 + 256 c_3 \cos\left(\frac{\Delta x k_x}{2}\right)^4 \cos\left(\frac{\Delta z k_z}{2}\right)^4 + \\
& 8960 c_4 \cos\left(\frac{\Delta x k_x}{2}\right)^4 \cos\left(\frac{\Delta z k_z}{2}\right)^4 - 5120 c_4 \cos\left(\frac{\Delta x k_x}{2}\right)^6 \cos\left(\frac{\Delta z k_z}{2}\right)^4 - \\
& 448 c_4 \cos\left(\frac{\Delta z k_z}{2}\right)^6 + 3584 c_4 \cos\left(\frac{\Delta x k_x}{2}\right)^2 \cos\left(\frac{\Delta z k_z}{2}\right)^6 - \\
& 7168 c_4 \cos\left(\frac{\Delta x k_x}{2}\right)^4 \cos\left(\frac{\Delta z k_z}{2}\right)^6 + 4096 c_4 \cos\left(\frac{\Delta x k_x}{2}\right)^6 \cos\left(\frac{\Delta z k_z}{2}\right)^6 \Big)^2 \\
& + \frac{\Delta t^2 v_{p,s}^2}{\Delta x^2} \cos\left(\frac{\Delta z k_z}{2}\right)^2 \sin\left(\frac{\Delta x k_x}{2}\right)^2 \\
& \left(c_1 + 3 c_2 + 5 c_3 + 7 c_4 - 12 c_2 \cos\left(\frac{\Delta x k_x}{2}\right)^2 - 60 c_3 \cos\left(\frac{\Delta x k_x}{2}\right)^2 - \right. \\
& \quad 168 c_4 \cos\left(\frac{\Delta x k_x}{2}\right)^2 + 80 c_3 \cos\left(\frac{\Delta x k_x}{2}\right)^4 + \\
& \quad 560 c_4 \cos\left(\frac{\Delta x k_x}{2}\right)^4 - 448 c_4 \cos\left(\frac{\Delta x k_x}{2}\right)^6 - \\
& \quad 4 c_2 \cos\left(\frac{\Delta z k_z}{2}\right)^2 - 20 c_3 \cos\left(\frac{\Delta z k_z}{2}\right)^2 - 56 c_4 \cos\left(\frac{\Delta z k_z}{2}\right)^2 + \\
& \quad 16 c_2 \cos\left(\frac{\Delta x k_x}{2}\right)^2 \cos\left(\frac{\Delta z k_z}{2}\right)^2 + 240 c_3 \cos\left(\frac{\Delta x k_x}{2}\right)^2 \cos\left(\frac{\Delta z k_z}{2}\right)^2 + \\
& \quad 1344 c_4 \cos\left(\frac{\Delta x k_x}{2}\right)^2 \cos\left(\frac{\Delta z k_z}{2}\right)^2 - 320 c_3 \cos\left(\frac{\Delta x k_x}{2}\right)^4 \cos\left(\frac{\Delta z k_z}{2}\right)^2 - \\
& \quad 4480 c_4 \cos\left(\frac{\Delta x k_x}{2}\right)^4 \cos\left(\frac{\Delta z k_z}{2}\right)^2 + 3584 c_4 \cos\left(\frac{\Delta x k_x}{2}\right)^6 \cos\left(\frac{\Delta z k_z}{2}\right)^2 + \\
& \quad 16 c_3 \cos\left(\frac{\Delta z k_z}{2}\right)^4 + 112 c_4 \cos\left(\frac{\Delta z k_z}{2}\right)^4 - 192 c_3 \cos\left(\frac{\Delta x k_x}{2}\right)^2 \cos\left(\frac{\Delta z k_z}{2}\right)^4 - \\
& \quad 2688 c_4 \cos\left(\frac{\Delta x k_x}{2}\right)^2 \cos\left(\frac{\Delta z k_z}{2}\right)^4 + 256 c_3 \cos\left(\frac{\Delta x k_x}{2}\right)^4 \cos\left(\frac{\Delta z k_z}{2}\right)^4 + \\
& \quad 8960 c_4 \cos\left(\frac{\Delta x k_x}{2}\right)^4 \cos\left(\frac{\Delta z k_z}{2}\right)^4 - 7168 c_4 \cos\left(\frac{\Delta x k_x}{2}\right)^6 \cos\left(\frac{\Delta z k_z}{2}\right)^4 - \\
& \quad 64 c_4 \cos\left(\frac{\Delta z k_z}{2}\right)^6 + 1536 c_4 \cos\left(\frac{\Delta x k_x}{2}\right)^2 \cos\left(\frac{\Delta z k_z}{2}\right)^6 - \\
& \quad 5120 c_4 \cos\left(\frac{\Delta x k_x}{2}\right)^4 \cos\left(\frac{\Delta z k_z}{2}\right)^6 + 4096 c_4 \cos\left(\frac{\Delta x k_x}{2}\right)^6 \cos\left(\frac{\Delta z k_z}{2}\right)^6 \Big)^2 \quad (\text{A.2})
\end{aligned}$$

Appendix B

Computational implementation of the rotated staggered grid

For the computational implementation of the rotated staggered grid (RSG) I modified the program “ULTIMOD” written by Martin Karrenbach and described in [Karrenbach, 1995]. The calculation of the spatial derivatives is the heart in every finite-difference algorithm. Therefore I replaced the subroutine conv1dc(), which is used to calculate the standard staggered spatial derivatives by the subroutine conv1dc45rotate() which calculates the spatial derivatives in the new directions of the RSG method in 2D and 3D (see Equations 3.14 and 3.15 for the 2D case and Equations 3.20, 3.21 and 3.22 for the 3D case). Note, that it is necessary to calculate two spatial derivatives to solve the elastodynamic wave equation:

$$\ddot{u}_i(\mathbf{r}, t) = \frac{1}{\rho(\mathbf{r})} \{ [c_{ijkl}(\mathbf{r}) \underbrace{\overbrace{u_{k,l}(\mathbf{r}, t)}_{spatial\ derivative}}_{spatial\ derivative}]_{,j} + f_i(\mathbf{r}, t) \}$$

In the subroutine conv1dc45rotate() (shown below) the calculation of the first spatial derivative is marked with “the gradient” and the calculation of the second spatial derivative is marked with “the divergence”.

```
subroutine conv1dc45rotate(conj,u,t,k,w,sidx,axis,&
help2,bnd,m,rho3)
use SHARED_PARAMS
implicit none
integer conj, t,k, sidx
integer axis
real scale
real u(:,:,:,:,:,::)
```

```

!HPF$ distribute u(BLOCK,BLOCK,BLOCK,*,*)
real w(:,:,:,:)
!HPF$ distribute w(BLOCK,BLOCK,BLOCK,*)
real m(:,:,:)
!HPF$ distribute m(BLOCK,BLOCK,BLOCK)
integer bnd(:,:,:)
!HPF$ distribute bnd(BLOCK,BLOCK,BLOCK)
real rho3(:,:,:)
!HPF$ distribute rho3(BLOCK,BLOCK,BLOCK)
integer ishift

real fakt,help2
integer i1,i2,i3
integer iZ,iX,iY

scale=help2
if (ndim==3) then

  if (conj==0) then # ``the gradient'', 3D
    do ishift = nlo-stagger, nhi-stagger
      fakt=coef(ishift+stagger)*scale

      if (axis==1) then
        do iX=1-ishift,ishift,2*ishift-1
        do iY=1-ishift,ishift,2*ishift-1
        forall(i1=1+stagger-nlo:nz+2*nbound1-nhi+stagger,&
        i2=1+nhi:2*nbound2+nx-nhi,i3=1+nhi:2*nbound3+ny-nhi)
          w(i1,i2,i3,sidx)=w(i1,i2,i3,sidx) + &
          fakt * u(i1+ishift,i2+iX,i3+iY,k,t)
        endforall
      enddo
      enddo
      endif

      if (axis==2) then
        do iZ=1-ishift,ishift,2*ishift-1
        do iY=1-ishift,ishift,2*ishift-1
        forall(i1=1+nhi:2*nbound1+nz-nhi,&
        i2=1+stagger-nlo:nx+2*nbound2-nhi+stagger,&
        i3=1+nhi:2*nbound2+ny-nhi)
          w(i1,i2,i3,sidx)=w(i1,i2,i3,sidx) + &
          fakt * u(i1+iZ,i2+ishift,i3+iY,k,t)
        endforall
      enddo
      enddo
    endif
  endif
endif

```

```

endif

if (axis==3) then
do iZ=1-ishift,ishift,2*ishift-1
do ix=1-ishift,ishift,2*ishift-1
forall(i1=1+nhi:2*nbound1+nx-nhi,&
i2=1+nhi:2*nbound2+ny-nhi,&
i3=1+stagger-nlo:ny+2*nbound3-nhi+stagger)
w(i1,i2,i3,sidx)=w(i1,i2,i3,sidx) + &
fakt * u(i1+iZ,i2+ix,i3+ishift,k,t)
endforall
enddo
enddo
endif

enddo

else      # ``the divergence'', 3D

do ishift = nlo-stagger, nhi-stagger
fakt=coef(ishift+stagger)*scale

if (axis==1) then
do ix=-1-ishift,ishift,2*ishift+1
do iy=-1-ishift,ishift,2*ishift+1
forall(i1=1+stagger-nlo:ny+2*nbound1-nhi+stagger,&
i2=1+nhi:2*nbound2+nx-nhi,i3=1+nhi:2*nbound3+ny-nhi)
u(i1,i2,i3,k,t)=u(i1,i2,i3,k,t) +&
fakt * w(i1+ishift,i2+ix,i3+iy,sidx)
endforall
enddo
enddo
endif

if (axis==2) then
do iz=-1-ishift,ishift,2*ishift+1
do iy=-1-ishift,ishift,2*ishift+1
forall(i1=1+nhi:2*nbound1+nx-nhi,&
i2=1+stagger-nlo:ny+2*nbound2-nhi+stagger,&
i3=1+nhi:2*nbound3+ny-nhi)
u(i1,i2,i3,k,t)=u(i1,i2,i3,k,t) + &
fakt * w(i1+iZ,i2+ishift,i3+iy,sidx)
endforall
enddo

```

```

enddo
endif

if (axis==3) then
do iZ=-1-ishift,ishift,2*ishift+1
do iX=-1-ishift,ishift,2*ishift+1
forall(i1=1+nhi:2*nbound1+nz-nhi,&
i2=1+nhi:2*nbound2+nx-nhi,&
i3=1+stagger-nlo:ny+2*nbound3-nhi+stagger)
u(i1,i2,i3,k,t)=u(i1,i2,i3,k,t) + &
fakt * w(i1+iZ,i2+ix,i3+ishift,sidx)
endforall
enddo
enddo
endif

enddo
endif

else

if (conj==0) then      # ``the gradient'', 2D
do ishift = nlo-stagger, nhi-stagger
fakt=coef(ishift+stagger)*scale
if (xcb==0) then      # no circular boundary conditions

if (axis==1) then
forall(i1=1+stagger-nlo:nz+2*nbound1-nhi+stagger,&
i2=1+nhi:2*nbound2+nx-nhi)
m(i1,i2,1)=u(i1+ishift,i2+ishift,1,k,t) + &
u(i1+ishift,i2-ishift+1,1,k,t)
endforall
endif

if (axis==2) then
forall(i1=1+nhi:2*nbound1+nz-nhi,&
i2=1+stagger-nlo:ny+2*nbound2-nhi+stagger)
m(i1,i2,1)=u(i1+ishift,i2+ishift,1,k,t) + &
u(i1-ishift+1,i2+ishift,1,k,t)
endforall
endif

else      # circular boundary conditions

```

```

if (axis==1) then
forall(i1=1+stagger-nlo:nz+2*nbound1-nhi+stagger,&
i2=nbound2+1-5:nbound2+nx+5)
m(i1,i2,1)=u(i1+ishift,i2+ishift,1,k,t) +&
u(i1+ishift,i2-ishift+1,1,k,t)
endforall
endif

if (axis==2) then
forall(i1=1+nhi:2*nbound1+nz-nhi,&
i2=nbound2+1-5:nbound2+nx+5)
m(i1,i2,1)=u(i1+ishift,i2+ishift,1,k,t) + &
u(i1-ishift+1,i2+ishift,1,k,t)
endforall
endif

endif

if (xcb==0) then # no circular boundary conditions
w(:,:,:,sidx) = w(:,:,:,sidx) + fakt * m(:,:,:)
else           # circular boundary conditions
w(:,nbound2+1-5:nbound2+nx+5,:,sidx) = &
w(:,nbound2+1-5:nbound2+nx+5,:,sidx) + fakt * &
m(:,nbound2+1-5:nbound2+nx+5,:)
endif

enddo

else          # ``the divergence'', 2D

do ishift = nlo-stagger, nhi-stagger
fakt=coef(ishift+stagger)*scale

if (xcb==0) then # no circular boundary conditions

if (axis==1) then
forall(i1=1+stagger-nlo:nz+2*nbound1-nhi+stagger,&
i2=1+nhi:2*nbound2+nx-nhi)
m(i1,i2,1)=w(i1+ishift,i2+ishift,1,sidx) + &
w(i1+ishift,i2-ishift-1,1,sidx)
endforall
endif

if (axis==2) then
forall(i1=1+nhi:2*nbound1+nz-nhi,&

```

```

i2=1+stagger-nlo:nx+2*nbound2-nhi+stagger)
m(i1,i2,1)=w(i1+ishift,i2+ishift,1,sidx) + &
w(i1-ishift-1,i2+ishift,1,sidx)
endforall
endif

else    # circular boundary conditions

if (axis==1) then
forall(i1=1+stagger-nlo:nz+2*nbound1-nhi+stagger,&
i2=nbound2+1:nbound2+nx)
m(i1,i2,1)=w(i1+ishift,i2+ishift,1,sidx) + &
w(i1+ishift,i2-ishift-1,1,sidx)
endforall
endif
if (axis==2) then
forall(i1=1+nhi:2*nbound1+nz-nhi,&
i2=nbound2+1:nbound2+nx)
m(i1,i2,1)=w(i1+ishift,i2+ishift,1,sidx) + &
w(i1-ishift-1,i2+ishift,1,sidx)
endforall
endif

endif

u(:,:,k,t)=u(:,:,k,t) + fakt * m(:,:, :)

enddo

endif

endif
return
end

```

Appendix C

Effective velocities in fractured media: database

In this chapter you can find the exact results of the numerical experiments discussed in chapter 5 . The symbols in the Tables denotes:

- I := Intersection of cracks with: y=yes, n=no, p=parallel cracks
- ρ := Crack density
- l := length of a single crack [0.0001m]
- asp. := aspect ratio of a single crack
- N := Number of cracks in the cracked region (size of the cracked region : 1000 * 1000 grid points)
- ϕ := porosity
- v_p := P-wave velocity of the homogeneous background [m/s]
- v_s := S-wave velocity of the homogeneous background [m/s]
- ρ_g := gravitational density of the homogeneous background [kg/m^3]
- R := realisation number of the model
- V_{EX} := Effective velocity [m/s]
- V_N := Normalized effective velocity
- TR := Transmission of the plane wave

Database of Figure 5.5												
$v_{SV}(90^\circ)$ (wavelet No. 5 of Table 5.2)												
I	ρ	1	asp.	N	ϕ	vp	vs	ρ_g	R	V_{EX}	V_N	TR
n	0.025	56	0.021	31	0.0022	5100	2944	2700	0	2884.56	0.980	99.51%
n	0.050	56	0.021	63	0.0046	5100	2944	2700	0	2817.51	0.957	99.23%
n	0.100	56	0.021	126	0.0091	5100	2944	2700	0	2699.97	0.917	98.20%
n	0.100	56	0.021	126	0.0091	5100	2944	2700	1	2718.22	0.923	98.11%
n	0.100	56	0.021	126	0.0091	5100	2944	2700	3	2677.54	0.909	98.09%
n	0.100	56	0.021	126	0.0091	5100	2944	2700	4	2705.01	0.919	97.81%
n	0.200	56	0.021	252	0.0181	5100	2944	2700	0	2491.75	0.846	96.20%
n	0.200	56	0.021	252	0.0180	5100	2944	2700	1	2483.71	0.844	96.04%
n	0.200	56	0.021	252	0.0180	5100	2944	2700	2	2453.92	0.833	96.76%
n	0.200	56	0.021	252	0.0179	5100	2944	2700	4	2435.44	0.827	94.22%
n	0.200	56	0.021	252	0.0182	5100	2944	2700	5	2491.42	0.846	95.94%
n	0.200	56	0.021	252	0.0182	5100	2944	2700	6	2459.03	0.835	95.53%
n	0.200	56	0.021	252	0.0179	5100	2944	2700	7	2469.33	0.839	96.18%
n	0.200	56	0.021	252	0.0180	5100	2944	2700	8	2492.35	0.847	96.00%
n	0.200	56	0.021	252	0.0180	5100	2944	2700	9	2458.43	0.835	94.62%
n	0.200	56	0.021	252	0.0182	5100	2944	2700	10	2479.10	0.842	96.03%
$v_{SH}(90^\circ)$ (wavelet No. 5 of Table 5.2)												
n	0.025	56	0.021	31	0.0022	5100	2944	2700	0	2843.95	0.966	99.39%
n	0.050	56	0.021	63	0.0046	5100	2944	2700	0	2739.92	0.931	98.60%
n	0.100	56	0.021	126	0.0091	5100	2944	2700	0	2568.23	0.872	97.25%
n	0.100	56	0.021	126	0.0091	5100	2944	2700	1	2543.73	0.864	95.94%
n	0.100	56	0.021	126	0.0091	5100	2944	2700	2	2555.75	0.868	96.46%
n	0.100	56	0.021	126	0.0091	5100	2944	2700	3	2557.39	0.869	95.93%
n	0.100	56	0.021	126	0.0091	5100	2944	2700	4	2555.75	0.868	95.07%
n	0.200	56	0.021	252	0.0181	5100	2944	2700	0	2235.02	0.759	91.47%
n	0.200	56	0.021	252	0.0180	5100	2944	2700	1	2223.34	0.755	90.62%
n	0.200	56	0.021	252	0.0180	5100	2944	2700	2	2246.06	0.763	93.17%
n	0.200	56	0.021	252	0.0181	5100	2944	2700	3	2206.90	0.750	89.87%
n	0.200	56	0.021	252	0.0179	5100	2944	2700	4	2234.77	0.759	90.86%
n	0.200	56	0.021	252	0.0182	5100	2944	2700	5	2217.42	0.753	88.99%
n	0.200	56	0.021	252	0.0182	5100	2944	2700	6	2209.34	0.750	90.23%
n	0.200	56	0.021	252	0.0179	5100	2944	2700	7	2227.55	0.757	90.86%
n	0.200	56	0.021	252	0.0180	5100	2944	2700	8	2234.52	0.759	91.11%
n	0.200	56	0.021	252	0.0180	5100	2944	2700	9	2208.61	0.750	88.79%
n	0.200	56	0.021	252	0.0182	5100	2944	2700	10	2223.34	0.755	90.69%

Table C.1: This Table contains information of the different numerical experiments shown in Figure 5.5 .

Database of Figure 5.5												
I	ρ	l	asp.	N	ϕ	vp	vs	ρ_g	R	V_{EX}	V_N	TR
$v_P(90^\circ)$ (wavelet No. 5 of Table 5.2)												
n	0.025	56	0.021	31	0.0022	5100	2944	2700	0	4846.64	0.950	99.36%
n	0.050	56	0.021	63	0.0046	5100	2944	2700	0	4584.46	0.899	98.47%
n	0.100	56	0.021	126	0.0091	5100	2944	2700	0	4143.73	0.812	95.51%
n	0.100	56	0.021	126	0.0091	5100	2944	2700	1	4208.99	0.825	95.27%
n	0.100	56	0.021	126	0.0091	5100	2944	2700	2	4028.77	0.790	94.71%
n	0.100	56	0.021	126	0.0091	5100	2944	2700	3	4087.94	0.802	94.47%
n	0.100	56	0.021	126	0.0091	5100	2944	2700	4	4139.44	0.811	93.75%
n	0.200	56	0.021	252	0.0181	5100	2944	2700	0	3411.47	0.669	89.15%
n	0.200	56	0.021	252	0.0180	5100	2944	2700	1	3414.61	0.670	86.07%
n	0.200	56	0.021	252	0.0180	5100	2944	2700	2	3343.10	0.656	89.88%
n	0.200	56	0.021	252	0.0181	5100	2944	2700	3	3341.44	0.655	86.46%
n	0.200	56	0.021	252	0.0179	5100	2944	2700	4	3249.66	0.637	82.71%
n	0.200	56	0.021	252	0.0182	5100	2944	2700	5	3456.27	0.678	88.05%
n	0.200	56	0.021	252	0.0182	5100	2944	2700	6	3311.73	0.649	85.62%
n	0.200	56	0.021	252	0.0179	5100	2944	2700	7	3380.75	0.663	87.21%
n	0.200	56	0.021	252	0.0180	5100	2944	2700	8	3440.90	0.675	88.58%
n	0.200	56	0.021	252	0.0180	5100	2944	2700	9	3332.03	0.653	84.14%
n	0.200	56	0.021	252	0.0182	5100	2944	2700	10	3379.61	0.663	88.54%

Table C.2: Table C.1 continued

Database of Figure 5.6												
I	ρ	l	asp.	N	ϕ	vp	vs	ρ_g	R	V_{EX}	V_N	TR
$v_{SV}(90^\circ)$ (wavelet No. 5 of Table 5.2)												
n	0.200	7	0.14	15280	0.1407	5100	2944	2700	0	2377.70	0.808	96.87%
n	0.200	7	0.14	15280	0.1407	5100	2944	2700	1	2363.64	0.803	95.86%
n	0.200	7	0.14	15280	0.1407	5100	2944	2700	2	2362.54	0.802	95.89%
n	0.200	7	0.14	15280	0.1407	5100	2944	2700	3	2367.49	0.804	95.69%
n	0.200	14	0.077	3881	0.0708	5100	2944	2700	0	2461.39	0.836	98.18%
n	0.200	14	0.077	3881	0.0712	5100	2944	2700	1	2430.04	0.825	94.83%
n	0.200	14	0.077	3881	0.0708	5100	2944	2700	2	2434.72	0.827	97.80%
n	0.200	14	0.077	3881	0.0706	5100	2944	2700	3	2433.25	0.827	97.76%
n	0.200	14	0.077	3881	0.0707	5100	2944	2700	4	2435.31	0.827	97.60%
n	0.200	14	0.077	3881	0.0708	5100	2944	2700	5	2448.00	0.831	97.77%
n	0.200	14	0.077	3881	0.0707	5100	2944	2700	6	2441.78	0.829	97.86%
n	0.200	28	0.04	996	0.0358	5100	2944	2700	0	2485.25	0.844	98.22%
n	0.200	56	0.021	252	0.0181	5100	2944	2700	0	2491.75	0.846	96.20%
n	0.200	56	0.021	252	0.0180	5100	2944	2700	1	2483.71	0.844	96.04%
n	0.200	56	0.021	252	0.0180	5100	2944	2700	2	2453.92	0.833	96.76%
n	0.200	56	0.021	252	0.0179	5100	2944	2700	4	2435.44	0.827	94.22%
n	0.200	56	0.021	252	0.0182	5100	2944	2700	5	2491.42	0.846	95.94%
n	0.200	56	0.021	252	0.0182	5100	2944	2700	6	2459.03	0.835	95.53%
n	0.200	56	0.021	252	0.0179	5100	2944	2700	7	2469.33	0.839	96.18%
n	0.200	56	0.021	252	0.0180	5100	2944	2700	8	2492.35	0.847	96.00%
n	0.200	56	0.021	252	0.0180	5100	2944	2700	9	2458.43	0.835	94.62%
n	0.200	56	0.021	252	0.0182	5100	2944	2700	10	2479.10	0.842	96.03%
$v_{SV}(90^\circ)$ (wavelet No. 1 of Table 5.2)												
n	0.200	56	0.021	252	0.0181	5100	2944	2700	0	2484.02	0.844	5.11%
$v_{SV}(90^\circ)$ (wavelet No. 2 of Table 5.2)												
n	0.200	56	0.021	252	0.0181	5100	2944	2700	0	2468.08	0.838	13.08%
$v_{SV}(90^\circ)$ (wavelet No. 3 of Table 5.2)												
n	0.200	56	0.021	252	0.0181	5100	2944	2700	0	2463.82	0.837	25.34%
n	0.200	56	0.021	252	0.0180	5100	2944	2700	1	2452.12	0.833	24.28%
n	0.200	56	0.021	252	0.0180	5100	2944	2700	2	2417.24	0.821	24.84%
n	0.200	56	0.021	252	0.0181	5100	2944	2700	3	2421.91	0.823	24.22%
n	0.200	56	0.021	252	0.0179	5100	2944	2700	4	2422.79	0.823	22.02%
n	0.200	56	0.021	252	0.0182	5100	2944	2700	5	2457.23	0.835	24.32%
$v_{SV}(90^\circ)$ (wavelet No. 4 of Table 5.2)												
n	0.200	56	0.021	252	0.0181	5100	2944	2700	0	2472.35	0.840	75.66%
$v_{SV}(90^\circ)$ (wavelet No. 6 of Table 5.2)												
n	0.200	56	0.021	252	0.0181	5100	2944	2700	0	2472.5	0.840	99.45%

Table C.3: This Table contains information of the different numerical experiments shown in Figure 5.6 .

Database of Figure 5.7 and Figure 5.8													
$v_{SV}(90^\circ)$ wavelet No. 5													
I	ρ	l	as.	N	ϕ	vp	vs	den	R	exv	eff	Atten	
y	0.050	56	0.021	63	0.0045	5100	2944	2700	0	2813.94	0.956	99.02%	
y	0.100	56	0.021	126	0.0091	5100	2944	2700	0	2679.36	0.910	98.17%	
y	0.200	56	0.021	252	0.0181	5100	2944	2700	0	2443.35	0.830	94.46%	
y	0.200	56	0.021	252	0.0182	5100	2944	2700	1	2423.81	0.823	91.68%	
y	0.200	56	0.021	252	0.0181	5100	2944	2700	2	2435.62	0.827	88.44%	
y	0.200	56	0.021	252	0.0182	5100	2944	2700	3	2437.40	0.828	94.35%	
y	0.200	56	0.021	252	0.0181	5100	2944	2700	4	2422.05	0.823	88.70%	
y	0.200	56	0.021	252	0.0182	5100	2944	2700	5	2421.75	0.822	91.83%	
y	0.300	56	0.021	378	0.0270	5100	2944	2700	0	2222.85	0.775	87.65%	
y	0.401	56	0.021	504	0.0360	5100	2944	2700	0	2006.73	0.682	79.56%	
y	0.401	56	0.021	504	0.0361	5100	2944	2700	1	1971.31	0.700	81.68%	
y	0.401	56	0.021	504	0.0361	5100	2944	2700	2	1916.08	0.651	73.44%	
y	0.401	56	0.021	504	0.0360	5100	2944	2700	3	2019.26	0.686	84.36%	
y	0.401	56	0.021	504	0.0359	5100	2944	2700	4	1971.12	0.670	73.70%	
y	0.401	56	0.021	504	0.0360	5100	2944	2700	5	2000.04	0.679	81.83%	
y	0.601	56	0.021	756	0.0539	5100	2944	2700	0	1560.86	0.530	52.82%	
y	0.801	56	0.021	1007	0.0720	5100	2944	2700	0	1181.93	0.401	32.96%	
$v_{SH}(90^\circ)$ wavelet No. 5													
y	0.050	56	0.021	63	0.0045	5100	2944	2700	0	2717.95	0.923	96.33%	
y	0.100	56	0.021	126	0.0091	5100	2944	2700	0	2525.42	0.858	93.46%	
y	0.200	56	0.021	252	0.0181	5100	2944	2700	0	2139.39	0.727	76.18%	
y	0.200	56	0.021	252	0.0182	5100	2944	2700	1	2120.11	0.720	81.96%	
y	0.200	56	0.021	252	0.0181	5100	2944	2700	2	2124.16	0.722	83.03%	
y	0.200	56	0.021	252	0.0182	5100	2944	2700	3	2146.96	0.729	83.40%	
y	0.200	56	0.021	252	0.0181	5100	2944	2700	4	2152.51	0.731	83.69%	
y	0.200	56	0.021	252	0.0182	5100	2944	2700	5	2145.12	0.729	84.35%	
y	0.401	56	0.021	504	0.0360	5100	2944	2700	0	1487.27	0.505	35.64%	
y	0.401	56	0.021	504	0.0361	5100	2944	2700	1	1449.92	0.492	48.99%	
y	0.401	56	0.021	504	0.0361	5100	2944	2700	2	1394.97	0.474	39.21%	
y	0.401	56	0.021	504	0.0360	5100	2944	2700	3	1449.71	0.492	45.89%	
y	0.401	56	0.021	504	0.0359	5100	2944	2700	4	1496.16	0.508	41.26%	
y	0.401	56	0.021	504	0.0360	5100	2944	2700	5	1426.94	0.484	45.53%	
y	0.601	56	0.021	756	0.0539	5100	2944	2700	0	990.27	0.336	9.30%	

Table C.4: This Table contains information of the different numerical experiments shown in Figure 5.7 and Figure 5.8 .

Database of Figure 5.7 and Figure 5.8													
I	ρ	1	as.	N	ϕ	vp	vs	den	R	exv	eff	Atten	
$v_P(90^\circ)$ wavelet No. 5													
y	0.050	56	0.021	63	0.0045	5100	2944	2700	0	4551.07	0.892	96.83%	
y	0.100	56	0.021	126	0.0091	5100	2944	2700	0	4097.04	0.803	94.74%	
y	0.200	56	0.021	252	0.0181	5100	2944	2700	0	3501.67	0.687	83.09%	
y	0.200	56	0.021	252	0.0182	5100	2944	2700	1	3353.13	0.657	80.86%	
y	0.200	56	0.021	252	0.0181	5100	2944	2700	2	3379.61	0.663	84.10%	
y	0.200	56	0.021	252	0.0182	5100	2944	2700	3	3397.31	0.666	85.54%	
y	0.200	56	0.021	252	0.0181	5100	2944	2700	4	3290.60	0.645	79.58%	
y	0.200	56	0.021	252	0.0182	5100	2944	2700	5	3364.91	0.660	85.18%	
y	0.401	56	0.021	504	0.0360	5100	2944	2700	0	2387.33	0.468	54.24%	
y	0.401	56	0.021	504	0.0361	5100	2944	2700	1	2157.97	0.423	52.44%	
y	0.401	56	0.021	504	0.0361	5100	2944	2700	2	2067.43	0.405	39.85%	
y	0.401	56	0.021	504	0.0360	5100	2944	2700	3	2289.79	0.449	53.01%	
y	0.401	56	0.021	504	0.0359	5100	2944	2700	4	2115.57	0.415	44.17%	
y	0.401	56	0.021	504	0.0360	5100	2944	2700	5	2300.93	0.451	54.30%	
y	0.601	56	0.021	756	0.0539	5100	2944	2700	0	1552.61	0.304	17.25%	

Table C.5: Table C.4 continued

Database of Figure 5.9												
I	ρ	l	asp.	N	ϕ	vp	vs	ρ_g	R	V_{EX}	V_N	TR
$v_{SV}(90^\circ)$ (wavelet No. 5 of Table 5.2)												
p	0.025	56	0.021	32	0.0018	5100	2944	2700	0	2817.11	0.957	99.25%
p	0.050	56	0.021	64	0.0036	5100	2944	2700	0	2702.53	0.918	98.28%
p	0.100	56	0.021	128	0.0073	5100	2944	2700	0	2510.20	0.853	96.93%
p	0.200	56	0.021	255	0.0145	5100	2944	2700	0	2199.14	0.747	93.97%
$v_{SH}(90^\circ)$ (wavelet No. 5 of Table 5.2)												
p	0.025	56	0.021	32	0.0018	5100	2944	2700	0	2843.14	0.966	99.54%
p	0.050	56	0.021	64	0.0036	5100	2944	2700	0	2744.43	0.932	98.60%
p	0.100	56	0.021	128	0.0073	5100	2944	2700	0	2571.53	0.873	96.88%
p	0.200	56	0.021	255	0.0145	5100	2944	2700	0	2272.09	0.772	93.36%
$v_P(90^\circ)$ (wavelet No. 5 of Table 5.2)												
p	0.025	56	0.021	32	0.0018	5100	2944	2700	0	4622.60	0.906	98.41%
p	0.050	56	0.021	64	0.0036	5100	2944	2700	0	4201.18	0.824	95.68%
p	0.100	56	0.021	128	0.0073	5100	2944	2700	0	3610.39	0.708	91.06%
p	0.200	56	0.021	255	0.0145	5100	2944	2700	0	2773.32	0.544	78.61%

Table C.6: This Table contains information of the different numerical experiments shown in Figure 5.9 .

Additional experiments												
I	ρ	l	as.	N	ϕ	vp	vs	den	R	exv	eff	Atten
$v_{SV}(90^\circ)$ wavelet No. 5												
n	0.200	56	0.021	252	0.0181	5100	2944	2700	0	2491.75	0.846	96.20%
n	0.200	56	0.021	252	0.0181	5100	4000	1150	0	3392.13	0.848	97.89%
n	0.200	56	0.021	252	0.0181	5100	4000	1150	1	3395.01	0.849	97.36%
n	0.200	56	0.021	252	0.0181	5100	4000	1150	2	3370.41	0.843	98.24%

Table C.7: This Table contains information of some additional numerical experiments.

List of Figures

1.1	Elementary cells with locations where strains, displacement and elastic parameters are defined. (a) Locations are shown on a standard staggered grid if no averaging of medium parameters is performed. (b) Elementary cell of the rotated staggered grid. Spatial derivatives are performed along the \hat{x} - and \hat{z} -axes.	2
2.1	This figure illustrates three types (SH(90), SV(90) and P(90)) of waves in transversely isotropic media. This type of media is used in chapter “Effective velocities in fractured media”	12
2.2	This figure graphically indicates the definitions of phase (wavefront) angle θ and group (ray) angle ϕ	13
3.1	Elementary cells of different staggered grids. Locations where strains, displacement (velocity) and elastic parameters are defined. (a) The elementary cell defined by Virieux [1986]. Note that the velocity components are not defined at the same location. (b) Locations on a standard staggered grid (e.g. [Kneib and Kerner, 1993]) if no averaging of medium parameters is performed. (c) Locations of parameters in the elementary cell for a modified staggered grid under the conditions mentioned in the text. (d) Elementary cell of the new rotated staggered grid. Spatial derivatives are performed along the \tilde{x} - and \tilde{z} -axes. The wave equation and the elements of the stiffness tensor are the same as in (b)	18
3.2	This figure illustrates the shift of the position of the derivative from the standard staggered grid technique to the rotated staggered grid technique (2D case). The technique makes use of the well known formula $\frac{\delta f}{\delta \mathbf{m}}(P_0) = \mathbf{grad} f(P_0) \cdot \mathbf{m}$ to calculate the derivatives in the old directions (axes).	22

- 3.3 Curves showing modeling errors caused by numerical dispersion for the new rotated staggered grid (left side) and the standard staggered grid (right side) for the 2D case ($\vartheta = \pi/2$). In the top row the angle between the direction of wave propagation and the axes is 45 degrees ($\varphi = \pi/4$). For the bottom row the angle is 0 degree ($\varphi = 0$). In each plot γ varies from γ_{max} (top) to 40% of γ_{max} (bottom) in steps of 20%. All curves are calculated for 8th order spatial differentiations using Central Limit coefficients [Karrenbach, 1995] (similar to Holberg coefficients [Holberg, 1987; Kindelan et al., 1990]) and 2nd order time update. Note that γ_{max} has different values for the different grids (see Section 3.5.3). 30
- 3.4 Curves showing modeling errors caused by numerical dispersion for the new rotated staggered grid (left side) and the standard staggered grid (right side) for the 2D case ($\vartheta = \pi/2$). The angle between the direction of wave propagation and the axes is 45 degrees ($\varphi = \pi/4$) on the left and 0 degree ($\varphi = 0$) on the right side. In each plot the order of spatial differentiations varies from 8 (top) to 2 (bottom) in steps of 2. All curves are calculated with Central Limit coefficients [Karrenbach, 1995; Kindelan et al., 1990] and 2nd order time update. γ is set to 40 % of γ_{max} 31
- 3.5 The spatial variation of the relative error of the phase velocity for the new rotated staggered grid (solid lines), and the standard staggered grid (dotted lines) is depicted. The computation is done for 2nd order spatial differentiations and 2nd order time update (2D case). The distance between the curve and the origin has the value $|A_{rel} - 1|$ (see Section 3.5.3) of the corresponding direction. In each Figure γ' and H' belong to the new rotated grid and γ and H to the standard staggered grid. Figure on the left side: $\gamma' = \gamma (= 80\% \cdot \gamma_{max})$, $H' = H (= 0.1)$. Figure on the right side: $\gamma' = \sqrt{2} \cdot \gamma (= 80\% \cdot \gamma'_{max})$, $H' = 1/\sqrt{2} \cdot H (= 1/\sqrt{2} \cdot 0.1)$ 32
- 3.6 The spatial variation of the relative error of the phase velocity (compare with Figure 3.5) for the new rotated grid (left side), and the standard staggered grid (right side) is depicted. The computation is done for 2nd order spatial differentiations and 2nd order time update (3D case). Figure on the left side (new rotated staggered grid): $\gamma' = 80\% \gamma'_{max}$, $H' = 0.1$. Figure on the right side (standard staggered grid): $\gamma = 80\% \gamma_{max} = 1/\sqrt{3} \cdot \gamma'$, $H = H' \cdot \sqrt{3}$. Note that the maximum phase velocity error of the new rotated staggered grid shown in this figure is 2.82%. This is less than the maximum error of the standard staggered grid (3.93%). 34
- 4.1 Modeling result (right side) for the 2D model shown on the left side. The new rotated staggered grid was used and a stable result was obtained. Compressional and shear waves and the influence of the crack and the boundaries can be seen very well. For details of the modeling see Section 4.1. 38

4.2 A typical geophysical situation with topography.	40
4.3 X-component-Snapshot at $1.09375\mu s$	41
4.4 Z-component-Snapshot at $2.1875\mu s$	41
4.5 A slice of the 3D aluminum plate model and three snapshots of the component of the displacement vector perpendicular to the plate at the surface of the aluminum plate at $50\mu s$, $100\mu s$ and $150\mu s$ after applying the source pulse at the point "S". Black (white) colors denote high positive (negative) amplitudes. Note that on the left-hand Figure the white area around the aluminum plate corresponds to the vacuum part of the model. The thin black line denotes the boundary of the model. The curves in Figure 4.6 were recorded at the point "R".	43
4.6 Comparison of experimental data to the result of the simulation: Signal recorded by an ultrasonic (point) receiver located at the point "R" in Figure 4.5.	43
4.7 The deformation of a thin plate during propagation of antisymmetrical Lamb waves (a) and symmetrical Lamb waves (b) is shown. The arrows mark the direction of wave propagation.	44
4.8 The strong physical dispersion of the generated antisymmetric Lamb waves is depicted (solid line). For comparison the amplitude spectrum of the wavelet (source-time function) is plotted (dashed line) in the same diagram.	45
4.9 Principle of the experiment	45
4.10 A slice of the 3D aluminum plate model is shown. It is easy to detect the crack in the homogeneous plate.	47
4.11 Snapshots of the wave field at $10.5\mu s$	47
4.12 Snapshots of the wave field at $21\mu s$	48
4.13 Snapshots of the wave field at $31.5\mu s$	48
4.14 Snapshots of the wave field at $52.5\mu s$	49
4.15 Snapshots of the wave field at $105\mu s$	49
4.16 Modeling of wave propagation in transversely isotropic medium. The details are in section 4.5	51
4.17 On the left side a heterogeneous concrete model with a defect, i.e. the crack, is shown. The ellipses represent gravel within cement. The concrete model is bounded by a thin layer of air. The right figure shows a Z-snapshot after a part of a plane wave has been reflected by the crack.	53

4.18 The migration of the plane-wave response is on the left. On the right is the envelope of the migrated section	53
5.1 Randomly distributed and randomly oriented rectilinear non-intersecting thin dry cracks in homogeneous 2D-media. A part of Model 7.1 is shown (see Table 5.1).	58
5.2 Randomly distributed and randomly oriented rectilinear intersecting thin dry cracks in homogeneous 2D-media. A part of Model 10x.1 is shown (see Table 5.1).	61
5.3 Randomly distributed rectilinear parallel non-intersecting thin dry cracks in homogeneous 2D-media. A part of Model 18p is shown (see Table 5.1).	65
5.4 The left hand side shows a typical fractured model (No. 7.1 of Table 5.1) used for the numerical experiments. I introduce a cracked region in a homogeneous material. At the top I place a small strip of vacuum. This is advantageous for applying a body force line source with the rotated staggered grid. The right side is a snapshot of a plane wave propagating through the cracked region.	67
5.5 Normalized effective velocity versus crack density. Dots: Numerical results of this study, Lines: Different theoretical predictions. The error bar denotes the standard deviation for different model realizations (see Table 5.1).	70
5.6 Normalized effective velocity (SH- waves) versus $p = 2l / \lambda_{\text{dom}}$ (normalized frequency), for crack density $\rho = 0.2$. Dots: Numerical results of this study, Two horizontal lines at the top: Different theoretical predictions. The error bar denotes the standard deviation for different model realizations (see Table 5.1). Note, the numerical result depicted at $p=0.095$ is depicted in Figure 5.5, too.	71
5.7 Normalized effective SH-wave velocities for intersecting cracks versus porosity. Dots: Numerical results, Line: Theoretical predictions of the modified DEM-theory.	73
5.8 Normalized effective SH-, SV- and P-wave velocities for intersecting cracks versus crack density. Dots: Numerical results of this study, Lines: Theoretical predictions of the CCD-formulations. The error bar denotes the standard deviation for different model realizations (see Table 5.1).	74
5.9 Normalized effective SH-, SV- and P-wave velocities for parallel cracks versus crack density. Dots: Numerical results, Dashed lines: Theoretical predictions of the theory for non-interacting parallel cracks.	75

Acknowledgments / Danksagung

An der Entstehung einer Dissertation sind viele Personen direkt und indirekt beteiligt. Ohne die großartige und facettenreiche Unterstützung der folgenden (und weiteren) Personen wäre diese Arbeit in der vorliegenden Version nicht möglich gewesen:

Prof. P. Hubral, Prof. Sergei A. Shapiro, Andreas Kirchner, Tobias Müller, Kai-Uwe Vieth, Jörg Zaske, Heiko Priller, Prof. E. A. Robinson, Prof. L. W. B. Leite, Norbert Gold, Jürgen Mann, Thilo Müller, Martin Karrenbach, Petra Knopf, Peter Dausch, Claudia Payne, meine gesamte Familie, insbesondere Ulla, Kilian, Julius und meine Eltern.

Vielen Dank !

Curriculum vitae

Persönliche Daten

Name	Erik Hans Saenger
Anschrift	Yorckstr.11 76185 Karlsruhe Tel. (0721) 8303544 email: erik@saenger.org
Geburtsdatum	23.6.1970
Geburtsort	Konstanz
Familienstand	verheiratet, 2 Kinder

Schulausbildung

1976-1977	Grundschule Konstanz
1977-1980	Grundschule Waldbronn
1980-1989	Gymnasium Karlsbad Abschluß: allgemeine Hochschulreife

Zivildienst

1989-1990	Pflegehelfer auf einer Station für Schädel-Hirn-Verletzte im Rehabilitationskrankenhaus Karlsbad-Langensteinbach
-----------	---

Hochschulausbildung

10/1990	Beginn des Studiums der Physik (Diplom) an der Universität Karlsruhe (TH)
23.09.1992	Vordiplom
04/1993	Fortsetzung des Studiums an der FU Berlin
10/1995	Fortsetzung des Studiums an der Universität Karlsruhe (TH)
11/1995 - 05/1997	Diplomarbeit im Forschungszentrum Karlsruhe
9.03.1998	Abschluß: Diplom-Physiker

Berufspraxis

seit 1.04.1998	Wiss. Angestellter am Geophysikalischen Institut der Universität Karlsruhe (TH)
----------------	--

